Renewable Energy 205 (2023) 956–991

Contents lists available at ScienceDirect

Renewable Energy

journal homepage: www.elsevier.com/locate/renene

Progress and opportunities in corrosion mitigation in heat transfer fluids for next-generation concentrating solar power

P. Kondaiah **, R. Pitchumani *

Advanced Materials and Technologies Laboratory, Department of Mechanical Engineering, Virginia Tech, Blacksburg, VA, 24061, USA

ARTICLE INFO

Keywords:
Corrosion
Molten salts
Liquid metals
Supercritical CO_2
Oxide coatings
Texturing

ABSTRACT

Concentrating solar power (CSP) systems have gained considerable eminence in converting solar thermal energy into electrical power in recent years. According to the U.S. Department of Energy's Gen3 roadmap, the CSP system should operate > 700 °C, as its efficiency depends directly on the operating temperature of the heat transfer fluids (HTFs). A significant challenge, however, is the corrosion of containment materials by the HTFs that is exacerbated at the higher temperatures. A comprehensive review of the high temperature stable HTFs, their properties, corrosion mechanisms on different alloys, and corrosion mitigation measures is of much importance for directing a concerted research and development in the field, which forms the motivation for this compendium. First, molten salt HTFs and their thermophysical properties, along with liquid metals, are introduced. Corrosion of structural materials in different HTFs including molten salts, liquid metals, and supercritical carbon-di-oxide at various temperatures and the corrosion mechanisms are comprehensively reviewed. In addition, several corrosion mitigation methods are discussed. Finally, future directions for HTFs and corrosion mitigation methods in molten salts are proposed. The holistic review presented here will serve as the foundation for further research addressing relevant challenges and enabling the promise of achieving cost-competitive CSP.

1. Introduction

In the last decade, global energy demand has increased enormously in various forms, mainly due to industrialization and broader economic development. Use of fossil fuels is directly correlated to increasing anthropogenic greenhouse gas production that exacerbates global warming. Renewable energy sources, on the other hand, are clean, plentiful, accessible globally, and inexhaustible. As per the BP Statistical Review of World Energy 2017, low-carbon emission strategies continued worldwide, and the electricity generation capacity of renewable energy increased by 20% [1]. Besides, new environmental policies promote the role of renewable energy and its usage for an energy-secure future of our planet. The earth receives abundant solar radiation in two forms, i.e., direct normal irradiation and diffuse scattered radiation. Direct normal irradiation is the primary energy resource for concentrating solar power (CSP) technology, and it can be used to convert solar thermal energy into electricity. Globally available direct normal radiation is shown in Fig. 1.

Solar thermal energy utilization occurs in three ways, low-temperature (< 80 °C), mid-temperature (80–250 °C), and high-temperature (> 250 °C) thermal utilization. Low-temperature applications using solar heating systems are relatively mature [2]. Using CSP technology, medium- and high-temperature thermal energy can generate electrical power [3]. CSP plants require 2000–2800 kWh/m^2/yr or more of direct normal radiation [4] and can be useful for commercial applications based on their higher thermal storage efficiency than solar PV and wind energy [5]. CSP plants are expected to contribute to 7% of global electricity contribution by 2030 and 25% by 2050 [6].

Generally, CSP technology can be used in four ways depending on how the various systems collect solar energy: parabolic trough collector (PTC), linear Fresnel reflector (LFR), solar parabolic dish (SPD), and solar power tower (SPT) plants. The first PTC-based CSP with 354 MW of installed capacity was constructed in California in 1980. In 1982, the U.S Department of Energy demonstrated the first SPT technology, called Solar One, with a 10 MW installed capacity. In 1996, Solar Two demonstrated an energy storage system to improve efficiency and produce electricity, even on days with no direct sunlight. Integrating CSP with an energy storage system provides for dispatchable high-value energy, reliable system capacity and operating reserves. The SPT system with a conventional steam-Rankine power cycle integrated with two tanks and running at 550 °C has reduced the levelized cost of electricity

* Corresponding author.
** Corresponding author.
E-mail addresses: paruchuri@vt.edu (P. Kondaiah), pitchu@vt.edu (R. Pitchumani).

https://doi.org/10.1016/j.renene.2023.01.044
Received 22 April 2022; Received in revised form 23 September 2022; Accepted 11 January 2023
Available online 14 January 2023

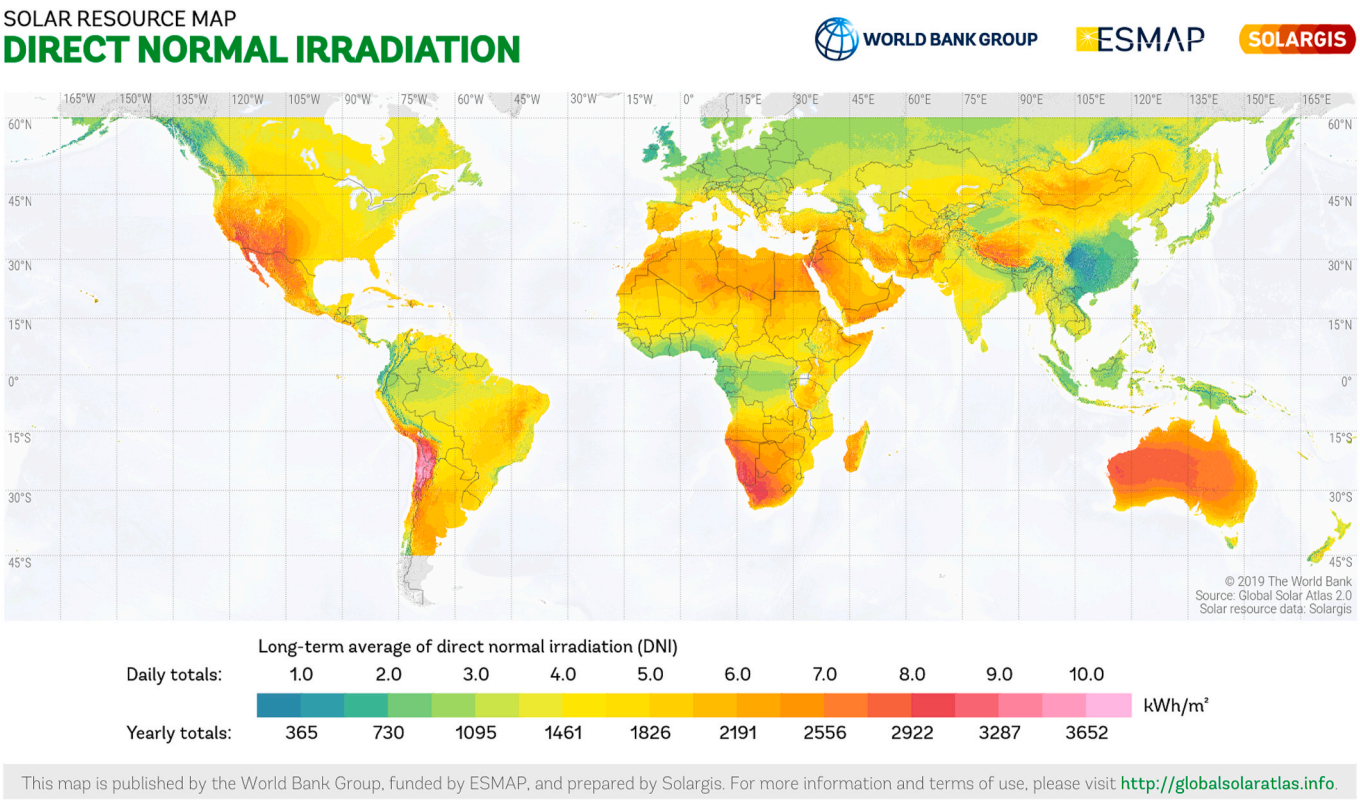

Fig. 1. Global available direct normal irradiation (downloaded from http://globalsolaratlas.info; Accessed February 2022).

from CSP by about 50% compared to the previous generation PTC-based systems [7].

CSP installed grew rapidly in the period 2010 to 2013, and their capacity increased 215% by the end of 2013 (2009: 700 MW to 2013: 2205 MW), fueled by the tremendous growth of CSP installations in China, Chile, India, Morocco, South Africa, and United Arab Emirates. Among them, China has begun constructing fifteen CSP plants with a total capacity of 1064 MW. Achkari and El Fadar [8] reported that 45% of the SPT plants are presently in development, with 60% installed capacity and 42% of PTC plants with 37% of the installed capacity. The worldwide installed, and near-developing capacity of the PTC and SPT plants are shown in Fig. 2.

A typical SPT CSP plant mainly consists of four parts (1) heliostats, (2) a heat transfer subsystem, (3) a thermal energy storage subsystem, and (4) a backup system. A typical CSP plant operates as follows: the concentrated sunlight from mirrors focuses on an absorber with flowing heat transfer fluid (HTF); the heated HTF is then flowed to a power block for electricity generation. The heated HTF can also be transferred to an ancillary storage system maintained at an elevated temperature to control the electricity generation in the backup system. The efficiency of the CSP plant depends on the HTF and its operating temperature. The schematic diagram of the commercial SPT is shown in Fig. 3.

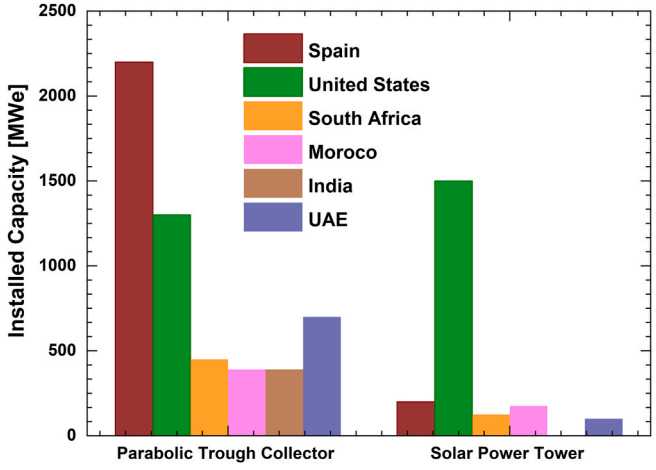

Fig. 2. Worldwide installed capacity of PTC and SPT plants (installed and under development).

The International Renewable Energy Agency (IRENA) reports that the levelized cost of electricity (LOCE) of CSP plants is a direct function of the amount of energy storage [9]. The LCOE of SPT plants is more attractive than PTC plants with the incorporation of thermal energy storage (TES) systems. The high operating temperature in a SPT increases the temperature difference in the TES system and reduces the required amount of TES materials [9]. The report further states that the installed CSP capacity globally grew to about 5.5 GW by 2018 representing 4.3-fold of what it was in 2010. Correspondingly, the global weighted average LCOE of the marginal 0.5 GW of added capacity in 2018 was US $0.185/kWh, 26% lower than the LCOE in 2017 and 46% lower than the LCOE in 2010 [10]. According to the U.S. Department of Energy's National Renewable Energy Laboratory (NREL), CSP technology generations are based on the type of collector and HTF used in the plant. CSP technology is classified as three generations in which Gen1 and Gen2 use the same nitrate salt for thermal storage, but differ in the type of collector. On the other hand, Gen3 runs with different HTF (chloride, carbonate, and supercritical CO_2) [11]. TES plays an important role in the total plant cost as it determines the size of the tanks and heat transfer fluids.

Another essential and cost-determining factor in CSP plants is the corrosion of containment materials in contact with the heat transfer fluids. In this context, the cost of molten salts and corrosion rate has been considered without impact on the plant efficiency. Besides, the possible failure of all the metallic alloys of containment materials used in receivers, storage tanks, piping, valves, and pumps should be

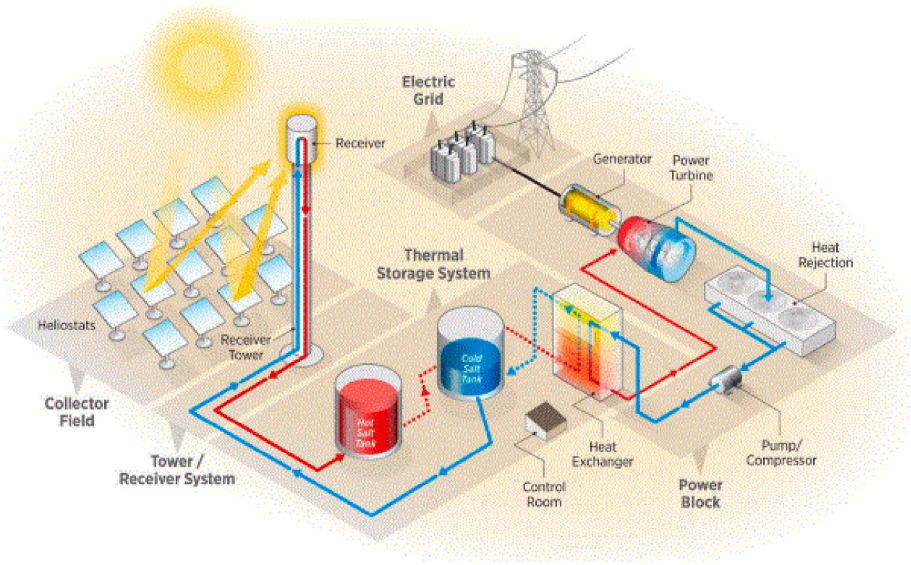

Fig. 3. Schematic of a STP plant incorporating two-tank molten salt storage (reproduced with permission from Ref. [7]).

considered in the long run operation at high temperatures [12]. In 2016, the U.S. Department of Energy's SunShot Initiative program advised three potential pathways for next generation (Gen3) CSP plant based on the thermal carrier in the receiver (molten salt, gaseous fluid, and particle). The goals and challenges of Gen3 CSP are shown in Fig. 4, which demonstrate various pathways to improve the efficiency of the CSP system [7].

According to Gen3 CSP roadmap, there are many research opportunities and challenges in all fields like heat transfer fluids, materials design, energy storage systems, heat exchangers, and turbine engines to improve the overall efficiency, of which lowering the technology costs is paramount. It involves considering new materials from the perspective of initial cost and the entire long-term system integrity. Of particular importance are the performance and stability of the materials in contact with heat transfer fluids at high temperature and limiting the associated mechanical stress during the operation of a CSP plant.

In recent years, extensive research has been conducted and published. Previous review articles on corrosion considered specific research topics independently. This review aims to provide a more holistic overview of corrosion of containment materials focusing on different HTFs at high temperatures, the importance of salts purification methods, and innovative corrosion mitigation methods for next-generation CSP. Based on the latest literature, it also uncovers the present technology gaps and areas for future studies toward development of

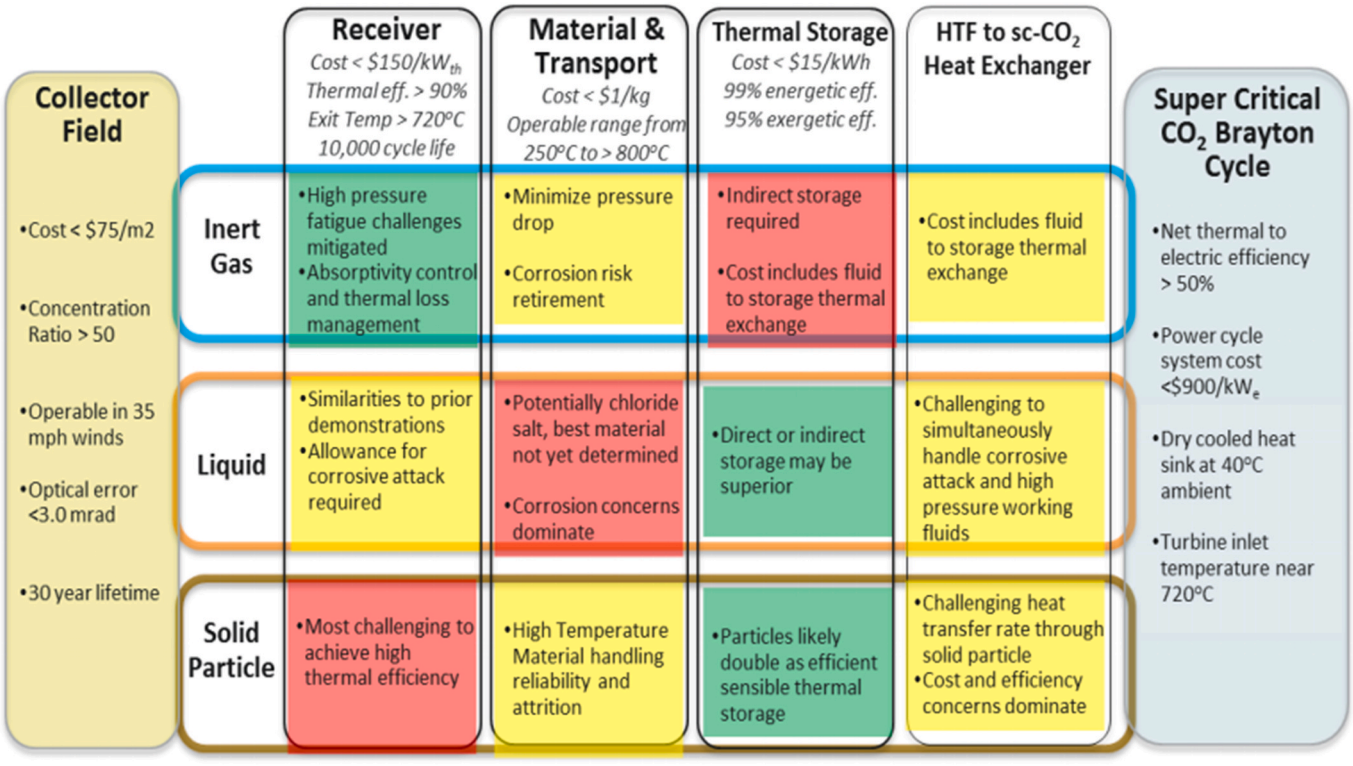

Fig. 4. Various pathways and challenges for Gen3 CSP technology (reproduced with permission from Ref. [7]).

Gen3 CSP technology. The main challenges and research gaps identified in CSP technology, especially with regard to molten salts, and their properties, material selection, corrosion in molten salts, and corrosion mitigation techniques, are explained section-wise to meet the U.S. Department of Energy Solar Energy Technologies' 2030 goals.

The review article is organized as follows: the importance of concentrating solar thermal technologies against conventional power plants in reducing global warming and the overall Gen3 CSP goals were described in this section. Heat transfer fluids used in CSP plants and different types of molten salts properties are described in section 2, which is followed by a discussion of corrosion of various structural materials in molten nitrate, chloride, carbonate, fluoride eutectic salts, and liquid metals as well as their respective corrosion mechanisms in section 3. Finally, the possible corrosion mitigation methods such as molten salt chemistry modifications, structural materials modifications, and coatings options are explained in section 4.

2. Heat transfer fluids

Generally, high-temperature TES systems are of three types: sensible heat storage, latent heat storage, and thermochemical storage systems. Sensible heat storage systems store and release thermal energy by raising and lowering the temperature of the material. Latent heat storage systems work on the principle of endothermic and exothermic processes taking place in phase change medium. Thermochemical storage accomplishes its energy storage through reversible chemical reactions of the medium. So far, only sensible heat storage systems have been used in commercial CSP plants [13,14]. Solar salt, Hitec, or HitecXL salts have been used in commercial CSP installations as HTF [15,16]. Eurelios station in Italy, CESA-1, Andasol power plant, and Solar Tres in Spain, and Solar Two station in the US have all used solar salt as the heat storage material [17,18]. Gemasolar is the first commercial solar tower plant that can operate at temperature up to 565 °C using molten salt as HTF and storage medium [19].

The operating temperature and thermophysical properties are important indicators for the efficacy of HTFs and storage media, of which the thermophysical properties—heat capacity, thermal conductivity, viscosity, and density—are fundamental in designing the storage system. Heat storage capacity of the HTF is determined by density and heat capacity. The viscosity of the HTF determines the size of heat exchanger as it influences pumping power of the fluid in the pipelines. A high thermal conductivity of the HTFs increases the efficiency of the heat exchange processes [20]. To improve the efficiency and lifetime of the plant, thermophysical properties like thermal conductivity, heat capacity, thermal stability, density, and viscosity of the molten salts need to be improved. Heat capacity and thermal stability can be measured using differential scanning calorimetry (DSC) and thermal gravimetric analysis (TGA), respectively, although thermogravimetric methods are considered as qualitative (semiquantitative) techniques for a comparison of the thermal stability of various HTFs. Direct interrogation of thermal energy storage also can be used to find exact decomposition of HTF [21]. Thermal conductivity is measured using laser flash analysis (LFA) and viscosity of the salts can be measured by capillary tube viscometry.

Several authors have presented an overview of certain molten salts and their limiting operating temperatures. Vignarooban et al. [22] considered the heat transfer fluids of thermal oils, organic fluids, air, water/steam, molten salts, and liquid metals. They particularly focused on the melting temperature and thermal stability of the HTFs and corrosion of various alloys in that media. Many researchers have recently focused on improving the salt properties by varying the composition and adding metal and ceramic nanoparticles into the salts. Henriquez et al. [23] investigated the thermophysical properties of solar salt with the influence of distinct degrees of purity of $LiNO_3$ in a ternary mixture of 30 wt% $LiNO_3$ + 13 wt% $NaNO_3$ + 57 wt% KNO_3. The melting temperature of the mixture for different purities shows a reduction of 92–96 °C compared to solar salt (223 °C), while the heat capacity exhibited between 14% and 21% increase than the solar salt currently used. The thermal stability results showed a maximum temperature of 596 °C, similar to that of solar salt.

Durth et al. [24] studied and optimized the TES cost of solar concentration systems by analyzing solar salt mixture with various percentages of $NaNO_3$ and KNO_3. A salt with a higher sodium nitrate concentration was reported to have a higher heat capacity that positively impacts the plant cost and reduces the size of the storage. However, thermal stability of the salt mixture did not show a significant variation with different sodium nitrate concentrations. Ternary reciprocal systems such as Hitec salt with $LiNO_3$ were studied by Villada et al. [25]. The resulting new mixture with 15% of $LiNO_3$ had a melting temperature of 77.5 °C, which is about 65 °C lower than that of commercial Hitec salt (141.8 °C), and was thermally stable in a nitrogen atmosphere up to 635 °C. They concluded that based on the melting point, heat capacity, thermal stability, and viscosity, the new molten salt mixtures have great potential for applications in thermal storage systems regardless of the cost of the lithium nitrate. The new mixture was selected as an alternative to the current Hitec salt based on its improved thermophysical properties such as heat capacity of 1.86 J/g °C at 300 °C, storage capacity of 237 KWh, and viscosity of 11.7 cp at 160 °C. The thermal stability of the new mixtures of salt is shown in Fig. 5. It is reported that thermal stability of Hitec salt with various percentage of $LiNO_3$ under N_2 atmosphere was higher than 610 °C—15% $LiNO_3$: 635.8 °C, 20% $LiNO_3$: 624 °C, 30% $LiNO_3$: 612 °C [25]. They defined the maximum stability temperature as the point where 3% of overall weight loss occurred, which is crucial as different mass loss definitions will result in other stability limits [26,27].

Zou et al. [28] proposed a quaternary nitrate molten salt composed of Hitec salt with $Ca(NO_3)_2$ additives. The melting temperature, crystallization, and thermal stability points of the salt were found to be 83.1 °C, 163.1 °C, and 628.5 °C, respectively. The operating temperature range of the new salt was observed in the range from 200 °C to 565 °C which was wider than those of Hitec salt (200–450 °C) and solar salt (290–565 °C). The average specific heat and thermal conductivity of the Hitec salt with $Ca(NO_3)_2$ additives are found to be approximately 1.52 J/(g K) and 0.655 W/(m K), respectively. The mixed molten salts exhibited good thermal stability up to 565 °C for 1200 h and 120 times for quenching/heating experiments conducted at atmospheric conditions.

Adding nanoparticles to molten salt is an alternative method pursued by several research efforts to improve its thermal performance, especially in enhancing the thermophysical properties by adding different types of nanoparticles. It is worth noting that SiO_2 nanoparticles are regarded as exceptional candidate material used in molten salts as nanofluids [29,30]. Wei et al. [31] prepared solar salt nano-fluids with 2.5, 3.5, 4.5, 5.0, and 10.0 wt% MgO nanoparticles of size ~60 nm and studied their thermal properties over 220 °C. The results showed that the viscosity and density of nano-fluids were close to those of solar salt, at about 5.1–2.4 cp and 1.96–1.83 g/cm^3 at 240–380 °C. The average specific heat capacity of the fluids with 0–5.0 wt% MgO nanoparticles varied from 1.442 to 1.613 J/(g.K), and the thermal conductivity ranged from 0.37 to 0.60 W/(m.K) at 375 °C. The structure of the quasi-solid layer formed due to attraction of nanoparticles to the surrounding ions and the micro-disturbance caused by the Brownian motion of the nanoparticles in the molten salt may enhance the properties. They concluded that the solar salt nanofluid with 5.0 wt % MgO is a promising heat transfer and thermal storage fluid in a CSP system. Although nanoadditives to molten salts appear to result in beneficial thermophysical properties, especially in terms of the potential increase in heat capacity, their viability for practical use is yet to be established. Among their limitations, the reactions of the molten nitrate salt with the oxide particles usually result in the incorporation of Na and/or K cations in the oxide particles. Also, there is a fundamental lack of understanding of the underlying mechanisms of specific heat enhancement or the long-term

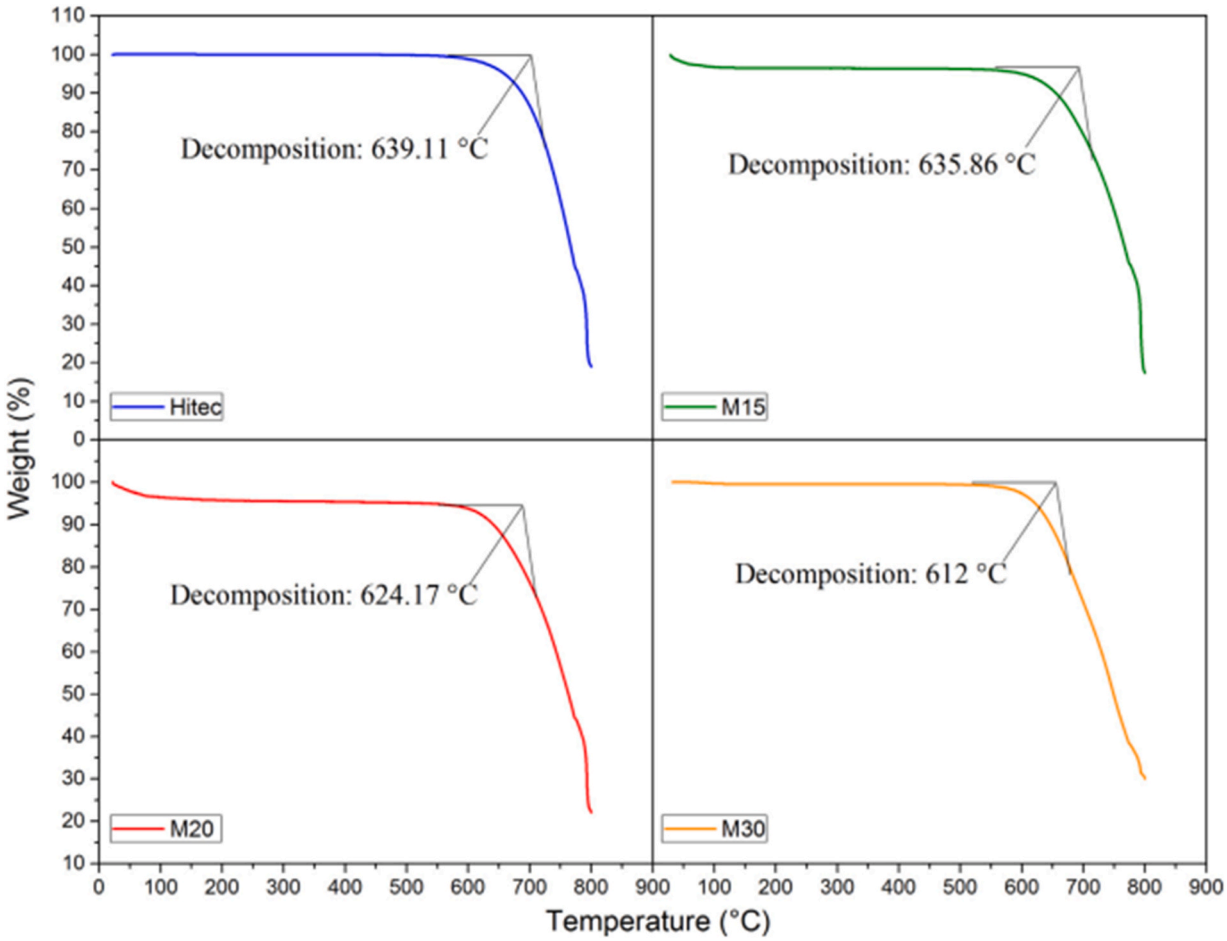

Fig. 5. Decomposition temperature of different molten salt mixtures measured from TGA. Hitec, M15: Hitec +15% $LiNO_3$, M20: Hitec +20% $LiNO_3$, and M30: Hitec +30% $LiNO_3$ (reproduced with permission from Ref. [25]).°

stability of the beneficial effects.

The nitrate mixtures are the most suitable materials for CSP applications at medium temperatures (100–600 °C). However, the current generation molten salts (solar salt and Hitec) decompose around 625 °C, making them inefficient for many advanced high-temperature power cycles. The recent U.S. Department of Energy Gen3 CSP Roadmap [7] is structured around developing an sCO_2 Brayton power cycle operating between temperature limits of 500 °C and 700 °C, where the hot salt temperature would need to be at least at 720 °C, in order to deliver a power cycle working fluid inlet temperature of 700 °C. In actual systems, the HTFs and storage fluids are composed of a mixed molten salt developed of binary and ternary eutectic salts rather than one kind of molten salt. The advantage of using mixed molten salts is that the required melting point can be achieved by partially changing the ratio of its components to accommodate a more wide-ranging temperature range. Compared with a single salt, a mixed salt provides a higher sensible heat storage density when melting at a similar temperature.

Goutham et al. [32] proposed four ternary chloride mixtures of different cation combinations (Na, K, Li, Mg) developed using the software, FactSage. The eutectic point was validated experimentally by differential scanning calorimetry. A phase diagram predicted using FactSage for a ternary mixture of NaCl–KCl–MgCl is shown in Fig. 6, and the formation of a eutectic mixture based on this FactSage prediction was found to be 383 °C. Han et al. [33] prepared chloride salt/-nanoparticle composite phase change materials by adding different concentrations of Al_2O_3, CuO, and ZnO nanoparticles dispersed into the base salt $MgCl_2$:KCl:NaCl with 51:22:27 M ratio and measured the thermal properties. The prepared composite materials' melting temperature was very close to that of the base salt in their results. The latent heat of phase change was slightly lower than that of the base, whereas enhancement was noted in the thermal conductivity and thermal diffusivity after adding the dopant nanoparticles. With Al_2O_3 nanoparticles, the thermal conductivity of the salt showed the most noticeable enhancement of 48%, compared to that of the base salt. So, Al_2O_3 nanoparticles could be considered an optimal additive to expand the thermal conductivity of chloride salts. It is also noticed that the upper limiting temperature for all samples in an argon atmosphere is above 800 °C. In particular, a composite doped with Al_2O_3 showed the best thermal stability temperature of 820 °C.

The vapor pressure of the molten salt used as thermal storage medium is another important consideration in the operation of the CSP plant. A vapor pressure greater than 1.0 atm will be detrimental to containment materials, particularly at the high temperatures. Nevertheless, at the operating temperatures of the sCO_2 Brayton cycle at high efficiencies (T > 720 °C), $AlCl_3$, $FeCl_3$, and $ZnCl_2$ have large vapor pressures (> 1 bar), whereas other chlorides such as $MgCl_2$ have small vapor pressures (< 0.01 bar) [34]. Low vapor pressure is beneficial for use of molten chlorides as TES/HTF. Wang et al. [35] examined a group of ternary eutectic halide salts with the goal of developing a high-temperature HTF that has a freezing point < 250 °C and vapor pressure < 1.0 atm, at temperatures up to 800 °C. Three chloride salts of i) 18.6% NaCl-21.9% KCl-59.5% $ZnCl_2$, T_{mp} = 213 °C; ii) 13.4% NaCl-33.7% KCl-52.9% $ZnCl_2$, T_{mp} = 204 °C; and iii) 13.8% NaCl-41.9% KCl-44.3% $ZnCl_2$, T_{mp} = 229 °C with different molar ratios showed different melting temperatures (T_{mp}) below 250 °C and it was found that the vapor pressure of all the three eutectic molten salts was below 1.0

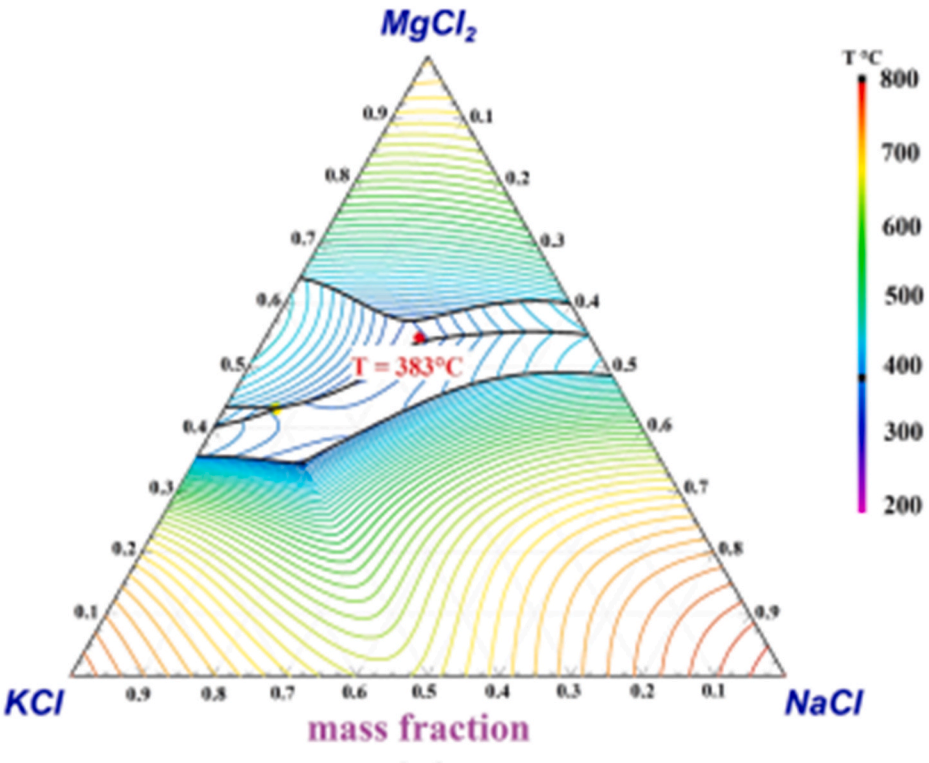

Fig. 6. Phase diagram predicted for 24.5% NaCl +20.5% KCl+55%MgCl eutectic salt using FactSage (reproduced with permission from Ref. [32]).

atm at 800 °C. A $ZnCl_2$–KCl–NaCl salt in mole fraction ratio of 44.3%-41.9%–13.8% exhibited the least vapor pressure of about 1.0 atm at temperature as high as 900 °C. Xu et al. [36] observed that the vapor pressure of eutectic $MgCl_2$–KCl salt increases with temperature but is < 13 kPa even at a high temperature of 800 °C. The low vapor pressure leads to a minimal mass loss of $MgCl_2$–KCl molten salts in an open container.

Numerical calculations have been used to predict the macroscopic and thermal properties of new molten salts. Recently, research focused on different chloride and carbonate molten salt mixtures to predict their thermophysical properties. Li et al. [37] provided a simulation study on thermophysical properties of 16 eutectic binary and ternary chloride molten salts in comparison to their own experimental data as well as those reported in the literature. Average ionic weight correlation, mole fraction average, and rough hard-sphere models were examined to predict the properties of binary and ternary eutectic salts composed of any species of NaCl, KCl, $MgCl_2$, $CaCl_2$, and $ZnCl_2$. The expected results on thermal conductivity for 68% KCl-32% $MgCl_2$ salt are shown in Fig. 7. It is reported that the predicted thermal conductivity of designed eutectic molten salt system using the rough hard sphere (RHS) method has an excellent agreement (with a deviation < 5%) with experimental data. Moreover, in predicting the density of the selected salts, mass fraction average and quasi-chemical model (QCM) are used. The simulation results for salt (13.4% NaCl-33.7% KCl-52.9% $ZnCl_2$) density compared with the experimental data are as shown in Fig. 8. From the Figure, it can be observed that the densities of the eutectic salts predicted using QCM have a better agreement (with a deviation < 5%) with the experimental data than the predictions of the other methods.

In another study, the local structures and thermodynamic properties of LiCl–KCl are computed by using molecular dynamics simulations (MD), and the results are consistent with available experimental literature data [38] obtained at the same temperature [39,40]. The errors in the predicted thermal properties are within 11.1%, which was deemed accurate and reliable. The results showed that Li^+ promotes the diffusion in the system efficiently. In addition, the specific heat capacity and

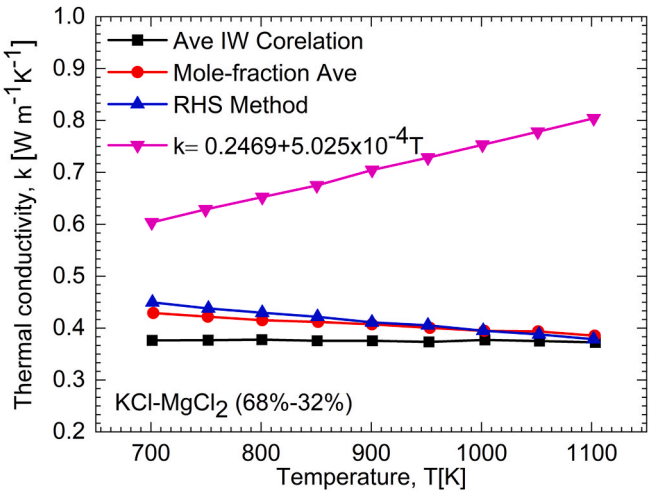

Fig. 7. Thermal conductivity of KCl–$MgCl_2$ salt derived from different prediction methods (reproduced with permission from Ref. [37]).

thermal conductivity significantly improved with Li^+. Specific heat capacities were calculated using a series of NPT molecular dynamics simulations at different temperatures. Temperature dependence of specific heat capacity with various components is presented in Fig. 9, which shows that the specific heat capacity of LiCl–KCl has a minimal change that matches the experimental results and increases with the increase of Li^+. The simulation models used in the prediction of the thermophysical properties of the designed molten salts are given in Table 1.

Liquid metals also can be used in CSP systems as HTF and thermal energy storage media. Although there are no commercial CSP systems using liquid metals, they are attractive for their wide operating temperature range, efficient heat transfer characteristics, and low viscosity. Lorenzin et al. [41] reviewed five liquid metals of molten tin (Sn),

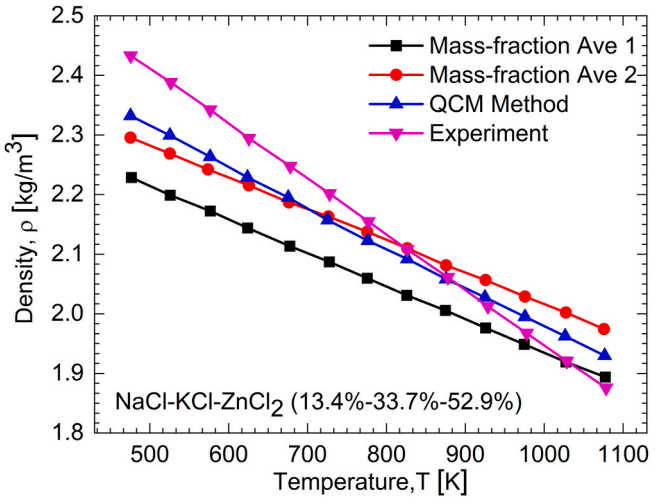

Fig. 8. Density of NaCl–KCl–$ZnCl_2$ obtained from experimental work and different prediction methods (reproduced with permission from Ref. [37]).

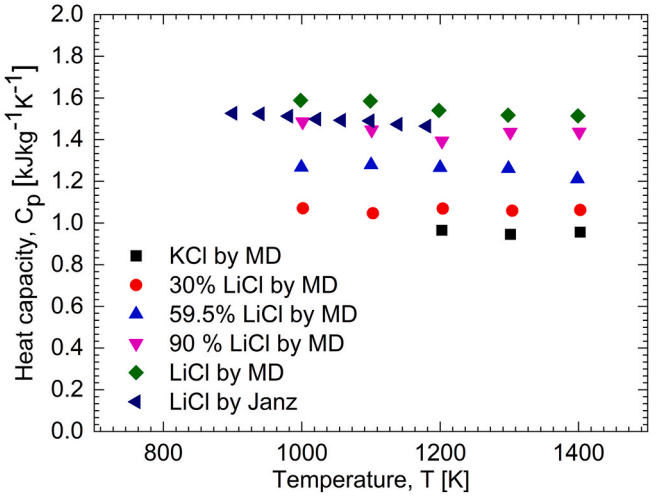

Fig. 9. Specific heat capacity of binary salt (LiCl/KCl) mixture with respect to temperature (reproduced with permission from Ref. [38]).

Table 1
Simulation models used in predicting the thermophysical properties of designed molten salts.

Thermophysical property	Simulation model	Reference
Phase diagram (liquidus temperature)	Factsage	[32]
	CALPHAD	[175]
Specific heat	Dulong-Petit method	[37]
	Mole fraction Average 1	[38]
	Mole Fraction Average 2	
	Molecular Dynamics (MD)	
Thermal conductivity	Average ionic Weight	[37]
	correlation	
	Mole Fraction average	
	Rough Hard Sphere (RHS)	
Viscosity	Polynomial Exploration	[37]
	Exponential Exploration	
	RHS method	
Density	Mole Fraction Average 1	[37]
	Mole fraction Average 2	[38]
	Mass Fraction average	
	Quasi Chemical Method (QCM)	
	Molecular Dynamics (MD)	

gallium (Ga), lithium (Li), sodium (Na), and lead-bismuth (PbBi) and also analyzed and discussed the critical issues like safety, compatibility with containment materials. The most common safety risks associated with sodium are its water and air reactions. Sodium reacts aggressively when it is in an open-air atmosphere and exposed to water, usually with an accompanying explosion caused by the secondary response of liberated hydrogen with oxygen in the air. Hence, an essential rule is to keep sodium completely isolated from water. When exposed to air in the absence of water, sodium may ignite spontaneously at a temperature as low as 120 °C depending on a range of factors such as air humidity and the surface-mass ratio of the sodium. At the temperatures of interest for CSP, most spillages of liquid sodium in the air can be expected to result in a fire [42]. The thermophysical properties of all the liquid metal categories would lead to higher efficiencies compared with conventional fluids such as water/steam, air, and molten salts due to their high boiling temperature, better chemical stability at high temperatures, higher conductivity, and higher heat transfer coefficient. However, a drawback of most liquid metal candidates is its low heat capacity making desired indirect storage medium which directly increases the costs of the CSP plant.

Thermophysical properties (heat capacity, thermal conductivity, viscosity, and density) of the molten eutectic salts depends on the composition of the individual salts and operating temperature. Each property of the molten salt can be expressed as a function of temperature. For example, in the case of NaCl–KCl–$ZnCl_2$, thermal conductivity of the eutectic salt with different composition is defined as follows (13.8NaCl-41.9KCl-44.3$ZnCl_2$; $k = 0.4372 - 1.23\times10^{-4}T$), (18.6NaCl-21.9KCl-59.5$ZnCl_2$; $k = 0.3895 - 8.169\times10^{-5}T$) and (13.4NaCl-33.7KCl-52.9$ZnCl_2$; $k = 0.5145 - 2.331\times10^{-4}T$). In the case of 68KCl–32$MgCl_2$; $k = 0.2469 + 5.025\times10^{-4}T$) [37]. A summary of the thermophysical properties of HTFs and liquid metals are provided in Table 2, and the prices of some readily available salts are also listed. The data of the key characteristics of the HTFs extracted from Table 2 are also plotted in Fig. 10. The melting temperature and thermal stability of the different molten salts and liquid metals are shown in Fig. 10(a) and (b). From Fig. 10(a), it is observed that the melting temperatures of the chloride salts are high compared to the nitrate salts and liquid metals. For reference, the U.S. Department of Energy goal calls for $T_{mp} < 250$ °C for molten salts and < 100 °C for metals. Among chloride salts, NaCl–KCl–$ZnCl_2$ has a low melting point of 229 °C. High thermal stability (under inert conditions) was observed in the case of chloride salts and liquid metals (> 800 °C), as shown in Fig. 10(b). Economic viability of thermal storage media is one of the most critical selection criteria for HTFs. The cost of molten salts and liquid metals is shown in Fig. 11.

Heat capacity, thermal conductivity, viscosity and density of the various molten salts at different temperatures are shown in Fig. 12(a), (b), (c) and (d), respectively. Nitrate salts, fluoride salts, and carbonate salts were found to have adequate heat capacity ($C_p > 1.5$) compared to the chloride salts [Fig. 12(a)]. Chloride salts and fluoride salts showed better thermal conductivity than nitrate salts Fig. 12(b). Among all the salts, NaCl–$MgCl_2$ and LiCl–KCl showed reasonable viscosity satisfying the U.S. Department of Energy goal ($\mu \leq 1.2$) [Fig. (12(c)]. The density data of the available molten salts plotted in Fig. 12(d) showed that all the salts satisfy the U.S. Department of Energy goal (≤ 6000 (at 300 °C) or ≤ 5400 (at 600 °C)). Based on the above data on the molten salt thermophysical properties, chloride and carbonate salts are the best candidates for high-temperature heat transfer and storage materials.

3. Corrosion in heat transfer fluids

Compatibility of the structural materials with HTFs and a storage medium is a crucial concern and a technical challenge in different CSP plant parts. Austenitic stainless steel can be used as the structural material for solar collectors, hot salt tank and the HTF pipes in a two-tank molten salt storage system while cold pipes, cold tanks, and preheaters are typically made of carbon steel. Nickel alloys are mainly used in the

Table 2
Thermophysical properties of heat transfer fluids.

Heat transfer fluid	Compositions[wt.%]	T_{mp} [°C]	T_{max} [°C]	μ [cp]	k [W/mK]	C_p [kJ/kgK]	ρ [kg/m^3]	Cost [$/kg]	Reference
Nitrate Salts									
Solar Salt	(60)$NaNO_3$-(40)KNO_3	223	565	4.68(300 °C)	0.55(300 °C)	1.5(400 °C)	1752 (500 °C)	0.8	[23]
Hitec	(7)$NaNO_3$-(53)KNO_3-(40)$NaNO_2$	142	535	3.16(300 °C)	0.2(300 °C)	1.56(300 °C)	1650 (600 °C)	0.93	[22]
Hitec XL	(7)$NaNO_3$-(45)KNO_3-(48)$Ca(NO_3)_2$	120	500	6.37(300 °C)	0.52(300 °C)	1.45(300 °C)	1740 (600 °C)	1.1	[22]
Li–Na–K nitrates	(30)$LiNO_3$-(57)$NaNO_3$-(13)KNO_3	128	596	8.71(300 °C)	NA	1.74(500 °C)	1784 (500 °C)	7.52	[23]
Li–Na–K nitrates/ nitrites	$LiNO_3$–$NaNO_3$– KNO_3–$NaNO_2$	82	635	11.7(160 °C)	NA	1.86(300 °C)	NA	1.347	[25]
Li–K–Ca nitrates	(0.25)$LiNO_3$-(50–80)KNO_3-(10–45)$Ca(NO_3)_2$	80	500	4.0(300 °C)	0.43(300 °C)	NA	1750 (400 °C)	0.6–0.8	[22]
Sandia Mix	(9–18)$NaNO_3$-(40–52) KNO_3-(13–21) $LiNO_3$-(20–27)$Ca(NO_3)_2$	<95	500	5-7(300 °C)	0.65(250 °C)	1.16–1.44 (247 °C)	NA	0.62–0.81	[47]
Quaternary nitrate salt	(5.58)$NaNO_3$-(44.17) KNO_3-(33.33) $NaNO_2$-(16.67)$Ca(NO_3)_2$ $4H_2O$	83	628	NA	0.65	1.52(440 °C)	1763 (500 °C)	NA	[28]
Solar salt-nanoparticles	$NaNO_3$–KNO_3-(5)MgO nano	NA	NA	3.24(300 °C)	0.55(300 °C)	1.58(300 °C)	1850 (400 °C)	NA	[31]
Chloride Salts									
LiCl–KCl	(45) LiCl- (55) KCl	355	>800	1.15(700 °C)	0.38(700 °C)	1.20(700 °C)	1520	5	[176] [32]
NaCl–$MgCl_2$	46 NaCl-54 $MgCl_2$	445	>800	1.36(700 °C)	0.95	1.09(700 °C)	1680	0.5	
KCl–$ZnCl_2$	(54) KCl-(46) $ZnCl_2$	432	>800	NA	0.83	0.67	NA	1.3	[177]
KCl–$MgCl_2$	(62) KCl-(38) $MgCl_2$	424	>800	3.38(700 °C)	0.44(700 °C)	1.01(700 °C)	1514 (700 °C)	0.5	[178]
NaCl–KCl–$ZnCl_2$	NaCl–KCl–$ZnCl_2$	229	>800	NA	0.3	0.81	2400	0.8	[179]
NaCl–KCl–$MgCl_2$	(27.5) NaCl-(32.5) KCl-(40.0) $MgCl_2$	400	800	NA	NA	1.11(500 °C)	1700 (600 °C)	0.35	[178]
NaCl–KCl–$MgCl_2$-nano	(27) NaCl-(51) KCl-(22) $MgCl_2$-(0.7) Al_2O_3 nanoparticles	398.8	820	NA	0.55(350 °C)	NA	1770 (450 °C)	NA	[33]
Carbonate salts									
Li–Na–K carbonates	(35)Li_2CO_3-(33)Na_2CO_3-(32)K_2CO_3	397	>650	4.3(800 °C)	NA	1.9(700 °C)	2000 (600 °C)	2.5	[164]
	LiF–Na_2CO_3–K_2CO_3	420	797	NA	1.17(375 °C)	1.90(375 °C)	2020 (600 °C)	NA	[180]
Fluoride salts									
LiNaK Fluorides	(46.5) LiF-(11.5) NaF-(42) KF	454	>700	6.78(500 °C)	1.27(500 °C)	1.8(500 °C)	2090 (500 °C)	>2	[181]
Liquid metals									
Li	Li	180	1347 (BP)	0.20 (1000 °C)	63.3 (1000 °C)	4.06(1000 °C)	436 (1000 °C)	11.82	[41]
Na	Na	98	883(BP)	0.21(600 °C)	46.0(600 °C)	1.25(600 °C)	835(500 °C)	2	
Sn	Sn	232	2687 (BP)	1.01(600 °C)	33.8(600 °C)	0.24	6330 (600 °C)	15.9	
Ga	Ga	29.8	2403 (BP)	0.69(700 °C)	59.5(700 °C)	3.75	5673 (700 °C)	252	
Galinstan	(66)Ga-(20.5)In-(13.5)Sn	19	>1300 (BP)	2.4	16.5	0.29	6440	450	
Na–K	(22.2)Na-(77.8)K	−12	785(BP)	0.18(600 °C)	26.2(600 °C)	0.87(600 °C)	NA	2	[72]
Pb–Bi	(44.5)Pb-(55.5)Bi	125	1533 (BP)	1.08(600 °C)	12.8(600 °C)	0.15(600 °C)	9710 (800 °C)	13	

piping sections of the plants that work at temperatures up to 700 °C [43–45]. Since structural corrosion of materials plays a vital role in the life cycle and cost of the plant, it is essential to determine accurate corrosion characteristics quantitively and qualitatively.

Generally, corrosion can be evaluated by the isothermal immersion method in which metal weight gain or loss is considered before and after immersion in the molten salt. A weight gain corresponds to the total weight of the reaction products on the sample surface; a weight loss signifies the alloy contribution to the corrosion products' weight in the corrosive environment. Quantitatively, corrosion can be calculated using the gravimetric method or descaling method, which analyzes the weight difference between the sample before and after exposure. The gravimetric method considers the weight gain due to oxide formation after immersion test. The descaling method considers the weight loss by removing the formed oxide layer by chemical cleaning without affecting the metal surface. In either case, the corrosion rate can be calculated as the mass change of the material over time per unit initial surface area of the material, S_o, given by Refs. [45,46] as follows:

$$\frac{\Delta m}{S_o} = \frac{m_i - m_f}{S_o} \tag{1}$$

The corrosion rate, CR, in $\mu m/y$ is then evaluated as

$$CR = \left[87600 \cdot \frac{\Delta m/S_o}{\rho_m t}\right] \tag{2}$$

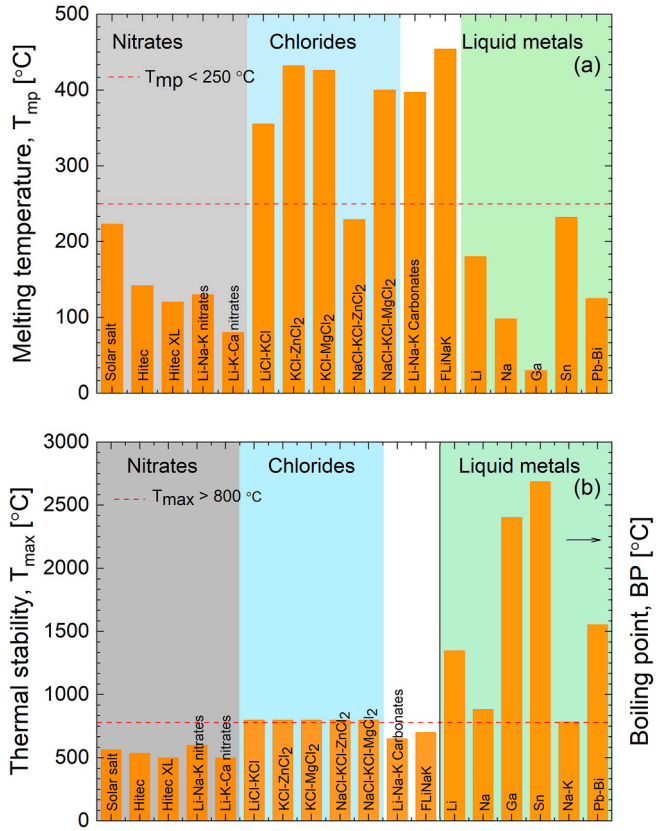

Fig. 10. Melting temperature and thermal stability of nitrate, chloride, carbonate, and fluoride based molten salts along with liquid metals.

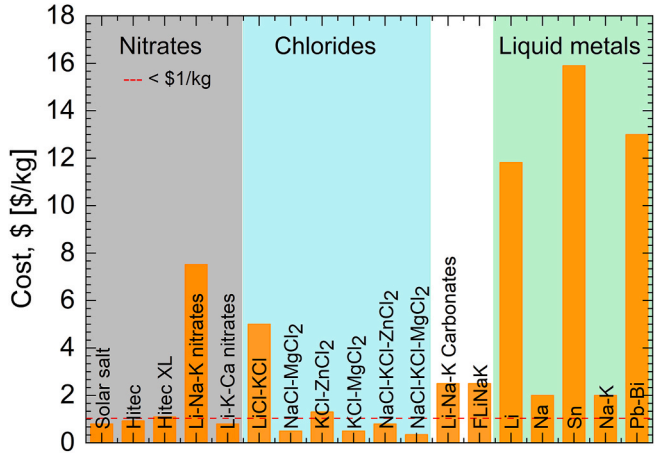

Fig. 11. Cost of nitrate, chloride, carbonate, and fluoride based molten salts along with liquid metals.

in which $\Delta m/S_o$ is the change of mass per area (mg/cm^2), ρ_m is the density (g/cm^3), t is the time of isothermal exposure (hours), and the constant 87600 accounts for the conversion to $\mu m/y$.

Accurate weight change cannot be obtained in the gravimetric method if some of the corrosion products are soluble in the solution. Descaled weight loss can be used as a principal measure of corrosion which eliminates uncertainties caused by corrosion products that may not be completely adherent. During the isothermal immersion method, the formed oxide layers should be removed to find an accurate weight loss. For corrosion rate calculations, the equations above can be applied in the descaling process; however, this method is based on the removal of the surface oxides from the metal surface after the corrosion test [47]. The descaling method consists of dissolving the corroded samples into an appropriate cleaning solution for a specified duration [48]. The solutions for cleaning the coupons should be selected as per ASTM Standards [49]. For example, formed oxide layers on carbon steel coupons can be removed with a negligible attack of the underlying metal by immersing the coupons in an inhibited HCl solution at room temperature and, similarly, stainless steel coupons can be descaled by boiling in alkaline permanganate [44].

In the case of Ni-based alloys, the method of chemical treatment guided by the ASTM is ineffective. McConohy and Kruizenga [50] developed a new method in which nickel based alloys washed in a hot $NaOH/KMnO_4$ bath for an hour, then washed in a hot diammonium citrate bath for an additional hour, and finally cleaned with deionized water. The corrosion data calculated from both the methods for various structural materials immersed in different molten salts—nitrates, chlorides, carbonates, and fluorides—at different temperatures are shown in Tables 3–6, respectively. The gravimetric method involves poor adherence, spallation, and solubility of oxides in the immersion fluid. It is challenging to remove formed oxides on Ni-based alloys using the descaling method. The gravimetric and descaling methods have limitations in finding the accurate corrosion since the sensitivity of the weight change measurements is limited to 0.1 mg. Other issues like different corrosion rates at different exposed areas when sample is partially immersed in a molten fluid and fluid/air interface. Besides, the above methods are very lengthy processes and only provide an average rate of corrosion over the exposed surface.

As an alternative, electrochemical methods are used to assess the corrosion rate of metals and alloys in molten salts. The main techniques involved are the Tafel technique, linear polarization, and electrochemical impedance spectroscopy, each of which has its limitations [51]. Fig. 13 illustrates an example of Tafel extrapolation where the slope of the linear part of the cathodic region is β_c and that of the anodic region is β_a, each in units of mV/decade. Corrosion potential, E_{corr}, and corrosion current density, j_{corr}, (A·cm^{-2}) are then derived from the intersection of the two linear regions asymptotes. Corrosion resistance R_{corr} (in $\Omega{\cdot}cm^2$) can be estimated from the parameters extrapolated from the Tafel plots by the Stearn-Geary equation [52] as:

$$R_{corr} = \beta_a \cdot \frac{\beta_c}{2.3(\beta_a + \beta_c)\cdot j_{corr}} \tag{3}$$

The intersection of the two Tafel lines represents an equilibrium between the kinetics of the cathodic and anodic reactions where the rates of those reactions are equal. The potential at this intersection is, therefore, the corrosion or open-circuit potential. The corrosion rate can be calculated using either anodic or cathodic reactions like $M_s \rightarrow M^{n+} + ne^-$, by relating current flow to mass via Faraday constant, as

$$Q = nFM \tag{4}$$

where Q is the transferred charge, n is the number of electrons transferred per molecule or atom of metal, F is Faraday constant, and M is the number of moles of metal being corroded. Substituting $M = m/AW$ where m is the mass of metal being corroded and AW is the atomic weight of the metal into equation (4) and rearranging, we get

$$m = \frac{(AW)Q}{nF} \tag{5}$$

By defining equivalent weight (EW) as $\frac{AW}{nF}$ and dividing equation (5) by time, we obtain corrosion rate (CR) as:

$$CR = K\frac{i_{corr}(EW)}{\rho_m \cdot A} \tag{6}$$

where A is the area of metal surface being corroded in units of cm^2, ρ_m is

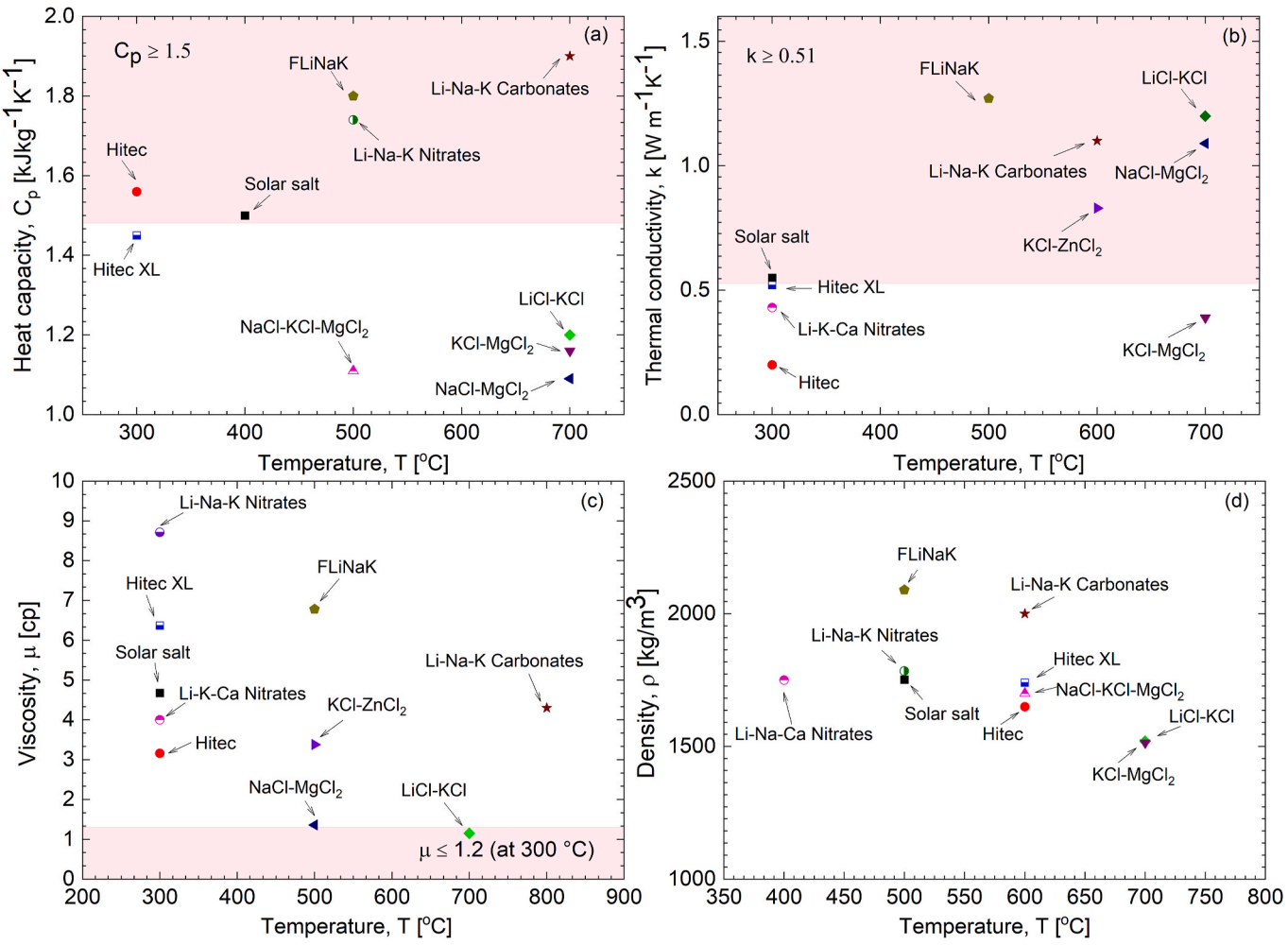

Fig. 12. Heat capacity, thermal conductivity, viscosity and density versus temperature of nitrate, chloride, carbonate, and fluoride based molten salts.

the metal density in units of g/cm^3, $K = 3.272\times10^6$ μm/(A·cm·y) and i_{corr} is the corrosion current in units of Ampere, such that *CR* is in units of μm/y.

Electrochemical impedance spectroscopy (EIS) has been used in recent years for studying corrosion of systems [53,54], including monitoring corrosion in CSP plants. An advantage of this technique is the low intensity of the excitation signal, which is less intrusive on the electrochemical system, making EIS a non-destructive technique that reduces measurement errors. However, EIS requires construction of an equivalent electrical circuit to correlate to X-ray diffraction (XRD) and SEM characterization of the physical phenomenon being studied. Because there is no single rate law to describe the corrosion kinetics with exposure time, some authors considered corrosion at a particular time of exposure, and others reported complete data at different exposure times.

The available corrosion data is summarized and presented in Tables 2–5 in units of μm/y by converting the mass loss or weight change data. In assembling the summary data, we have considered the longest duration of exposure time in this conversion. The collected data on corrosion of various alloys in molten salts (nitrates, chlorides, carbonates, and fluorides), supercritical CO_2 (sCO_2), and liquid metals are reported in Tables 2–9. The corrosion mechanism and analysis in different HTFs are explained in the following section.

3.1. Corrosion mechanism

In molten salts, materials degradation involves various mechanisms such as thermodynamically driven corrosion, impurity driven corrosion, localized corrosion, and mechanically assisted corrosion. Corrosion due to the presence of impurities is a significant issue in the molten salt used in CSP systems. Impurities such as moisture, hydroxides in chloride salts, Cl^- ions in nitrate and carbonate salts, as well as metallic impurities from containment systems accelerate the corrosion severely [55]. Localized corrosion occurs due to aggressive ions, creating small, deep indentations called *pitting corrosion* and preferential degradation of surfaces around a confined electrolyte volume called *crevice corrosion*. Localized corrosion breaks the passive film and affects the active metal. Mechanically assisted corrosion results in stress corrosion cracking under incidental loads and corrosion fatigue under repeated loads [56]. Impurity-driven corrosion was identified as the most severe attack on the materials at the initial stage. Fig. 14 shows the characteristic variation observed in these experiments conducted in closed convection loops at the U.S. Department of Energy's Oak Ridge National Laboratory [56,57]. The figure shows that the corrosion depth increases rapidly at the initial stages stemming from the impurities in the salt and at later stages, it is dominated by thermal gradient and other effects. The results point to the importance of removing impurities and salt purification in CSP molten salt systems.

The primary corrosion mechanism in various molten salts of nitrates, carbonates, chlorides, and fluorides is explained based on anion species present in the salt using an acid/base model like that adopted for corrosion in an aqueous solution [58]. The acid/base model is significant for explaining the major mechanisms of material degradation and removal in nitrate, sulfate, and molten carbonate salts (oxyanions salts). Generally, the oxyanion salts dissociate into ionic species upon heating

Table 3
Mass change and corrosion rate of structural materials in molten nitrate salts at various temperatures except Ref. [48] which is for $Ca(NO_3)_2$+ $NaNO_3$+ KNO_3.

Reference	Molten Salt	Metal	Temperature [°C]	Time [h]	Cover gas	$\Delta m/S_o$ [mg/cm^2]	CR [μ m/y]
[182]	$LiNO_3$+$NaNO_3$ +KNO_3	SS310	350	50	Air	1.2	266.46
				100		0.38	42.19
				350		0.7	22.20
				500		0.6	13.32
		SS316		50		0.9	197.34
				100		0.4	43.85
				350		0.6	18.79
				500		0.62	13.59
		SS321		50		1.5	331.81
				100		0.8	88.48
				350		0.4	12.64
				500		0.75	16.59
[48]	$Ca(NO_3)_2$+$NaNO_3$+ KNO_3	SS304	390	550	Air	0.025	0.49
				1000		0.03	0.33
				1500		0.01	0.07
				2000		0.02	0.11
		T-22		550		0.15	3.06
				1000		0.17	1.90
				1500		0.20	1.49
				2000		0.19	1.06
		TAISI430		550		0.003	0.06
				1000		0.05	0.56
				1500		0.06	0.45
				2000		0.07	0.39
[46]	$NaNO_3$+KNO_3	SS321	400	3064	Air	0.27	0.97
		SS347		1025		0.20	2.14
[183]	$NaNO_3$+KNO_3	Alloy 4130	500	100	Air	0.09	10.04
		SS316				0.08	8.77
		800H				0.002	0.22
[46]	$NaNO_3$+KNO_3	SS321	500	3064	Air	1.98	7.14
		SS347				1.28	4.59
[45]	$NaNO_3$+KNO_3	A516	500	100	Air	1.935	217.31
[184]	$NaNO_3$+KNO_3	SS304	500	360	Air	0.01	0.30
				720		0.02	0.30
				1440		0.04	0.304
				2160		0.06	0.304
		SS316L		360		2.92	88.92
				720		2.91	44.31
				1440		4.76	36.24
				2160		5.67	28.77
		In600		360		0.02	0.57
				720		0.11	1.58
				1440		0.08	0.57
				2160		0.06	0.28
[65]	$NaNO_3$+KNO_3	SS316	550	100	Air	0.15	16.44
				500		0.23	5.04
				700		0.31	4.85
				1500		0.30	2.19
				2000		0.35	1.91
		SS321		100		0.09	9.95
				500		0.19	4.20
				700		0.15	2.37
				1500		0.15	1.10
				2000		0.18	0.99
[185]	$NaNO_3$+KNO_3	P91	580	500	Air	4.30	96.58
				1000		20.0	224.61
[50]	$NaNO_3$+KNO_3	Ha230	600	3000	Air	7.25	23.60
		In625		1025		4.86	49.21
		Ha230	680	1025		72.30	688.85
		In625				58.70	594.39
[46]	$NaNO_3$+KNO_3	SS321	680	1025	Air	42.70	460.76
		SS347				42.05	451.47

and melting. The dissociation for an alkaline metal, R, is given by the reaction:

$$R_xAO_y \longleftrightarrow xR^{z+} + AO_y^{z-} \tag{7}$$

The oxyanions species further dissociate depending upon environmental conditions. In molten salts, this dissociation is the Lux-Flood model resembling an acid-base model in an aqueous solution. The dissociation reactions are shown below for carbonates, sulfates and nitrates [59].

$$CO_3^{2-} \longleftrightarrow CO_2 + O^{2-} \tag{8}$$

$$SO_4^{2-} \longleftrightarrow SO_3 + O^{2-} \tag{9}$$

$$NO_3^- \longleftrightarrow NO_2^+ + O^{2-} \tag{10}$$

which may be expressed more generally as

$$AO_y^{-z} \longleftrightarrow AO_{y-1}^{+2-z} + O^{2-} \tag{11}$$

Table 4
Mass change and corrosion rate of structural materials in molten chloride salts at various temperatures.

Reference	Molten Salt	Metal	Temperature [°C]	Time[h]	Cover gas	$\Delta m/S_o$ [mg/cm^2]	CR [μ m/y]
[73]	NaCl + $CaCl_2$+$MgCl_2$	In 625	600	504	Air	5.0	102.9
		Hastelloy X				6.3	133.21
		HastelloyB3				8.0	150.81
[186]	LiCl + KBr + $CaCl_2$	SS310	650	48	N_2	1.3	300.69
		CS				2.1	488.21
		Ni201				0.15	30.75
[187]	NaCl + KCl + $ZnCl_2$	C276	700	168	Ar	3.8	222.88
				336		1.0	29.32
				504		2.4	46.92
[188]	NaCl–KCl–$MgCl_2$	SS316	700	100	N_2	2.38	260.93
		In600				2.16	223.39
		In617				0.85	89.06
		In625				0.67	69.54
		Ha C-22				0.74	74.59
		Ha 276				1.05	103.46
[189]	NaCl + $MgCl_2$	SS316	500	240	Ar	0.37	16.90
			600			0.80	36.54
			700			4.49	205.11
[77]	$MgCl_2$ + KCl	HR224(Oxidized, 1050 °C, 4h)	700	175	Ar	2.4	146.86
				325		5.02	165.41
				505		10.2	216.30
		In702(Oxidized, 1050 °C, 4h)	700	175	Ar	1.02	65.46
				325		1.2	41.46
				505		2.0	44.47
[76]	LiCl + KCl	In702	750	170	Air	1.9	125.52
				335		4.1	137.45
				500		5.9	132.52
				675		11.9	197.99
				850		14.1	186.29
				1000		15.9	178.56

Table 5
Mass change and corrosion rate of structural materials in molten carbonate salts at various temperatures.

Reference	Molten Salt	Metal	Temperature[°C]	Time[h]	Cover gas	$\Delta m/S_o$ [mg/cm^2]	CR [μ m/y]
[76]	Li_2CO_3+ Na_2CO_3+K_2CO_3	In702	550	170	Air	0.15	9.90
				335		0.12	4.02
				500		0.15	3.36
				675		0.16	2.66
				850		0.18	2.37
				1000		0.2	2.24
		OC4	550	170	Air	0.3	–
				350		0.45	–
				500		0.44	–
				675		0.54	–
				850		0.61	–
				1000		0.55	–
		SS304	550	170	Air	0.20	12.8
				335		0.23	7.51
				500		0.32	7.0
				675		0.30	4.86
				850		0.2	2.57
				1000		0.05	0.54
[190]	Li_2CO_3+ Na_2CO_3+K_2CO_3	SS304	650	24	CO_2+O_2	7.6	3467
		SS316L				6.3	2877
		SS310S				1.2	555
[89]	Li_2CO_3+ Na_2CO_3+K_2CO_3	OC4	650	170	Air	3.5	–
				335		9.5	–
				500		9.5	–
				675		3.0	–
				850		4.5	–
				1000		4.7	–
		HR224	650	170	Air	0.5	33.37
				335		2.7	91.45
				500		5.0	113.47
				675		7.0	117.67
				850		21.0	280.34
				1000		22.0	249.63
[91]	Li_2CO_3+ Na_2CO_3+K_2CO_3	HR3C	700	2000	Air	3.32	–
[187]	Li_2CO_3+ Na_2CO_3+K_2CO_3	C-276	700	168	Ar	4.0	234
		In625				28	1729
		SS316				4.0	267

Table 6
Mass change and corrosion rate of structural materials in molten fluoride salts at various temperatures.

Reference	Molten Salt	Metal	Temperature[°C]	Time[h]	Cover gas	$\Delta m/S_o$ [mg/cm^2]	CR [μ m/y]
[191]	LiF-NaF-KF	SS316	650	100	Ar	1.0	109.63
[104]	LiF–NaF–KF	GH3535	650	200	Ar	1.5	74.15
				500		2.7	53.39
				700		4.4	62.14
		Ha-N	650	200		1.2	59.32
				500		2.3	45.48
				700		4.1	57.91
		MoNiCr	650	200		1.0	–
				500		2.1	–
				700		3.1	–
[192]	LiF–NaF–KF	Ha-N	700	100	Ar	25	2471.78
				200		35	1730.24
				500		43	850.29
				1000		50	494.35
		Ha-B3		100		25	2375.27
				200		34	1615.18
				500		46	874.09
				1000		57	541.56
[193]	LiF–NaF–KF	Ni–26W–6Cr	800	400	Ar	0.138	–
		GH3535				0.204	5.04
[194]	LiF–NaF–KF	In800H	850	500	Ar	29	639.89
		In617				30	628.70
		Haynes				51	996.12
		Ha-X				13	277.08
		Ha-N				4	79.09
[55]	LiF-NaF-KF	Ha-N	850	500	Ar	3	59.32
		Ha-X				13	277.08
		In617				30	628.70
		In800H				28	617.83
		Haynes				51	996.12
[195]	LiF–NaF–KF	800H	850	300	Ar	0.035	1.28
		GH3535				0.005	0.16

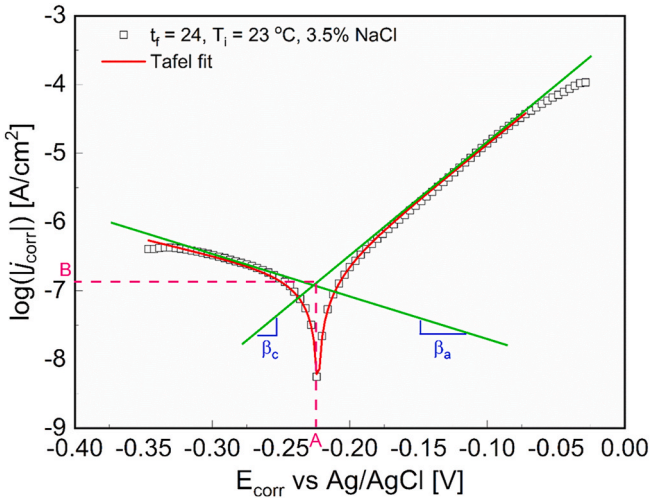

Fig. 13. Example of Tafel extrapolation of a polarization curve. The solid straight line (red) through data is the Tafel fit.

In the Lux-Flood acid/base model, the gas oxide species AO_y^{-z} and the oxide ions O^{2-} and AO_y^{-z} act as acid and base, respectively. The O^{2-} ion plays an essential role in defining the acidity or basicity of the molten salt, similar to the H^+ ion in an aqueous solution. When the O^{2-} activity is low in the melt, it leads to acidic dissolution in which the metal oxide will dissociate as metal ions and be soluble in the molten salt. When excess O^{2-} ions are present in the molten salt, the basicity reaction dominates and creates metal oxide anions, which may also be salt-soluble. The general dissolution reactions are given by [60,61]

$$M_xO_y \longleftrightarrow xM^{z+} + yO^{2-} \tag{12}$$

$$M_xO_y + zO^{2-} \longleftrightarrow M_xO_{y+z}^{2-} \tag{13}$$

The above mechanism applies to many oxyanion salts (nitrates, carbonates, sulfates, and hydroxides) within the melting temperature range of 400–800 °C.

Similarly, the Lux-Flood model can be applied to halide-based salts (chloride and fluoride) consisting of halide anions. The acid/base reactions are similar to the oxyanionic salts formed from the dissociation reaction given by

$$RA_y \longrightarrow R^{y+} + yA^- \tag{14}$$

where A^- and R^{y+} represent base and acid species according to the Lewis acid/base model. So, halide salts associated with alkali metals such as sodium, lithium, and potassium create a highly basic salt upon heating as they produce halide ions.

3.2. Nitrate salts

Nitrate-based salts like solar salt and HitecXL have been used in commercial CSP plants as high-temperature HTF and storage media [15,62]. Different research groups have studied the corrosion in these salts. Bradshaw and Goods did extensive work on nitrate-based molten salts at the U.S. Department of Energy's Sandia National Laboratories [63]. Some of their results are as follows. Corrosion performance of the alloys, SS304 and SS316, and carbon steel (A36) was evaluated in different binary and ternary eutectics of $NaNO_3$, KNO_3, and $Ca(NO_3)_2$ salts. Descaled weight loss was used to determine corrosion rates, and the oxidation products were characterized by SEM, electron microprobe analysis (EMPA), and XRD. In the case of binary nitrate salts, the annualized mass loss rate ranged from 6 to 15 gm/y for SS304 and SS316 at 570 °C, based on eutectic composition. Isothermal tests suggested that the short-term corrosion rate of stainless-steel followed a parabolic kinetics in the mixtures. The complex, multiphase oxides found to be formed on the surface of SS304 and SS316 coupons were composed

Table 7
Corrosion rate of different structural materials in molten $NaNO_3$+KNO_3 at different temperatures.

Reference	Metal	Temperature[°C]	Time[h]	Cover gas	$\Delta m/S_o$ [mg/cm^2]	*CR* [μ m/y]
[157]	CS	310	1500	Ar	Isothermal	8.8
[46]	SS321	400	3064	Air	Static immersion	1.0
	SS347					0.7
	SS321	500	3064	Air		7.1
	SS347					4.6
[184]	SS304H	500	1440	Air	Static immersion	0.27
	SS321L					36.25
	In600					0.61
[66]	SS304	530	Not reported	Air	Potentiodynamic	63.4
	SS316					41.7
	In600					38.9
	In825					26.5
[65]	SS316	550	3000	Air	Static immersion	8.6
	SS321					9.0
[185]	P91	580	1000	Air	Static and dynamic immersion	210
[196]	SS316	600	3000	Air	Static immersion	8.4
	SS347					8.8
[50]	HA230	600	3000	Air	Static immersion	23.6
	In625		1025			16.8
	HA230	680	1025	Air	Static immersion	688
	In625					594
[46]	SS321	680	1025	Air	Static immersion	460
	SS347					447

Table 8
Corrosion rate of different structural materials in molten chloride salts at various temperatures.

Reference	Metal	Molten chloride salt	Temperature[°C]	Time[h]	Cover gas	Method	*CR* [μ m/y]
[74]	C-276	NaCl + KCl + $ZnCl_2$	500	840	Air	Potentiodynamic polarization	42
	C-22						50
	SS304						381
	N-type						120
[73]	In625	NaCl + $CaCl_2$+$MgCl_2$	600	504	Air	Isothermal immersion	121.09
	Ha X						153.16
	Ha B3						144.59
[186]	SS310	LiCl + $CaCl_2$+KBr	650	48	N_2	Potentiostatic polarization	290
	CS						480
	Ni 201						30
[197]	SS310	NaCl + LiCl	650	–	N_2	Potentiodynamic polarization	7490
	In800H						5940
	In625						2800
	SS347						6240
[75]	SS310	NaCl + KCl + $MgCl_2$	700	500	Ar	Isothermal immersion	1581
	In800H						364
	C-276						79
[179]	SS316	NaCl + KCl + $ZnCl_2$	700	500	Air	Isothermal immersion	1700
	In625						447
	C-276						668
	In718						962
[187]	SS316	NaCl + KCl + $ZnCl_2$	700	504	Ar	Isothermal immersion	892
	C-276						55
	In625						7
[142]	SS304	NaCl + KCl + $MgCl_2$+	720	8	Ar	EIS	8190
	HR224						3120
	In702						6340
[77]	HR224	$MgCl_2$+KCl	700	72	Ar	EIS	224
	In702						136
[76]	In702	LiCl + KCl	750	100		Isothermal immersion	120
[72]	C-276	NaCl + KCl + $ZnCl_2$	800	245	Sealed	Isothermal immersion	10
	C-22						12

mainly of iron oxides, iron-chromium spinel, and sodium ferrite, whereas magnetite was formed as the main corrosion product on A36.

Soleimani et al. [64] investigated corrosion resistance of ferritic steels (P91 and X20CrMoV11-1) austenitic steels (SS316 and SS347H) and a Ni-alloy, Inconel 625 (In625), by isothermal immersion in solar salt at 600 °C for long run duration of 5000 h. P91 and X20CrMoV11-1 were found to lack long-term corrosion protection from molten nitrate salts. However, protective oxide scales were formed on stainless steel SS316 and SS347H with similar kinetics. It was also found that the oxides were formed as alkali ferrites on stainless steel. A linear weight loss with the best protective layer was observed for In625 and electron probe micro analysis (EPMA) results revealed that a multiphase oxide layer composed of Fe oxides, Fe–Cr spinel, and sodium ferrite developed on SS347H, whereas In625 surface was covered primarily with a dense NiO layer.

Corrosion of SS316L and SS321H austenitic stainless steels was analyzed after isothermal immersion test conducted in solar salt at 550 °C in the presence of atmospheric air for 3000 h [65]. In the results, it

Table 9
Corrosion rate of different structural materials in molten carbonate salts at various temperatures.

Reference	Metal	Molten carbonate salt	Temperature[°C]	Time[h]	Cover gas	Method	*CR* [μ m/y]
[198]	SS316	Li_2CO_3+K_2CO_3+Na_2CO_3	450	1000	Air	Static Immersion and EIS	176
[199]	SS316	Na_2CO_3+Li_2CO_3+K_2CO_3	600	1440	Air	Dynamic Gravimetric Analysis	1030
[162]	In800H	Na_2CO_3+Li_2CO_3+K_2CO_3	600	24	N_2	Potentiodynamic polarization	451
[200]	P91	Na_2CO_3+Li_2CO_3+K_2CO_3	650	1000	Air	Static and dynamic Immersion	2686
[190]	SS304	Li_2CO_3+K_2CO_3+Na_2CO_3	650	24	CO_2+O_2	Potentiodynamic polarization	3500
	SS316						2900
	SS310						500
[187]	SS316	Li_2CO_3+Na_2CO_3+K_2CO_3	700	504	Ar	Static Immersion	94
	C-276						229
	In625						1729
[187]	SS316	LiF + Na_2CO_3+K_2CO_3	700	504	Ar	Static Immersion	275
	C-276						77
	In625						12
[162]	SS310	K_2CO_3+Na_2CO_3	750	24	N_2	Potentiodynamic polarization	1560
	SS321						4640
	SS347						2360
	In800H						1080
	AFA OC-6						1570
	In625						2600

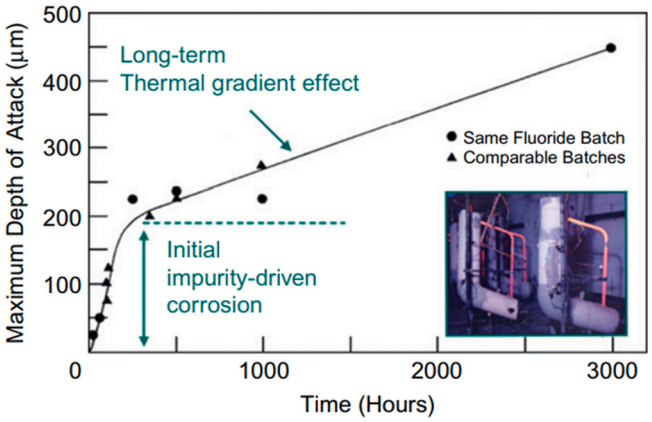

Fig. 14. Impurity driven and thermal gradient corrosion (reproduced with permission from Ref. [55]).

was found that multilayers of various oxides, mainly Fe_3O_4, and Fe_2O_3 are formed on the surfaces of 321H (7.5 ± 2.9 μm) and 316L (6.9 ± 2.1 μm). A minimal change of the molten nitrate salt composition was noted in time owing to the formation of soluble chromate and nitrite products resulting from the thermal decomposition of nitrate ions. Recently, Wang et al. [66] studied the corrosion behavior of X80 carbon steel, SS304, SS316L, and nickel alloys, 600 and 825, in molten salt mixture. Corrosion tests were performed at different temperatures using static and dynamic immersion tests and electrochemical scan. It was observed that the corrosion resistance of the tested alloys in molten salt at 530 °C followed the sequence of SS304 < SS316L < In 825. They concluded that corrosion under dynamic conditions was more severe than that under static conditions. A N_2 atmosphere was seen to protect the alloys against corrosion in high-temperature molten salts.

Corrosion performance and mechanism of three austenitic stainless sheets of 310S, 316L, and 321 were studied experimentally in a new quaternary eutectic salt KNO_3–$NaNO_2$–$NaNO_3$–KCl [67]. The composition of the corrosion products and their morphology were analyzed using XRD and SEM with energy dispersive X-ray analysis (SEM-EDX). The cross-sectional SEM images and EDX mapping of 310S, 316L, and 321 are shown in Figs. 15 and 16. The cross-sectional morphology is divided into the resin layer, corrosion layer, and metal matrix. From the figure, the corrosion layer thickness of the 310S, 316L, and 321 stainless sheets of steel is found to be approximately 2.55 μm, 3.40 μm, and 4.17 μm which can also be observed from the EDS of the elemental distribution map as shown in Fig. 16(a)–(c). A dense Fe_3O_4 oxide layer was found on the surface of 310S that contributes to good corrosion resistance and prevents the diffusion of oxygen. In case of 316L, Fig. 15(b), it can see that funnel-shaped pits were observed on the inside of the corrosion layer composed of thicker outer layer of Fe_2O_3 and a thinner inner layer of $NiCr_2O_4$. Similar cross-sectional corrosion morphology with many corrosion holes ranges from 0.4 to 1.6 μm observed in 321, as

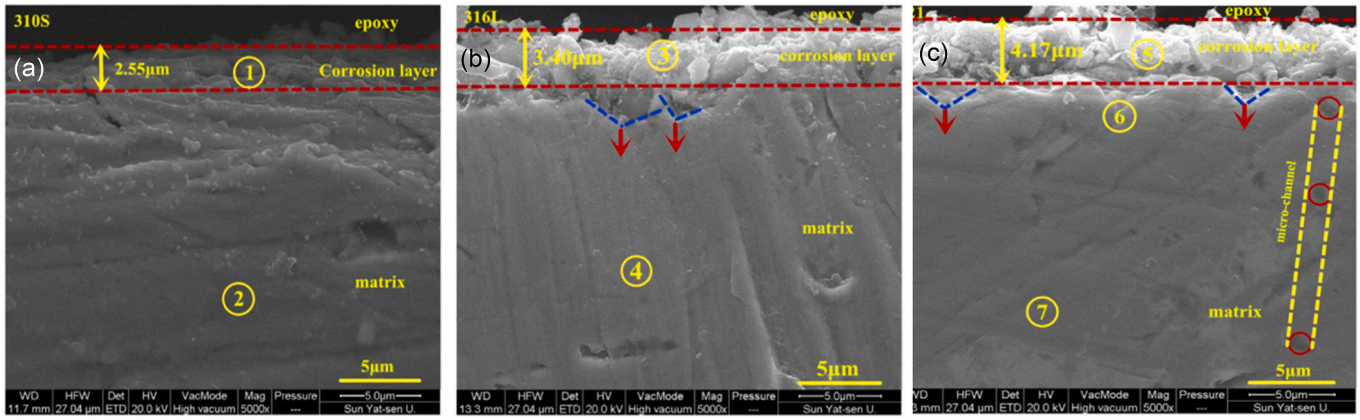

Fig. 15. Cross sectional scanning electron microscope images of 310S, 316L, and 321 immersed in nitrate salts at 500 °C for 42 days (reproduced with permission from Ref. [67]).

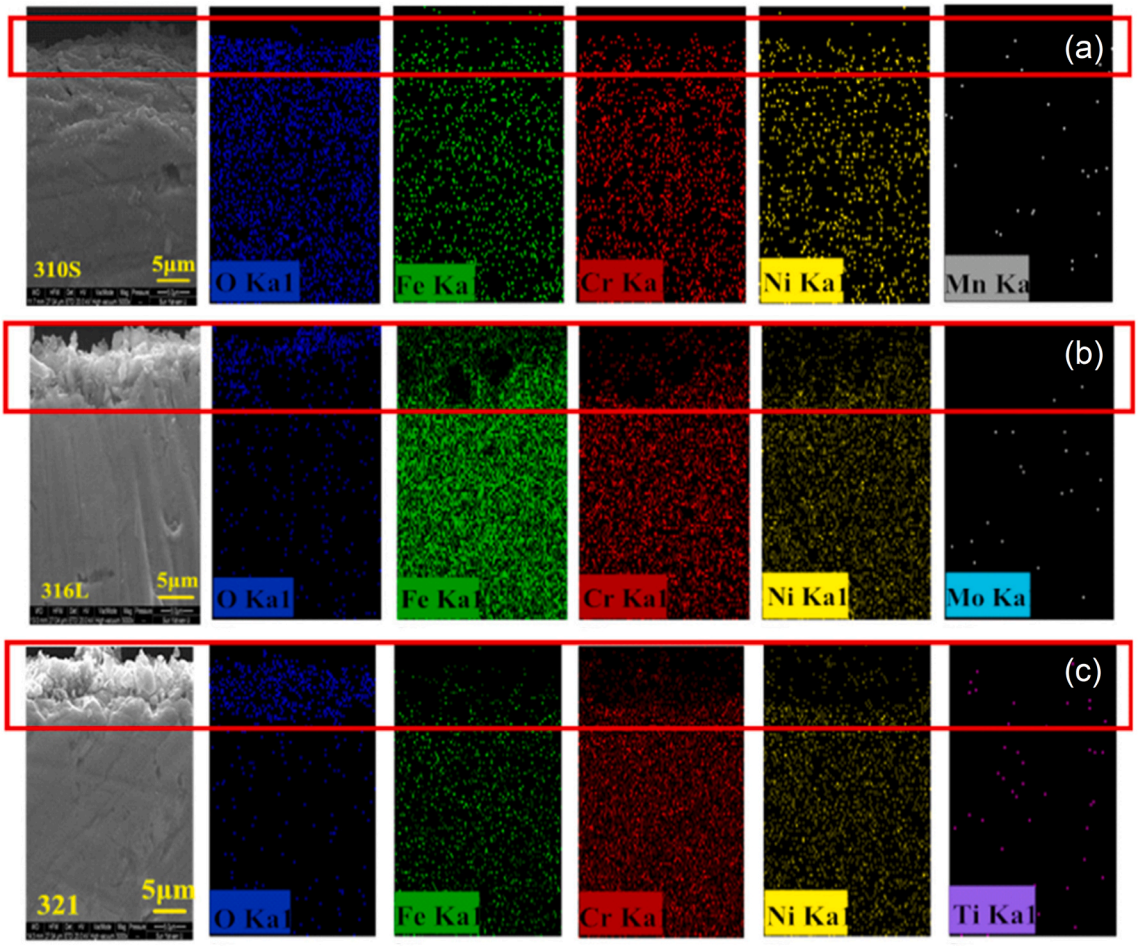

Fig. 16. EDS mapping of 310S, 316L, and 321 exposed to nitrate salts at 500 °C for 42 days (reproduced with permission from Ref. [67]).

shown in Fig. 16(c). In comparing Fig. 16(a), (b), and (c), there are significant Cr-depleted zones in 316L and 321, except for 310S, and these regions may lead to intergranular corrosion especially when the Cr content is lower than 12.5%. It is expected that phases of FeCr, TiC compounds precipitate at the grain boundaries of 316L, and 321 easily dissolved in a strong oxidizing medium. Both 316L and 321 have an apparent Cr depletion region resulting in intergranular corrosion. 310S showed the best corrosion resistance in this quaternary molten salt compared to 316 and 321L. Mo and Ti could not inhibit intergranular corrosion but accelerated the dissolution of σ-phase and TiC in the quaternary molten salt.

The thermal stability of solar salt chemistry can be affected by purging gas and operating temperature over time. Bonk et al. [68] reported that a quick stabilization of the nitrite content is established whereas nitrate content remains constant over 500 h in synthetic air. In a nitrogen atmosphere, the nitrite content steadily increases (up to 15 mol%) after 500 h at 560 °C. However, the nitrate content decreases as a result, and no equilibrium nitrate/nitrite ratio is reached. But, without gas purging and in an open atmosphere, a stable nitrite content is reached, and carbonate content is observed deriving from reactions of molten nitrate with atmospheric CO_2. The thermal stability of solar salt at high temperatures and long durations depends on the gas phase chemistry and the impurities present in the molten salt. At high temperatures, decomposition of the nitrite ion into oxide ions (e.g. O^{2-}) and different gaseous species such as nitrous gases (NO, NO_2), nitrogen (N_2) or oxygen (O_2) can be observed. The formed toxic nitrous gases and oxide ions lead to aggressive corrosion [69].

Bonk et al. [70] investigated the impact of molten salt chemistry, changed by the gas atmosphere and artificial chloride impurities, on the corrosion behavior of AISI 316Ti and AISI A213/T91. They concluded that the molten salt chemistry could directly be affected by the composition of the surrounding air flow atmosphere. A stable nitrate/-nitrite level was obtained with synthetic air flow, but excessive nitrate decomposition, nitrite formation, and oxide formation occurred in N_2 flow. They also demonstrated that molten salt aging impacted not only the corrosion rate but also the corrosion mechanism. Further, chromium dissolution was observed during the corrosion of SS 316Ti when solar salt was stored under N_2 atmosphere, which was ascribed to unusually high nitrite and oxide contents, formed by the steady decomposition of the nitrate melt. Federsel et al. [16] investigated the chemical reaction network of molten nitrate/nitrite salt mixtures in Hitec salt at high temperatures (>450 °C). Thermal stability results showed that at low temperatures a significant mass loss was observed within 20 days. At 500 °C, a daily mass loss of 0.2% could be observed which increased ten times higher at 550 °C in synthetic air.

Sötz et al. [71] investigated the effect of NOx in the purge gas on the chemical composition of the solar salt. They demonstrated that the concentration of oxide ions can be controlled by adjusting the partial pressures of the purge gas. The oxide ion formation in solar salt is based on equilibrium reactions and stabilizes in the presence of NO_x gas in the synthetic air purge. The stabilizing effect was demonstrated experimentally for two relevant temperatures (600 and 620 °C) in laboratory tests for about 1000 h. Stepwise increase of the concentration of nitrous gases remarkably reduced the formation of oxide ions. At 600 °C, the stabilization was achieved for 100 ppm NO_x and higher, and at 620 °C, 500 ppm was required to keep the oxide content at a low level. These results help in reducing steel corrosion under specific gas operating conditions for solar salt applications. McConohy and Kruizenga [50]

studied the thermophysical properties and corrosion studies of Ni-based alloys in solar salt at high temperatures of 600 °C and 680 °C. The DSC measurements showed that for the most extreme case, 680 °C operating temperature for 2000 h, the salt displayed a melting point of 156 °C, nearly 70 °C lower than the melting point of pure solar salt. The primary reason for the reduction in melting point was attributed to the presence of high nitrite concentrations in the molten salt. The results of this test indicate that the nitrate/nitrite equilibrium is responsible for the majority of physical changes that occur within the salt mixture.

The data collected from the various studies on corrosion of structural materials in the nitrate-based molten salts are summarized in Tables 3 and 7, while the corrosion rate of the structural materials in nitrate-based molten salts at different temperatures is shown in Fig. 17. The figure shows that nitrate salts are suitable for lower temperatures of less than about 600 °C. The region marked Gen3 in Fig. 17 represents the temperature range and maximum corrosion rate stipulated by the U.S. Department of Energy's targets for Gen3 CSP plants. It is evident that none of the existing studies summarized from the literature currently meets the Gen3 targets, which represents a challenge and an opportunity for future development.

3.3. Chloride salts

Next-generation solar thermal power conversion systems target high temperature and advanced fluids that will be operated in the range of 600–800 °C, which surpasses the limits on thermal stability of nitrate salts [72]. Chloride-based salts are promising candidates for HTF and energy storage materials, due to their thermal stability and low cost. These advantages permit them to be used at a temperature greater than 600 °C, enabling higher thermal-to-electrical energy conversion efficiency.

Vignarooban et al. [73] studied corrosion of Ni-based alloys of Hastelloy X (H X), In625, and Hastelloy B-3 (H B-3) in NaCl–$CaCl_2$–$MgCl_2$ salt using gravimetric techniques. The corrosion behavior was quantified in terms of mass loss of samples at different time instants. The results showed that In625 alloy was more corrosion resistant than H B-3 and H X and alloys. A compact protective layer of $MgCr_2O_4$ attached to the In625 and H X alloys surfaces inhibits the corrosion. The steady-state potentiodynamic method was used to estimate corrosion rates for commercial Hastelloy C-22, C-276 and N types in eutectic molten salts [74]. Hastelloy C-276 exhibited the least corrosion rate of 10 μm/y at 250 °C and 40 μm/y at 500 °C in 13.4NaCl–33.7KCl–52.9$ZnCl_2$ (mol%) salt. Hastelloy N, despite its higher Ni content of 71%, showed a higher corrosion rate than C-22 and C-276 owing to its low chromium content (7%). Immersion tests were conducted on high temperature corrosion behavior of three commercial alloys of S310, Incoloy 800H, and Hastelloy C-276 in molten $MgCl_2$–NaCl–KCl (60-20-20 mol%) at 700 °C for 500 h under inert atmosphere [75]. SS310 demonstrated the highest corrosion rate, while Hastelloy C-276 exhibited the highest corrosion protection. Microstructural analysis on the exposed alloy specimens revealed that Cr dissolved constructively over Fe and Ni results a porous layer during isothermal immersion. Moreover, the corrosion products, such as MgO, $MgCr_2O_4$, etc., were found to be precipitated in the pores of the Cr-depleted corrosion layer in addition to the surface of the exposed specimens. They proposed that an impurity of $MgOH^+$ reacts with the Si and Cr in the alloy materials.

Fernandez and Cabeza [76] investigated the corrosion behavior of different alumina-formed austenitic alloys (AFA) in lithium-based molten salts. The temperature range was found to improve by reducing the melting point and improving the thermal stability [76]. In their results, In702 showed the best corrosion resistance owing to the growth of protective layers comprised mainly of $NiCr_2O_4$ and Al_2O_3. Based on EIS measurements, corrosion models were proposed, as shown by the Nyquist plot and its respective equivalent circuit in Fig. 18. The corrosion scale is considered a capacitor, which is related to the double-layer capacitance at the interface of the salt and the scale, as represented by the equivalent circuit of Fig. 18. In the figure, C_{ox} is the oxide capacitance and R_{ox}, the transfer resistance of ions present in the scale [77]. The second, low frequency, loop corresponds to the corrosion process due to ion transport in the surface layer of the material. Further, R_s represents the resistance of the molten-salt (electrolyte), R_t denotes the electrochemical transfer resistance or polarization resistance of the material, C_{dl} is the double layer capacitance at the salt/metal interface, and n_{dl}/n_{ox} represents the coefficient of constant phase element of the first and second capacitance loop [54].

Recently, the same researchers [78] examined the corrosion of SS304 and two Ni-based materials—Inconel 702 (In702) and Haynes 224 (HR224)—in eutectic ternary KCl (20.4 wt%) + $MgCl_2$ (55.1 wt%) + NaCl (24.5 wt%) molten salt at 720 °C for 8 h. The corrosion mechanism and corrosion rate were characterized through EIS. Further, Fig. 19 shows XRD patterns of SS304, HR224, and In702 in the ternary chloride

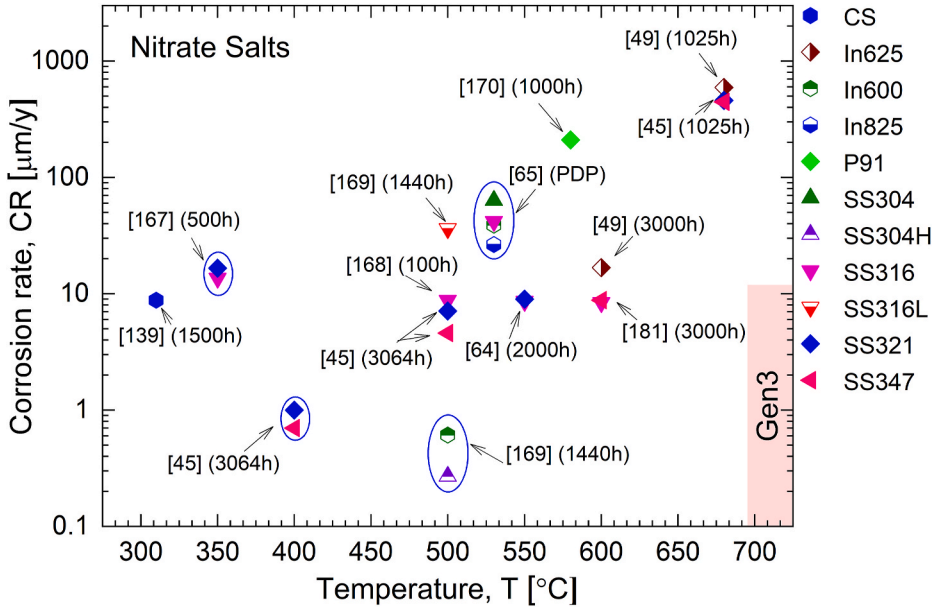

Fig. 17. Corrosion rate of different structural materials in terms of temperature for corrosion in nitrate salts.

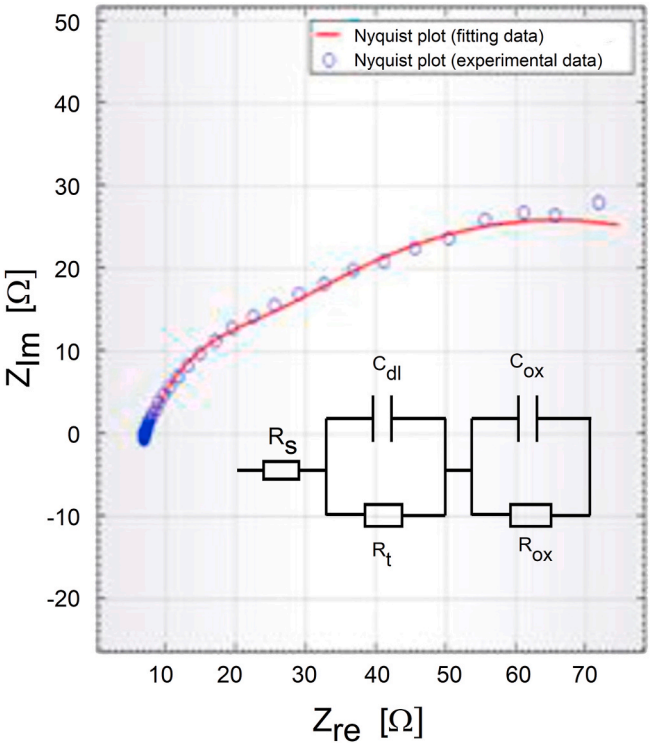

Fig. 18. Nyquist plot from EIS study in saline LiCl (45 wt%) + KCl (55 wt%) at 750 °C for 24 h (reproduced with permission from Ref. [77]).

molten salt at 720 °C after 8 h of immersion. The lower corrosion rates for HR224 and In702 alloys, due to internal oxidation composed by $MgCr_2O_4$ and an external layer of Al_2O_3, were confirmed from the XRD and SEM analysis. Guo et al. [79] studied the corrosion performance of binary alloys of Ni-xAl (x = 6, 10, and 15 at. %) in a binary $ZnCl_2$–KCl molten salt at 700 °C under oxygen atmosphere. It was observed that porous oxide scales were strongly enhanced by $ZnCl_2$–KCl deposits, and internal attack on the alloys induced by chlorine. But the formation of aluminum oxide layer acted as corrosion protection. The concentration of aluminum enhances the thickness of Al_2O_3, which may obstruct the rapid migration of the reactants.

Oxygen gas is a strong oxidant in molten chloride salt. Corrosion of stainless steels and Inconel alloys in molten chloride salts under reactive atmospheres such as air or Ar-10% O_2 was significantly enhanced in comparison with the corrosion of the same materials under an argon atmosphere [80,81]. The corrosion behavior of steel containers may be affected by water and other impurities in the mixture, particularly if the containers are filled with air [82]. The data collected from the studies on corrosion of various containment materials in chloride-based molten salts are summarized in Tables 4 and 8, while the corrosion rate of the structural materials in chloride-based molten salts at different temperatures is presented in Fig. 20. The figure shows that the Ni-based alloys, C-22 and C-276, exhibited the lowest corrosion rate and are suitable for next-generation CSP applications.

3.4. Carbonate salts

Molten carbonate eutectic salts and their blends with additional molten salts can be useful operational media in a wide range of high-temperature applications, primarily in the field of renewable and sustainable energy [83–86]. Ternary and binary carbonate eutectics like Li_2CO_3–Na_2CO_3–K_2CO_3 and Na_2CO_3–K_2CO_3 exhibit excellent thermophysical properties and have high thermal stability up to 850 °C, and these mixtures could be used as HTF and latent TES [87]. TES systems operating with carbonate eutectics and compatible to work with supercritical CO_2 (sCO_2) as HTF are crucial in developing high temperature CSP. With sCO_2, temperature as high as 1000 °C can be achieved [88]. In addition, carbonate eutectic salts used in such applications can also absorb carbon dioxide and convert it into carbon monoxide (CO), mono carbon (C), and carbon nanoparticles.

Corrosion of structural materials in molten carbonate salts at high temperatures has received much attention. Alumina-forming austenitic (AFA) alloys, such as modified OC4 and HR224, were examined in a ternary carbonate eutectic of 32.1%Li_2CO_3-34.5%K_2CO_3-33.4%Na_2CO_3 at a temperature of 650 °C for 1000 h [89]. It was found that structured layers with different chemical compositions were formed on both alloys after exposure. The authors reported multilayer structure formed with a steady state for OC4 and near steady state for HR224, as shown in Fig. 21. It was noted that one corrosion product of Ni and two types of corrosion products were formed on OC4 and HR224, respectively, possibly due to high Ni content in HR224. An irregular interface observed in HR224 due to precipitation of $NiFe_2O_4$ and $CrFe_2O_4$ spinels at the instability interface [90]. However, on both the alloys, the formed NiO acts as protective corrosion layer [91].

The considerable volume of molten salt required in CSP applications may produce a large amount of CO_2 by partial decomposition. The developed CO_2 will enhance corrosion when it mixes with O_2 impurity. Sah et al. [92] studied corrosion behavior of austenitic stainless steels of SS304, SS316L, and SS310S in 0.43Li_2CO_3-0.32Na_2CO_3-0.25K_2CO_3 carbonate melt under a controlled CO_2–O_2 environment. Fig. 22 shows the cathodic polarization curves of SS304 stainless steel in carbonate eutectic salt under various CO_2–O_2 ratios. Cathodic current increases with increasing O_2 partial pressure, which may be due to presence of derivatives of O_2 like peroxide or superoxide [93,94]. CO_2 partial pressure also influences the cathodic current as it is involved in the reduction reaction. But, under a pure CO_2 environment, low cathodic current is observed which supports that CO_2 speeds up cathodic reduction only when combined with O_2. It was found that for 99.30 kPa CO_2-2.03 kPa O_2 gas mixture, 316L and 304 showed high corrosion compared to 310S.

Corrosion behavior of austenitic steel HR3C was studied in a eutectic ternary Li_2CO_3–Na_2CO_3–K_2CO_3 molten salt mixture by conducting an isothermal immersion test at 700 °C for 2000 h [91]. The weight of the specimens was measured at different intervals of time (0, 24, 72, 168, 250, 500, 750, 1000, 1250, 1500, 1750, and 2000 h). The authors noticed that the mass loss occurred between the first 24 and 72 h and a constant mass gain was observed up to 750 h. After 750 h, the weight of the substrates improved slightly up to 2000 h. Sarvghad et al. [95] examined compatibility of duplex steel 2205, stainless steel 316, and carbon steel 1008 with the eutectic mixtures of NaCl + Na_2CO_3 and Li_2CO_3 + K_2CO_3 + Na_2CO_3 at 700 °C and 450 °C in the presence of air, respectively. They found that oxidation was the primary corrosion attack mechanism in both molten salt environments, and the availability of oxygen controlled the degree of oxidation. Grain boundary oxidation was observed in alloys in chloride/carbonate at 700 °C whereas no localized degradation was seen in ternary carbonate salt at 450 °C. Intragranular attack also observed in alloys 316 and 2205 due to depletion of alloying elements through the grain boundaries at 700 °C.

In carbonate molten salts, oxide ions, O^{2-}, and carbonate ions, CO_3^{2-}, play an essential role in the oxidation of the constituent elements in alloy materials. At equilibrium, the oxide ions emerge by self-dissociation.

$$CO_3^{2-} \leftrightarrow CO_2 + O^{2-} \tag{15}$$

When the alloys are immersed in a molten carbonate salt at high temperatures, the alloys form respective metal oxides as oxide ions react with the metals present in the alloys as well as in the molten salt by following reaction [96]:

$$M + \frac{n}{2} CO_3^{2-} \leftrightarrow MO_{\frac{n}{2}} + \frac{n}{2} CO_2 + ne^- \tag{16}$$

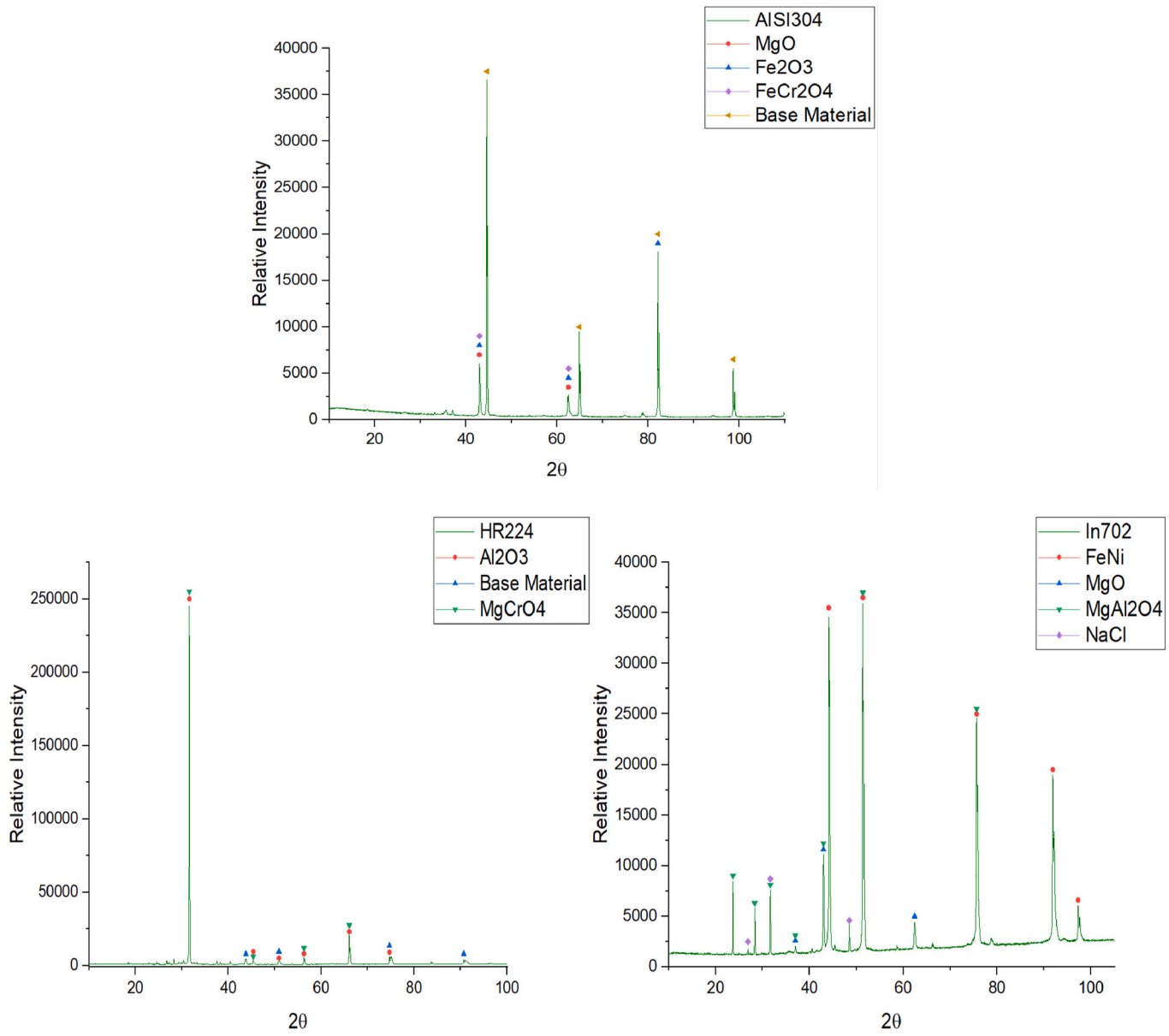

Fig. 19. XRD patterns of SS304, HR224 and In702 in KCl (20.4 wt%) + $MgCl_2$ (55.1 wt%) + NaCl (24.5 wt%) molten salt maintained at 720 °C for 8 h (reproduced with permission from Ref. [78]).

Since Fe and Cr are the major constituent elements in Fe-based alloys, and Ni in the case of Ni-based alloys, the possible reactions with Fe, Cr, and Ni in the oxidation process in Li-based chloride salts are as follows:

$$Cr + Li^{+} + 2CO_3^{2-} \rightarrow LiCrO_2 + 2CO_2 + 3e^{-} \quad (17)$$

$$Fe + CO_3^{2-} \rightarrow FeO + CO_2 + 2e^{-} \quad (18)$$

$$Ni + CO_3^{2-} \rightarrow NiO + CO_2 + 2e^{-} \quad (19)$$

Generally, during the oxidation process, the metal constituents will out-diffuse, and the dissociated ions (oxide and carbonate) present in the salt will down-diffuse, which forms oxides on the surface of the substrates. In Fe-based alloys, at the initial stage, chromium oxide will act as a protective layer to prevent the out-diffusion of metal ions.

In carbonate molten salts, purging gases (CO_2 and O_2) play an important role in maintaining the salt stability and corrosion rate of exposed alloy materials. The influence of CO_2 and O_2 partial pressures on the corrosion behavior of SS310 and SS316 were studied in a molten 52 mol% Li_2CO_3–48 mol% Na_2CO_3 salt at a temperature of 580 °C [97]. The corrosion rates were measured as the weight loss of 316L and 310S stainless steel samples after out-of-cell tests for 100 h at 580 °C by varying the partial pressure of each gas from 0 to 0.6 atm CO_2 and the balance being argon. A high corrosion rate was observed in Ar–CO_2 at 0.1 atm for both the alloys (SS310: 12 mg/cm^2 SS316: 14 mg/cm^2) whereas a constant corrosion rate (SS310: 1 mg/cm^2 SS316: 3 mg/cm^2) was found in Ar–O_2 atmosphere even up to 0.6 atm. High corrosion rate at partial pressure 0.2 atm or above is due to saturation of dissolved CO_2 in Li/Na electrolyte. The dissolved CO_2 is considered to possibly involve two corrosion mechanisms as follows: (1) as CO_2 dissolves in the Li/Na electrolyte, the electrolyte becomes more acidic, and this higher acidity makes the metal oxide scale more soluble in the electrolyte, consequently, leading to an enhanced corrosion rate; (2) the dissolved CO_2 can play an important role in deciding the composition of the metal oxide scale.

Further, the corrosion behavior of SS316L and oxide-dispersion

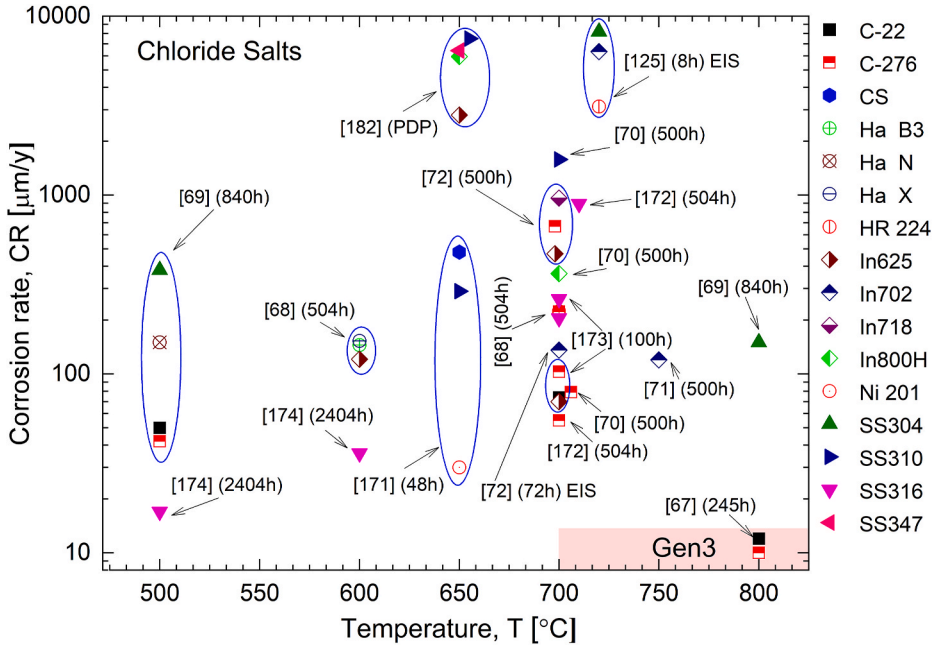

Fig. 20. Corrosion rate of different structural materials in terms of temperature for corrosion in chloride salts.

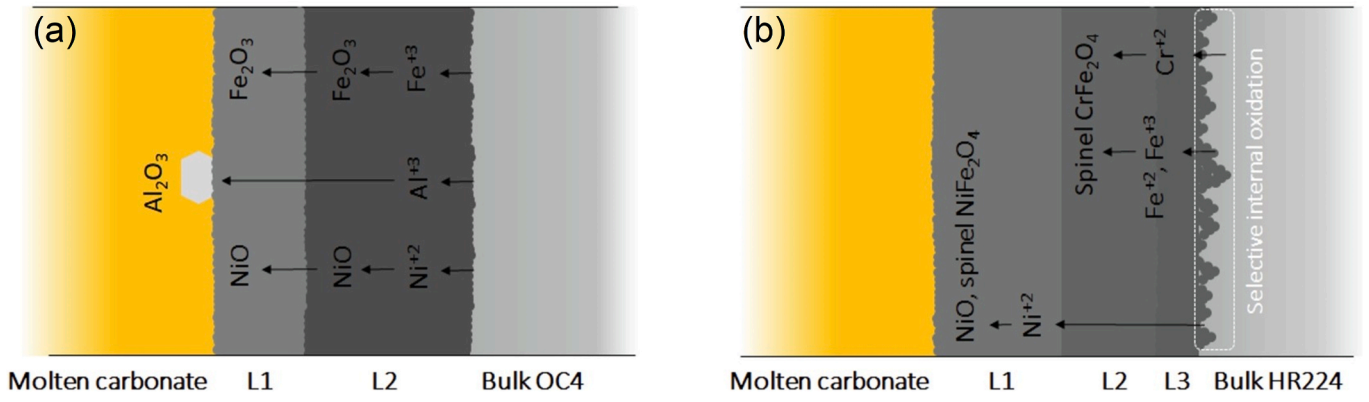

Fig. 21. Proposed concept involved in growth of protective multilayer on AFA alloys exposed to molten carbonate: (a) OC4 and (b) HR224 (reproduced with permission from Ref. [89]).

strengthened (ODS) FeAl alloy was investigated in molten Li_2CO_3–K_2CO_3 eutectic at 650 °C under flowing CO_2–O_2 gas mixtures [98]. At low CO_2 partial pressure conditions, both the alloys followed a time-decreasing corrosion rate due to the formation of protective oxide scales, with the corrosion resistance of FeAl being much higher than that of SS316L. In dry CO_2 gas, corrosion of AISI 316 proceeded at a near-linear rate, indicative of a surface-controlled reaction. ODS-FeAl corroded initially following a parabolic behavior, but exhibited some weight loss on further reaction. In a $67CO_2$–$33O_2$ gas mixture, both alloys experienced weight loss. The weight loss of AISI 316L can be attributed to the high oxidizing power of the gas causing a continuous dissolution of the Cr_2O_3 layer into soluble chromate. A totally different mechanism was observed for ODS-FeAl, where corrosion is caused by a high CO_2 partial pressure, resulting in the acidic fluxing of yttria particles from oxide dispersion.

Biedenkopf et al. [99] studied corrosion behavior of iron and chromium in $0.62Li_2CO_3$-$0.38K_2CO_3$ molten salt and found that the corrosion products were arranged in a multilayer structure, with $LiFeO_2$ and $LiCrO_2$ being the primary products in different layers. The data collected from various studies on corrosion of structural materials in the carbonate-based molten salts are shown in Tables 5 and 9 and the corrosion rate of structural materials in carbonate-based molten salts at different temperatures is shown in Fig. 23. The figure shows that Ni-based alloys (In625) exhibited the lowest corrosion rate and are suitable for next-generation CSP applications.

3.5. Fluoride salts

Fluoride-based molten salts have been used as primary and secondary coolants in nuclear energy systems [100,101]. In nuclear power plants, fluoride salts can be used as potential transport fluids in a heat exchange loop because of its superior characteristics: large specific heat and high thermal conductivity, high density at low pressures, resistance to radiolysis, and relatively good chemical inertness [102]. However, the corrosion of containment materials by fluoride molten salts and the factors influencing them are similar for both CSP and molten salt reactors. Extensive research has been conducted on fluoride-based molten salt properties and corrosion of structural materials, mainly Ni-based alloys, at very high temperatures of 700–900 °C [103,104]. Oak Ridge National Laboratory (ORNL) investigated various causes for corrosion and developed its mitigation techniques during 1947–1970 [105,106]. It was found that the main reasons for corrosion in molten salts are the

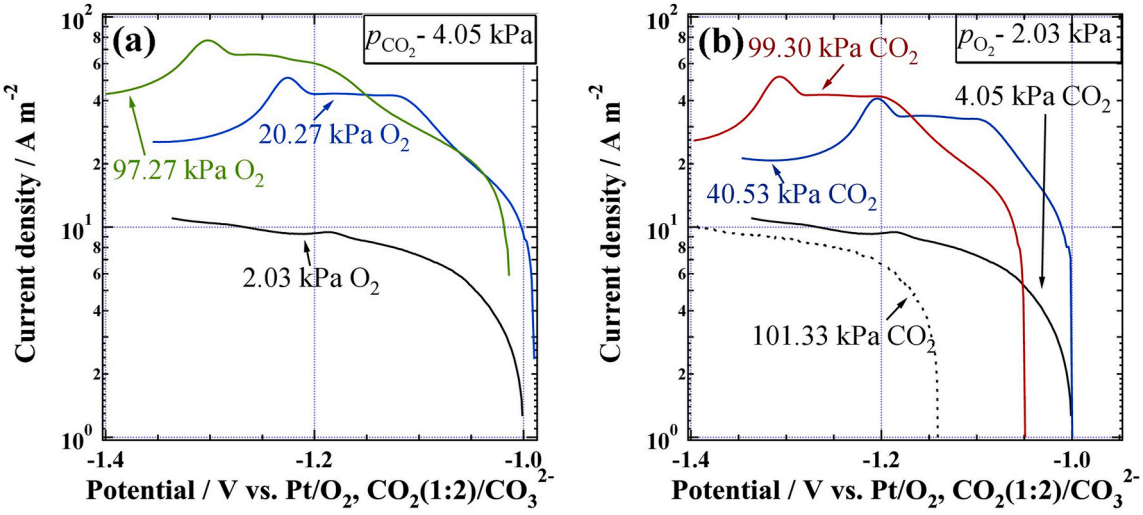

Fig. 22. Cathodic polarization curves of 304 stainless steel observed in 0.43Li_2CO_3-0.32Na_2CO_3-0.25K_2CO_3 at 650 °C and under mixed gases of (a) 4.05 kPa CO_2 and (b) 2.03 kPa O_2 (reproduced with permission from Ref. [92]).

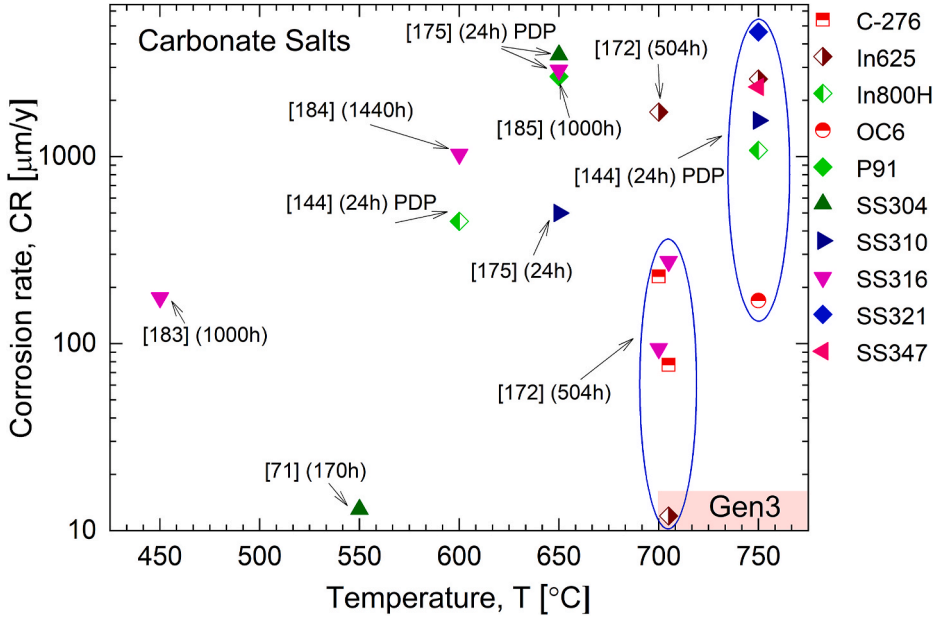

Fig. 23. Corrosion rate of different structural materials in terms of temperature for corrosion in carbonate salts.

differences in free energy of the fluoride salt constituents and their alloying elements, impurities present in the salt, difference between hot and cold section temperatures, and presence of dissimilar materials at vicinity of each other in molten salts [55].

The corrosion mechanism of Ni–Mo–Cr alloys (HASTELLOY-N, GH3535, and MoNiCr) was investigated in FLiNaK molten salt at 650 °C [104]. It was observed that the corrosion of these alloys differs not only on their elemental composition but also on their microstructural properties such as grain size, length of grain boundary and presence of phase of the particles. Using electron back-scatter diffraction technique, it was found that primary M_6C carbides of up to 5 μm in size were present in both HASTELLOY-N (~0.75%) and GH3535 (~1.25%) whereas MoNiCr alloy has no such large M_6C carbides (>1 μm). However, MoNiCr has a larger grain size compared to HASTELLOY-N and GH3535 alloys. The study concluded that MoNiCr alloy being affected marginally in the FLiNaK molten salt exposure could be due to its chemical composition, large grain size, and virtual absence of large (M_6C) carbides.

Wang et al. [107] investigated the corrosion of pure Cr and alloy of GH3535 in FLiNaK molten salt over a temperature range of 650–700 °C and 600–700 °C for 24 h. From electrochemical analysis, they found that the corrosion potentials shifted negatively, and current densities increased with increase of molten salt temperature from 600 °C to 700 °C. Also, galvanic corrosion increased in both Cr and GH3535 when the two substrates are in electrical contact in molten salt where temperature gradients exist. The mass loss for Cr anode was found to be 141 mg/cm^2 at temperature gradient of 50 °C and increased to 162 mg/cm^2 when the temperature gradient increase to 100 °C. In the case of GH3535, mass loss of 2.89 and 2.17 mg/cm^2 were measured at the temperature gradients of 600–700 °C and 650–700 °C, respectively.

The data collected from various literature on corrosion of structural materials in fluoride-based molten salts at different temperatures is shown in Fig. 24. From the figure, it is observed that all the structural materials exhibit a high corrosion rate in fluoride salts.

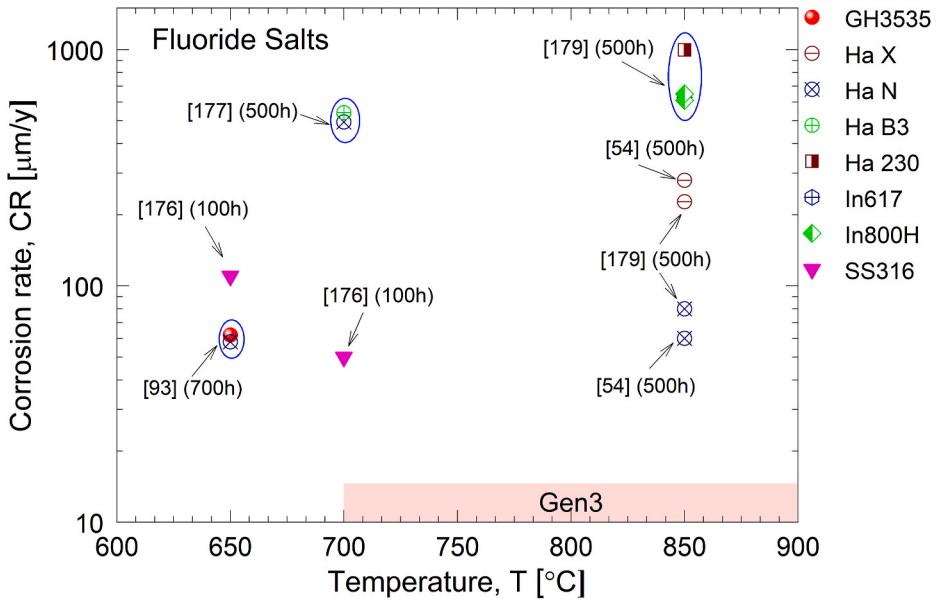

Fig. 24. Corrosion rate of different structural materials in terms of temperature for corrosion in fluoride salts.

3.6. Liquid metals

Molten salts are not chemically stable at higher temperatures, particularly on the hot side of a turbine engine operating at inlet temperature > 1300 °C, as in air-Brayton thermodynamic cycles. In these applications, the fluid should be chemically stable and compatible with structural materials at extreme environments. Liquid metals are one potential class of fluids for such applications. Recently, the importance of liquid metals for use as heat transfer fluids has been reviewed for nuclear and CSP systems [108,109]. Currently, liquid metals have received more attention for solar thermal systems since they have several advantages over molten salts, including high operating temperature, low viscosity, and effective heat transfer characteristics.

High-temperature materials like silicon carbide (SiC), graphite (C), and mullite ($Al_6Si_2O_{13}$) were examined in the liquid Sn. Corrosion and its penetration on these materials in pure and 2 wt% Zn doped Sn liquids were evaluated at 1350 °C for 100 h [110] using electron microscopic analyses and weight change measurements. Cross-sectional SEM images of the molten liquid Sn exposed graphite tube surfaces after ion milling are shown in Fig. 25. Bright spherical particles of solidified tin-bearing phase were detected on the surface of the graphite tubes. The presence of spherical particles at external graphite surfaces with purity of 98% (Figs. 25(a))–99.999% (Fig. 25(b)) indicates that the Sn-based liquids did not penetrate the graphite tubes at the temperature of 1350 °C. The penetration of Sn-based liquids on the graphite tubes at 1350 °C was also determined by measuring the weights of Sn-based composition. The loss of graphite in each tube was obtained by dividing the measured weight loss of the graphite tube by the starting bulk density of the tube. The graphite recession values were extracted by dividing the lost graphite volume with the exposed graphite surface area.

The recession values of the graphite are plotted in Fig. 25(c). Recession values ≤ 0.43 µm were observed on graphite tubes with very little mass loss per area (≤ 7.5×10^{-5} g/cm^2). No appreciable changes were detected with respect to Sn purity. But in the case of α-SiC, significant mass loss per area (3.8×10^{-3} g/cm^2) was observed when exposed to 99.8% purity of molten Sn. However, mass loss of SiC reduced to ≤ 4.2×10^{-5} g/cm^2 by addition of 0.06–0.12 wt% soluble silicon to molten Sn at 1350 °C due to incongruent dissolution of α-SiC. There was no appreciable change observed in mullite when it contacts with Sn but partial silica reduction (alumina enrichment) was detected with graphite at 1350 °C. Such silica reduction can be avoided by

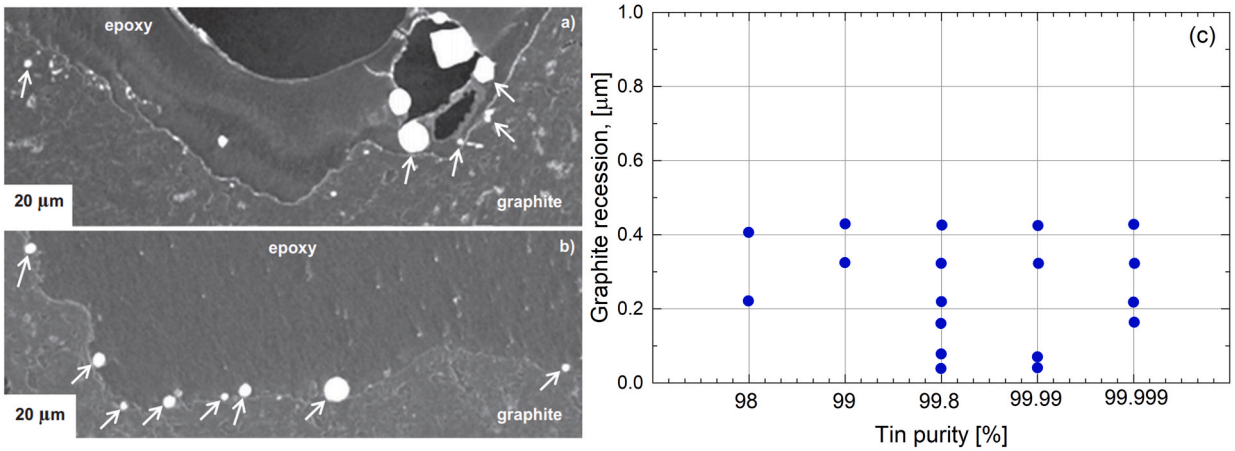

Fig. 25. Cross-sectional SEM images of graphite surfaces exposed at 1350 °C for 100 h (a) 98 wt% molten Sn, (b) 99.999 wt% molten Sn and (c) graphite recession after exposure to molten Sn at 1350 °C for 100 h with different purities (reproduced with permission from Ref. [110]).

physical separation of mullite from graphite. From this study it can be concluded that graphite, SiC, and $Al_6Si_2O_{13}$ are useful containment materials in CSP systems which are compatible with liquid metals operating at higher temperatures.

Sodium is the most technologically ready of the main liquid metal candidates as there is extensive experience with materials compatibility [111]. Although sodium is a hazardous material, CSP can benefit from the depth of experience gained by the nuclear industry working with high-temperature liquid sodium. The key benefits are that it is a liquid within a suitable temperature range for advanced power cycles and that its high conductivity may lead to better system performance, potentially upward of 15% higher than current state-of-the-art molten salt systems. Sodium seems to be an unlikely candidate for high-temperature applications due to its boiling point being slightly above 800 °C at 1 atm pressure. Such a relatively low boiling point can lead to a significantly more dangerous operation if sodium vapor is released at high temperatures since it will burn upon contact with moisture from the air. For these reasons, only liquid heavy metals remain as reasonable candidates for high-temperature applications.

Lead-bismuth eutectic (LBE: 55.5 w.t.% Bi, 45.5 w.t.% Pb) can be used as a potential candidate as HTF due to its special benefit of the large temperature difference between its high boiling point (1670 °C) and the rather low melting point (125 °C) [112]. The other benefits are non-reactivity with water and low vapor pressure. Lead and bismuth are less chemically active than the main constituents of steel and other common structural materials and have high Gibbs free energy so that oxides of the constituent elements of structural materials will form preferentially than the formation of PbO or Bi_2O_3. The oxides of constituent elements can act as passive layers to protect and prevent the further diffusion of constituent elements of the alloys when in contact with LBE.

3.7. Supercritical CO_2

Currently, all solar thermal power plants are based on converting solar thermal energy to electricity through traditional Rankine steam cycles. High temperature operating power block configurations are needed to enhance the efficiency power conversion, as the steam cycle maximum temperature is limited to 550 °C. Supercritical CO_2 (sCO_2) Brayton cycles, which can operate at high temperatures $>$ 600 °C, are identified as the future power block to convert thermal to electric energy [113,114]. Initially, supercritical CO_2 cycles were proposed in the late 1960s [115] to overcome the limitations of steam cycle performance. Traditionally these cycles are considered in application of nuclear power plants [116], but the development of supercritical CO_2 power conversion technology has been reinvigorated by the pusuit of cost-effective CSP technology [117]. In light of this, the corrosion characteristics of different structural materials in supercritical CO_2 conditions at medium and high temperatures is reviewed below.

Corrosion behavior of austenitic alloys of SS316 and SS310 and Incoloy 800H (In800H) were examined in supercritical CO_2 conditions maintained at 650 °C and 20 MPa for 3000 h [118]. It is reported that Incoloy 800H showed the lowest weight gain and exhibited the best corrosion resistance among all alloys studied. In800H and SS310 were oxidized and the corrosion followed a diffusion-controlled parabolic growth law. Spallation of oxide layer was particularly observed in SS316, but it was less significant for SS310 and In800H. In SS310, Cr-rich oxides of Cr_2O_3 and $Cr_{1.4}Fe_{0.7}O_3$ act as protective layers to improve the corrosion resistance. In Incoloy 800H, a very thin layers of chromium-rich oxides, magnetite and a spinels of $Ni_{1.4}Fe_{1.7}O_4$ and $MnFe_2O_4$ are responsible for the higher corrosion resistance.

Corrosion behavior of special metals like stainless steel AL-6XN and three nickel-based alloys of PE-16, Haynes 230, and Inconel 625 were investigated in sCO_2 conditions maintained at 650 °C and 20 MPa up to 3000 h exposure [119]. After exposure, the weight gain in the alloys was found to be 0.23, 0.13, 0.17 and 0.15 gr/cm^2 for Al-6XN, Haynes 230, Inconel 625, and PE-16, respectively. Results showed that the Al-6XN exhibited the least corrosion resistance compared to other alloys. Oxide layers composed of Fe_3O_4 as the outer layer and $FeCr_2O_4$ as the inner layer formed on the surface and Cr-rich oxide phases of Cr_2O_3 and $Cr_{1.4}Fe_{0.7}O_3$ were identified as the protective layers. In the case of alloy PE-16, formed thin layer of Al_2O_3 and Cr_2O_3 in Haynes 230 and 625 were identified as the primary protective oxide layer.

He et al. [120] studied corrosion of alumina forming austenitic steel in sCO_2 over a temperature range 450–650 °C and at 20 MPa for 1000 h exposure. The weight gain and scale thickness increase rapidly as the temperature increases. It is reported that at low temperatures or short exposure times, a thin and continuous layer composed of Al_2O_3 and $(Cr, Mn)_3O_4$ was detected which acted as protective layer. Continuity in the Al_2O_3 scale is lost as the temperature and exposure time increase and a non-protective multilayer structure composed of Fe_3O_4, $FeCr_2O_4/Al_2O_3$, $NiFe/FeCr_2O_4/Cr_2O_3/Al_2O_3$, $(Cr,Fe)_3O_4$, $NiFe/Cr_2O_3/Al_2O_3$ was detected. It is found that the breakaway oxidation mechanism is related to the depletion of Al and Cr from their respective oxides. The corrosion rate of different alloy materials in sCO_2 at different atmospheric conditions and different temperatures is shown in Table 10.

4. Corrosion mitigation

High-temperature corrosion is a significant issue in materials selection, structure design, and lifetime prediction of CSP plants. While the mechanisms of corrosion associated with the different heat transfer fluids were reviewed in Section 3, this section is devoted to the studies on mitigation of high-temperature corrosion in structural materials, which plays a crucial role in the reliability, quality, safety, and cost-effectiveness of CSP systems. Various methods can reduce corrosion through molten salt modifications like the addition of nanoparticles, control of redox potential, and removal of impurities present in the molten salts. Besides, oxide and amorphous metal coatings on the structural materials inhibit corrosion. Different corrosion mitigation techniques have been used so far, as discussed in the following subsections.

4.1. Corrosion control with nanoadditives

Corrosion studies of commercial stainless steel SS347 were conducted in two different grades of solar salt (industrial (ISS) and refined purity (RSS)) doped with 1 wt% Al_2O_3 nanoparticles or 1 wt% SiO_2 nanoparticles [89]. Results showed that the steel showed a higher corrosion rate in the ISS mixture due to the presence of higher Cl content. Also, it has been found that Al_2O_3 nanoparticles provides better corrosion protection to the steel matrix in RSS salts rather than using ISS salts. The formed alumina needles and a compact protective layer of spinel ($FeCr_2O_4$) on the steel surface enhance the corrosion resistance of the steel when contact with the molten salt at 565 °C.

Nithiyanantham et al. [121] investigated the influence of nanoparticles of Al_2O_3 and SiO_2 dispersed in binary eutectic (51% $NaNO_3$–49%KNO_3) nitrate salt on the corrosion of carbon steel A516 Gr70. The corrosion tests were conducted under static immersion conditions in the presence of air at 390 °C and different exposure times. The observed mass change in the carbon steel after corrosion tests in pure eutectic salt, and Al_2O_3, and SiO_2 doped nanofluids at 390 °C is shown in Fig. 26. In the figure, it can be seen that initially higher mass gain is observed in all the salts up to 250h, which then decreases at 500 h, after which it followed a linear variation with exposure time. However, the mass gain was higher in pure eutectic salt than Al_2O_3 and SiO_2 doped nanofluids, which supports the occurrence of higher oxidation in the eutectic salt. The mass gain in SS347 is ~2.2 mg/cm^2 in pure eutectic salt which decreased to ~0.7 mg/cm^2 in Al_2O_3 based nanofluids and further decreased to 0.6 mg/cm^2 in SiO_2 based nanofluids after exposure to 1500 h. It was also reported that the maximum penetration depth of the corrosion layer decreased by addition of nanoparticles to the eutectic

Table 10
Corrosion rate of structural materials in supercritical CO_2 at various temperatures and in different environments..

Reference	Material	Temperature[°C]	Pressure[MPa]	Environment	Time [h]	$\Delta m/S_o$ [mg/cm^2]
[201]	P91	245	8	CO_2 rich phase	500	0.26
	SS347					0.05
	P91	245	8	With H_2O condensation	500	0.22
	SS347					0.001
[202]	Alloy 600	550	20	sCO_2	1000	0.021
	Alloy 690					0.020
	Alloy 800HT					0.020
	Alloy 600	600	20	sCO_2	1000	0.055
	Alloy 690					0.09
	Alloy 800HT					0.065
[203]	304H	600	150 cc/min	Industrial grade CO_2	1000	0.105
	347H					0.035
	800H					0.065
	HR120					0.06
	In617					0.07
[202]	Alloy 600	650	20	sCO_2	1000	0.07
	Alloy 690					0.12
	Alloy 800HT					0.08
[118]	SS316	650	20	sCO_2 Phase	1000	1.0
	SS310					0.02
	Alloy 800H					0.01
[204]	SS347	650	20	RG CO_2	1000	0.03
	AFA OC6					0.4
[205]	T91	650	15	sCO_2 Phase	500	0.051
	TP347HFG					0.002
	Alloy 617					0.002
[206]	Haynes 230	750	20	RG CO_2	1000	0.1
	Haynes 625					0.15
[207]	740H	750	20	RG CO_2	1000	0.0021
	In625					0.0043
[207]	S30409	800		25 bar CO_2	500	0.18
	N06230					0.25
	N07208					0.42
	N07247					0.3
	S30409	800		25 bar (CO_2+H_2O)	500	0.36
	N06230					0.59
	N07208					0.46
	N07247					0.22
	S30409	800		25 bar(CO_2+H_2O + SO_2)	500	2.5
	N06230					0.16
	N07208					0.67
	N07247					0.30

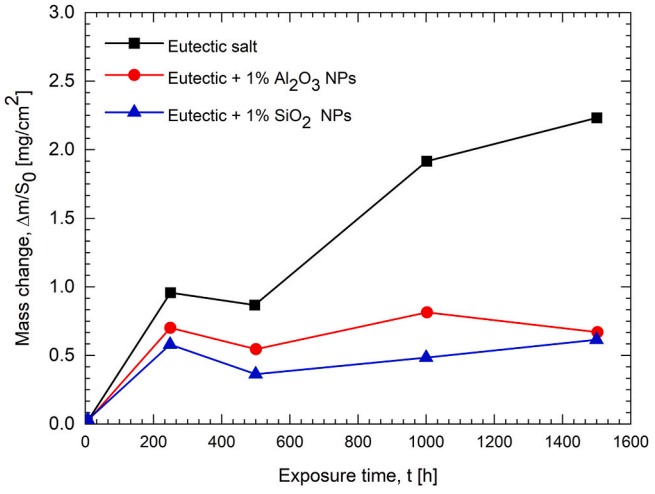

Fig. 26. Mass change in carbon steel following corrosion in eutectic salt, Al_2O_3 and SiO_2 based nanofluids at 390 °C (reproduced with permission from Ref. [121]).

salts (~21 μm for pure salt; ~8 μm for Al_2O_3 nanofluid; and ~9 μm for SiO_2 nanofluid). The diminished penetration depth and minimal corrosivity in nanofluids may also be due to the incorporation of nanoparticles into the corrosion layer.

In another study, the same research group [122] reported an increased corrosion rate with nanoparticles in HitecXL salts. They reported two major factors that affect the corrosion of carbon steel when molten salt mixed with nanoparticles. One factor is incorporation of nanoparticles into the corrosion layer and other is formation of long-lasting microbubbles in the salt (~4 days at 310 °C) both leading to increase in the oxidation rates. In contrast, other studies reported a reduction in corrosivity in binary carbonate salt incorporating 1 wt% silica nanoparticles at 520 °C [123]. However, a few drawbacks were observed when the salts were doped with SiO_2 nanoparticles including increase of the molten salt viscosity during the test. Nithiyanantham et al. [124] studied the influence of the size of the nanoparticles to that of the base salt. A higher viscosity was observed for 17 nm size of SiO_2 covered with 5 nm outer diameter of Al_2O_3 core shell-based nanofluids due to chain-like aggregation, which was 25–34% higher compared to the base fluids in the temperature range between 250 and 400 °C.

4.2. Salt purification and redox potential control

Impurities present in the molten salts severely affect the corrosion of structural materials. In the case of solar salt, even low concentration of Cl and oxide ions causes severe corrosion in structural alloys at high

temperatures [63,125]. Bradshaw and Goods [126] investigated the effects of thermal cycling and chloride concentration on corrosion of Fe-based alloys in nitrate salts. The results showed a corrosion rate increase of 25–50% in 316 SS, 25% in 316L SS, and 50% in 304 SS when the chloride concentration was up to 0.82%. The increase could be due to cracking of protective oxides due to stresses developed by differences in the thermal expansion between the metal and corrosion products. The authors studied the effect of impurities and humidity on corrosion and compatibility of carbon steel (A516.Gr70), SS304 and SS316 in molten HitecXL salt at 310 °C. They observed that the humidity present in the salt severely affects the corrosion rate in the case of carbon steel A516. Gr70 and making it an unacceptable choice under such conditions. But acceptable corrosion rates were observed in SS304 and SS316 [127].

In chloride based salts, moisture and oxygen contaminants are the main impurities which can react with the chlorine anion to form HCl and Cl_2, that leads to high corrosion rates [128,129]. Salt purification is one of the methods to significantly reduce the corrosive impurities thereby improving corrosion resistance of structural materials especially for chloride molten salts [55,72]. Multiple methods of controlling salt dehydration and purification have been proposed to mitigate the corrosion risks, such as controlled thermal treatment [130,131], magnesiothermic reduction by adding elemental Mg [132,133], dehydration with NH_4Cl [134], and carbochlorination with CO, Cl_2, and/or CCl_4 [135]. Carbochlorination is a general method for extracting oxide impurities present in metals. Various forms of carbochlorination like carbon with chlorine ($C + Cl_2$), carbon monoxide with chlorine ($CO + Cl_2$) are widely used combinations [136]. Chen et al. [135] used carbon tetrachloride (CCl_4) to extract trace oxide from haloaluminate melts as phosgene. Mathew et al. [137] purified a 1 kg of 68:32 mol% KCl:$MgCl_2$ salt by sparging with CCl_4, which reduces the dissolved oxide to trace levels (42 mmol MgO/kg salt). It was also found that CCl_4 exhibited superior purification thermodynamics in $MgCl_2$-based salt compositions above the melting temperature.

Most alkali chlorides may be heated under pressure to absorb surface moisture and then melted to extract dissolved moisture. But heating in vacuum creates impurity of $MgCl_2$ due to hydrolysis and then double vacuum distillation yields high purity salt by leaving low vapor pressure impurities, such as MgO [138]. Although distillation produces high salt purity, this poses a technological problem that raises costs and limits economic feasibility. Currently, reagents such as NH_4Cl or HCl are used to purify $MgCl_2$-based materials in magnesium production by the electrolysis process [139]. Noah et al. [140] demonstrated an easy-to-use method to determine MgOHCl and MgO in $MgCl_2$-containing chloride salts. They extracted the impurities using methanol followed by water, and then by a common EDTA titration procedure, that shows significant improvement over the other reported methods. The tests demonstrated that the procedure is appropriate in mass fraction regimens as small as 1.0 wt % MgO and 0.3 wt % MgOHCl. Further, It can be enhanced by adjusting the concentration of the EDTA solution.

Gong et al. [141] proposed a chemical analysis technique based on direct titration and a high-precision automatic titrator used in the exact measurement of MgOHCl at the tens of ppm O level. The method showed a standard deviation below 5 ppm O and an average error below 7 ppm O when the concentration of MgOHCl is 36 ppm O. Moreover, compared to other methods available in some literature reports, the titration method can exclude the influence of co-existing MgO on the MgOHCl concentration measurement. This chemical analysis technique was used to calibrate the previously developed electrochemical method based on cyclic voltammetry (CV) to achieve reliable in situ monitoring of MgOHCl in the $MgCl_2$–KCl–NaCl molten salt at a concentration as low as the tens of ppm O level. The in-situ monitoring technique showed a monitoring limitation of < 39 ppm O.

Fernandez et al. [142] addressed the corrosion mitigation strategy by various thermal treatments before reaching the testing temperature of 720 °C. They found that the corrosion rate was decreased from 19.66 mm/year to 6.33 mm/year after thermal treatment. The lowest corrosion rate was obtained for a specific stepwise heating (117 °C for 2 h, 145 °C for 4 h, 190 °C for 4 h, 227 °C for 4 h, 300 °C for 4 h, 450 °C for 3 h and 600 °C for 1 h). It is also reported that without purification, MgOHCl is the main aggressive impurity in chloride based molten salts.

Recently, the U.S. Department of Energy's Oak Ridge National Laboratory provided a unified procedure and a protocol for handling and purifying anhydrous carnallite (AC) salt [143]. In their process, as-received AC salt with grains of > 2 mm, 2.5 g of Mg and 65 g of SPK halite for each 1 kg of AC salt were placed in a quartz crucible, which was, in turn, placed in a purification vessel with a gas inlet and a gas outlet. Before starting the purification procedure, the vessel was drawn to a vacuum of < -25 inHg (-0.085 MPa) and flushed with UHP or higher grade nitrogen (or Ar) at least three times. The vessel was kept in the furnace and heated to 120 °C for 2 h with a ramp rate of 1 °C/m and then raised the temperature to 670 °C with the same ramp rate and maintained up to 3 h. For a larger scale, the hold time needed may vary and it can be determined by monitoring the release of HCl. The flow of cover gas was kept at a constant rate during the entire purification process. A high flow rate is used to remove HCl and water generated during purification as fast as possible to avoid corrosion at the gas outlet. After the furnace is cooled down to room temperature, the test vessel was opened and the quartz crucible/salt was transferred into an inert glove box. Using the purified salt with varying Mg concentration, the corrosion rate of alloy 600, alloy 230 and C276 was reduced to the target goal of < 15 μm/y when tested at 600–800 °C, for up to 1000 h.

Redox control is another technique that has been proposed to protect the containment materials from corrosion in molten fluoride and chloride salts [144]. The idea of the redox control is to introduce another redox couple RA^{k+}/RA^{j+} ($k > j$, RA stands for a redox buffering agent), to make the salt less oxidizing. Three major approaches for redox control are through gas-phase control, major metal control, and dissolved salt control [145]. Every technique introduces a reducing agent into the system to establish equilibrium within the molten salt. The redox potential is a broadly used term in molten salt electrochemistry to describe the redox condition of molten salt. The term is defined as the tendency of a chemical species to acquire electrons and become reduced. It is a measurable voltage that is related to the activities of the reduced and oxidized species in the molten salt solution (i.e. concentration).

Fig. 27 shows the kinetics of reactions occurring on a corroded metal surface in a redox control system that contains a metal M, an oxidizing impurity Ox, and a redox buffering agent RA^{k+}/RA^{j+}. All electrochemical parameters except the exchange current density of RA^{k+}/RA^{j+} are the same in Fig. 27(a) and (b). The horizontal line indicates the corrosion potential where the net current is zero. It is seen that the inhibition of corrosion by introducing RA^{k+}/RA^{j+} with lower i_0 in the system is minimal. By increasing the i_0 of RA^{k+}/RA^{j+} (Fig. 27(b)), the negative shift of corrosion potential becomes more pronounced. At this corrosion potential, the oxidation rate of RA^{j+} is several orders of magnitude higher than the dissolution rate of metal M. This means most oxidants will be consumed by the oxidation of RA^{j+} rather than metal corrosion. In other words, RA^{j+} acts as a sacrificial material to protect the metal. In addition to the exchange current density, the charge-transfer coefficient and diffusion coefficient also affect the sacrificial effect of redox buffers.

From a thermodynamic consideration, the redox potential of RA^{k+}/RA^{j+} should be controlled below the oxidation potential of M to avoid corrosion by RA^{k+} following the consumption of oxidizing impurities. Therefore, the redox control system requires a redox buffer RA^{k+}/RA^{j+} with higher i_0 and lower redox potential. The redox potential can be controlled by adjusting the concentration ratio of RA^{k+}/RA^{j+}, which may change with time due to the reaction with oxidants in the molten salt.

Addition of a corrosion inhibitor is also an effective way to further reduce corrosion by lowering the redox potential of a salt [146]. In this process, the added inhibitors favourably react with the corrosive impurities present in the salt and devour them. The use of corrosion

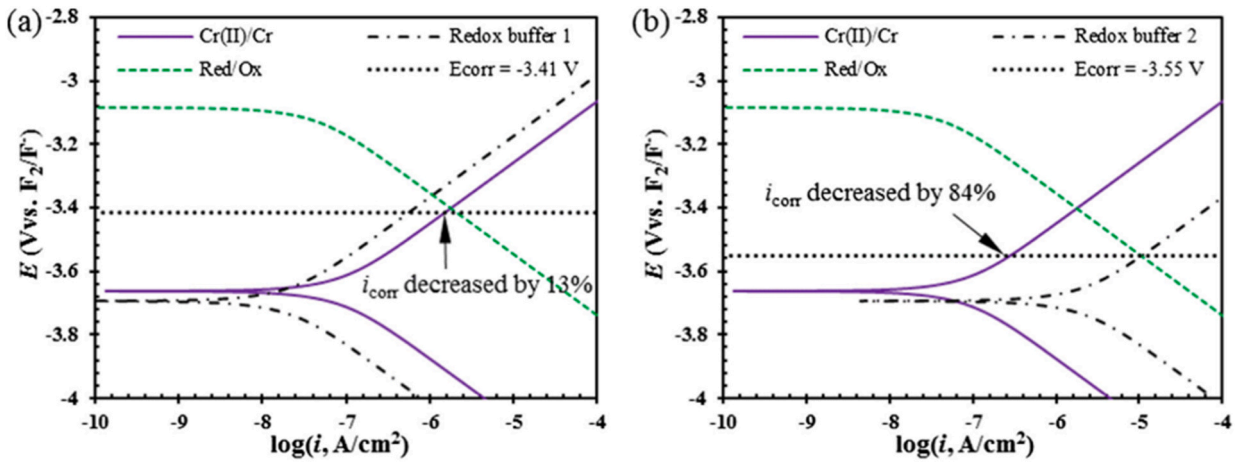

Fig. 27. Schematic polarization curves for chromium corrosion in the presence of a redox buffer with (a) low i_0 and (b) high i_0, respectively. (reproduced with permission from Ref. [144]).

inhibitors in different aggressive environments have been reported in the literature such as, for example, Li metal addition in molten LiCl [147, 148], Mg in molten $MgCl_2$–KCl [132]. The results showed that corrosion rate was reduced to be 35 times lower than baseline tests, with addition of 1.15 mol% Mg in $MgCl_2$–KCl under an inert atmosphere at 850 °C. Ding et al. [149] investigated the corrosion of commercially available

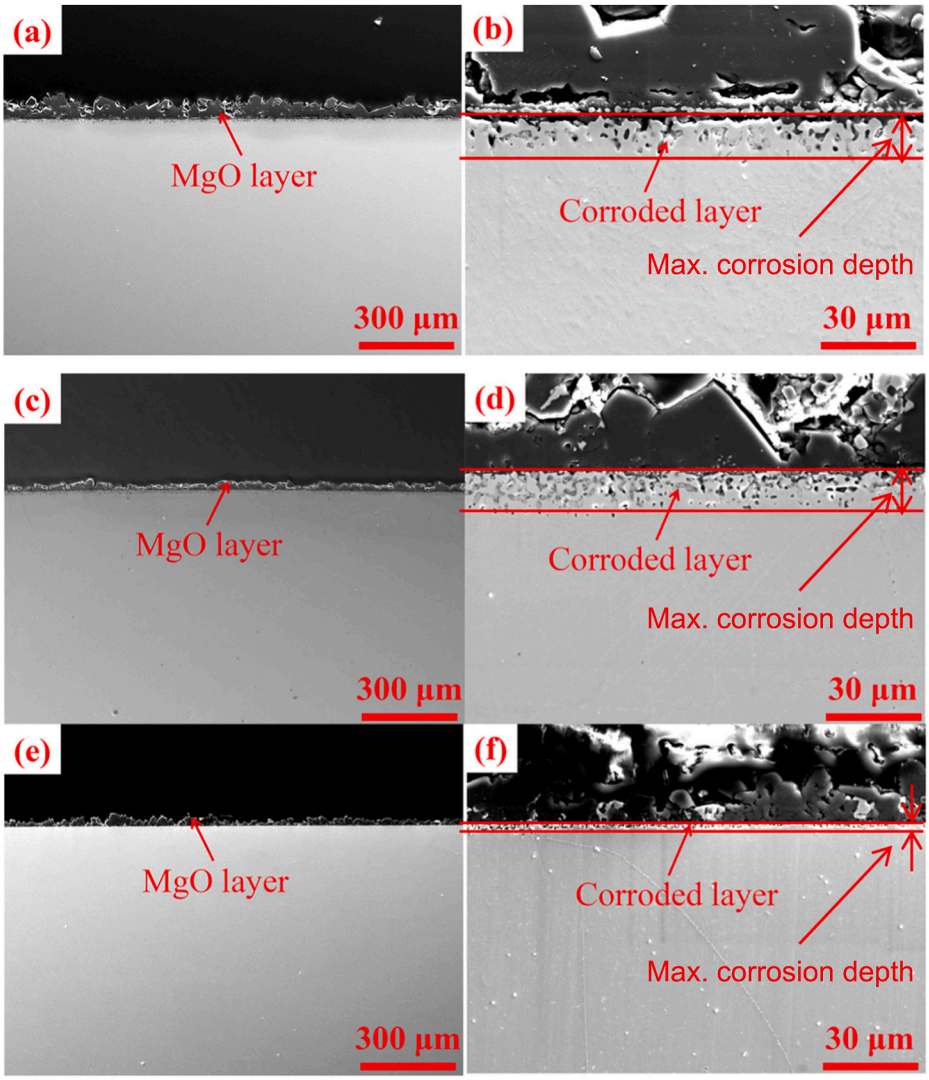

Fig. 28. Cross-sectional SEM images (BSE) of: (a and b) SS310, (c and d) In800H and (e and f) Ha C-276 following corrosion experiment with addition of 1 wt% Mg (a, c, e: 100 ×; b, d, f: 1000 ×) (reproduced with permission from Ref. [149]).

Fe–Cr–Ni alloys (SS310, Incoloy 800H, and Hastelloy C-276) in molten $MgCl_2$/NaCl/KCl (60/20/20 mol%) mixed salt with addition of 1 wt% Mg as a corrosion inhibitor at temperature of 700 °C under inert atmosphere for 500 h.

Cross-sectional SEM backscattered electron (BSE) images of the three tested alloys (SS316, In800H and C-276) are shown in Fig. 28 (a, c, and e are low-magnification images; b, d, and f are at higher magnification). It is observed in the figure that a measurable and dense MgO layer with a thickness of 30 ± 15 μm is attached to all samples (Fig. 28(b, d), and f with 1000X). Beneath the MgO layer, a porous and uniform corroded layer is observed with the same thickness in SS310 and In800H, while a thin corrosion layer is detected on the Ha C-276 surface. The maximum corrosion depth of SS 310, In800H and Ha C-276 were measured to be 100, 50, and 30 μm, respectively, after immersion for 500 h at 700 °C. After adding Mg, the corrosion depths reduced to 17 ± 4, 15 ± 3, and 1.7 ± 0.5 μm, respectively. The same research group [150] used an electrolysis method to purify the molten chloride salts with an Mg-anode to reduce the corrosive impurity $MgOH^+$ concentration. Cyclic voltammetry measurements showed that the potential of the alloy shifts to more negative values, which indicates that the salt is less oxidative. The impurity concentration in purified salt was only ~7% of that in un-purified salt at 500 °C. Potentiodynamic polarization results revealed that the corrosion rate of In800H in purified salt is ~20% of that in un-purified salt at 700 °C.

However, excess Mg can form intermetallic compounds with nickel at high temperatures, which may cause alloy embrittlement. Hanson et al. [151] studied a combination of corrosion experiments, microscopy, and modelling to investigate the interaction of Ni-200 (99.6% Ni) and austenitic stainless steel 316 H with KCl + $MgCl_2$ salts, with and without the addition of different amounts of pure Mg. *Ab initio* molecular dynamics simulations were used to predict the influence of residual H_2O impurity in the chloride salt. Experimental results revealed that the added excess Mg reacts with impurities to mitigate corrosion completely before it starts developing intermetallic compound with Ni. In the case of 316 H, the results showed that optimization of Mg level depends on the impurity amount, which will reduce the molten salt and prevent the selective dissolution of Cr or other active elements. But no form of Ni–Mg intermetallic was detected on Ni-rich (N-200) alloy surfaces.

4.3. Oxide and metal coatings

Corrosion-resistant coatings on structural materials are possible solutions to reduce corrosion at high temperatures. Environmentally compatible coatings at high temperatures are regularly used on turbine blades in jet propulsion and power generation applications [152–154]. Similarly, coatings on structural materials in contact with molten salts can improve the lifetime of CSP plants which operate at high temperatures. Corrosion resistance of P91 steel, dip-coated with a sol-gel ZrO_2–3% mol Y_2O_3, was statically tested at 500 °C in contact with solar salt for 1000 h [155] and the results were compared with SS304 steel from a technical and environmental point of view. The coating thickness was found to be 1.0–1.4 μm, with the elemental composition of 1.68% of Zr and 1.01% of Y. After 1000 h of testing, the uncoated P91 showed a weight loss of 0.320 mg/cm^2 and the coated P91 suffered a weight loss of 0.050 mg/cm^2, comparable to the uncoated SS304 (0.043 mg/cm^2). The results suggest that the coating significantly protects P91 steel against corrosion in the molten binary salt. Nithiyanantham and co-workers [156,157] reported that graphite coating could serve as suitable anti-corrosion protection for carbon steel against molten solar salt and HitecXL salt. They reported that the corrosion rate decreased by more than a factor of 6 compared to the non-graphitized carbon steel by adding 2 wt% of graphite into the solar salt. This reduction in corrosion rate is due to the formation of homogeneously dispersed iron carbide crystals on the surface of carbon steel [158].

Thermal spraying using high velocity oxy fuel (HVOF) process has been of emerging interest in depositing protective overlay coatings onto the surfaces of structural materials to allow them to operate under extreme circumstances [159]. Generally, HVOF process involves the transfer of thermal and kinetic energy by means of acceleration of molten powder particles to deposit the desired coating [160]. HVOF sprayed coatings are a viable option to protect superalloys from hot corrosion. Corrosion evaluations of uncoated and coated In800H and stainless steel SS310 alloys were conducted in 34.42 wt% NaCl – 55.47 wt% KCl at 700 °C in the presence of N_2 atmosphere [161]. Coatings of MCrAlX where M = Ni, Co and X = Y, Ta, Hf, and/or Si were deposited on alloy materials using HVOF and subsequently the coated samples were annealed at different temperatures of 700–900 °C in the presence of air. NiCoCrAlY coatings were reported to show the lowest corrosion rate of 190 μm/y after annealing in air at 900 °C for 24 h with a heating/cooling rate of 0.5 °C/min.

Gomez et al. [162] studied the corrosion performance of Ni-based MCrAlX coatings on common alloys of SS310 and In800H in molten carbonates (Na_2CO_3–K_2CO_3–Li_2CO_3) in the presence of bone-dry CO_2 atmosphere at 700 °C. Their results reported that coatings after oxidation reduced the corrosion rates by two orders of magnitude from ~2500 μm/y to only a few tens of μm/y. The coating 47.6Ni/22Co/17Cr/12Al/0.5Hf/0.4Si/0.5Y (by wt%) deposited using atmospheric plasma spray and annealed in air at 900 °C for 24 h in steps of 0.5 °C/min showed a corrosion rate of 34 μm/y. In comparison, the coating with composition 38.5Co/32Ni/21Cr/8Al/0.5Y (by wt%) deposited using HVOF and annealed in air at 800 °C for 24 h in steps of 0.5 °C/min showed a corrosion rate of 46 μm/y.

Amorphous metal coatings are more corrosion resistant than conventional metals due to their unique microstructure with disordered and non-crystalline nature [163,164]. Recently, Raiman et al. [165] evaluated the corrosion of Ni-based alloy 230 with various amorphous metal coatings (Fe and Ni-based) in molten chloride KCl–$MgCl_2$ salt at 750 °C for 300 h in sealed Mo capsules. The coatings were deposited by using the spray method. In the case of uncoated samples, corrosion attack of 33 μm and chromium depletion near the surface was observed. No such attack was observed in coated sample due to crystallization occurred during exposure.

Application of corrosion resistive coatings is a potential solution to enable use low-cost structural materials. But the stability of such coatings at high temperatures is often a challenge. Mohammad et al. [166] studied the failure mechanism involved in nanostructured scandia 3.6 mol% and 0.4 mol% of yttria-stabilized zirconia topcoat by air plasma spraying on Inconel 738-LC with NiCrAlY bond coat tested in 45 wt% Na_2SO_4 + 55 wt% V_2O_5 molten salt at 910 °C. They reported that the formation of mixed oxides NiO, $NiAl_2O_4$ and $NiCr_2O_4$ are the main reason for failure of this thermal barrier coating. In the case of molten chloride and fluoride salt systems, the formation of an oxide barrier layer is a challenge [167].

Modification of alloy materials is another approach to improving corrosion resistance by creating an oxide layer that acts as a barrier which can prevent direct interaction of alloy with the corrosive environment [168,169]. The grown oxide should maintain the anticorrosive property, be thermodynamically stable towards the aggressive environments as well as adhere to the bulk material. Li et al. [170] studied the corrosion characteristics of aluminium/silicon alloyed Fe–Cr materials in gaseous or solid KCl salt at 650 °C in air. They reported that addition of silicon effectively reduced and enhanced the corrosion resistance of Fe–Cr alloys by forming a stable and dense oxide layer which controls the rapid growth of iron oxides. Gomez-Vidal et al. [77] investigated the corrosion properties of pre-oxidized AFAs of Haynes 224, Inconel 702 and Kanthal APMT at various temperatures in molten 35.59 wt% $MgCl_2$/64.41 wt% KCl at 700 °C in Ar atmosphere. Their results demonstrated that the formed Al_2O_3 scale, upon annealing, protected the base alloy from corrosion attack. Among all the alloys, pre-oxidized In702 in air (80%N_2 + 20%O_2) at 1050 °C for 4 h showed the best corrosion resistance due to presence of steady and stable alumina layers.

4.4. Surface texturing

Apart from the above methods, surface modification through texturing is an efficient method to mitigate corrosion [171,172]. In a recent work, we presented a novel approach of fractal surface texturing for reducing corrosion in solar salt maintained at 600 °C [173]. Fractal structures, with multi fractals of dimension above 1.90, on different alloy materials SS316, In625, In718, In800H, and Ha230 were fabricated by chemical etching. The fractal textured surfaces effectively reduced the corrosion rate by 30% in Fe-based alloys and 80–87% in high Ni-based alloys. Fig. 29 depicts cross-sectional SEM images of the corrosion layers on the plain, chemically etched, and etched-annealed surfaces after molten salt exposure for 300 h. From the figure, the thickness of the corrosion layer is seen to be less in etched and etched-annealed surfaces *vis-à-vis* plain, untextured, surface for all the alloys.

Corrosion rate of the alloys was determined using weight gain measurements and is shown in Fig. 30. In the plots, the red markers and dashed lines represent the corrosion rate of the plain samples, the green markers and dashed lines correspond to the etched substrates, and the orange markers and dashed lines denote the etched-annealed surfaces. It is observed that corrosion rate of all the alloys reduces with increase of immersion duration up to 400 h. Further, the etched substrates exhibit a low corrosion rate relative to the plain surfaces, for nearly all time instants except in In718. For In718 (Fig. 30(c)), initially higher corrosion is observed for the etched sample; however, at longer duration it reduces

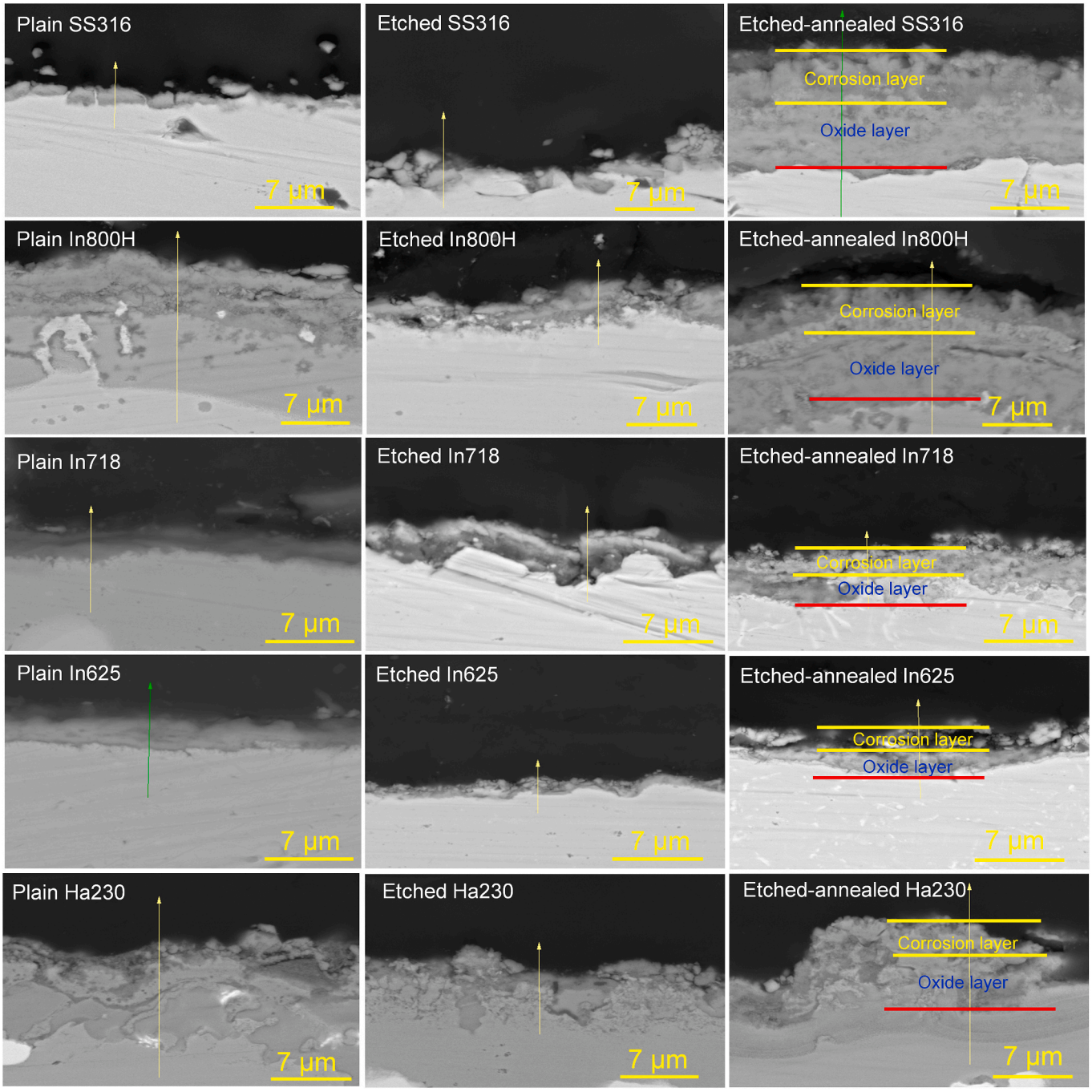

Fig. 29. X-SEM images of the corrosion layers formed on the plain, etched and etched-annealed surfaces of the various alloys after 300 h exposure in solar salt at 600 °C (reproduced with permission from Ref. [173]).

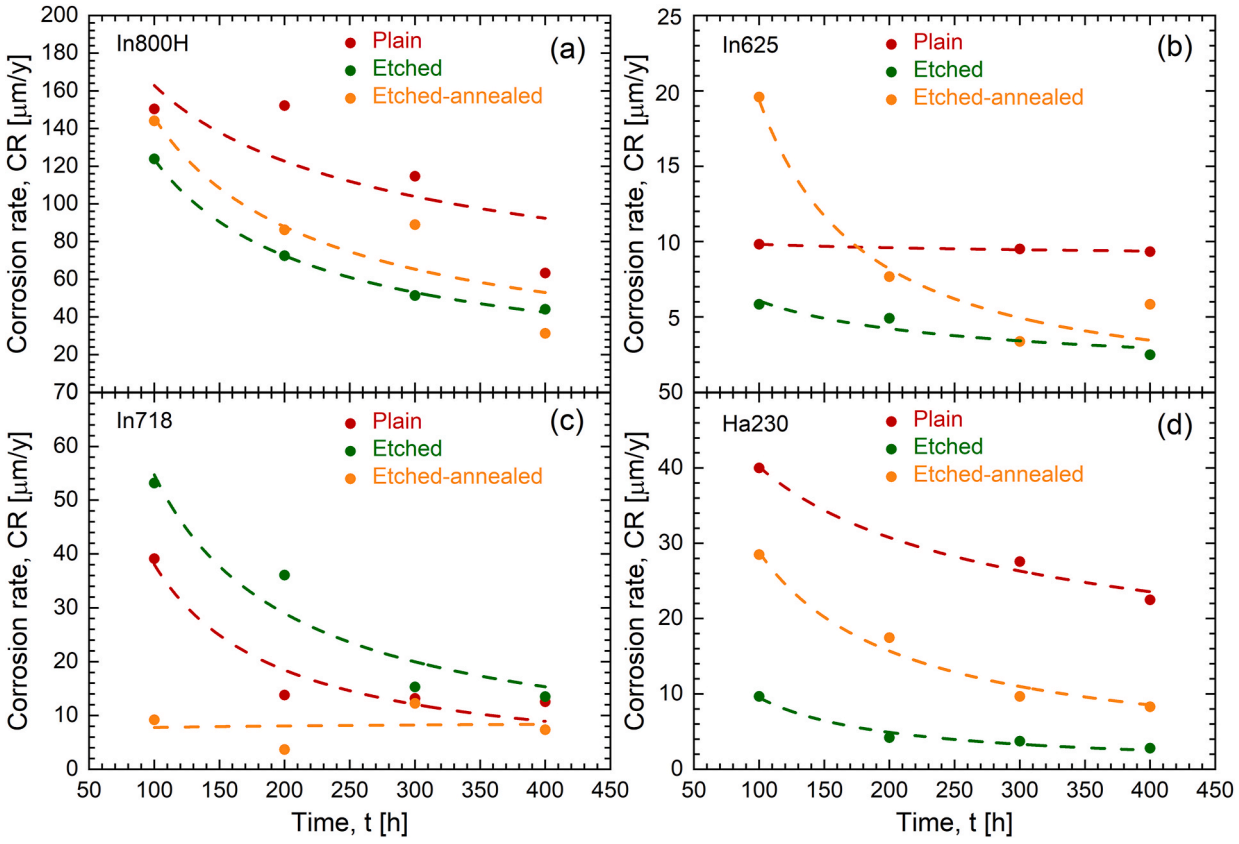

Fig. 30. Corrosion rate of (a) In800H, (b) In625, (c) Ha230, and (d) In718 alloys after immersion in solar salt at 600°C for 400 h (reproduced with permission from Ref. [173]).

significantly. Overall, the data trends in Fig. 30 indicate that the textured surfaces show a distinct advantage over the plain surfaces in the long run immersion. The above study shows that textured surfaces are an effective option to mitigating corrosion and offers much potential for application to other high temperature heat transfer fluids such as carbonates and chlorides [173].

In another study, we developed fractal structured Ni and NiYSZ coatings for corrosion mitigation in molten solar salt [174]. Highly adhesive, multiscale Ni and NiYSZ coatings were fabricated via electrodeposition and optimized using the Taguchi method. Corrosion of Fe- and Ni-based alloys with the optimized fractal coatings were examined in solar salt at 600 °C [174]. Fig. 31 shows the corrosion rate of the uncoated plain, plain-Ni, plain-NiYSZ, etched-Ni, and etched-NiYSZ surfaces of the five different substrates studied. In all the cases, the Ni and NiYSZ coatings on plain as well as etched surfaces exhibit a dramatically lower corrosion rate than the corresponding plain uncoated samples, suggesting that fractal textured coatings on plain and etched surfaces are viable options for reducing corrosion. In the case of

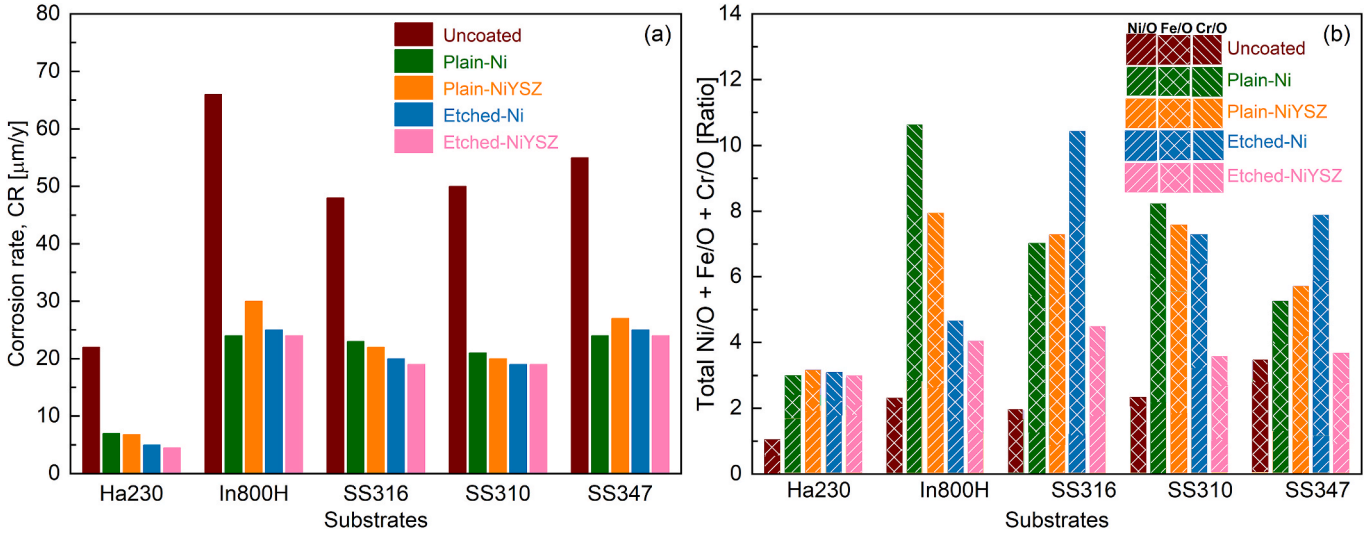

Fig. 31. (a) Corrosion rates of the Ni and NiYSZ coated samples with uncoated plain substrates after 400h in solar salt at 600 °C, and (b) comparison of the total metal-to-oxide ratio in the corrosion layers (reproduced with permission from Ref. [174]).

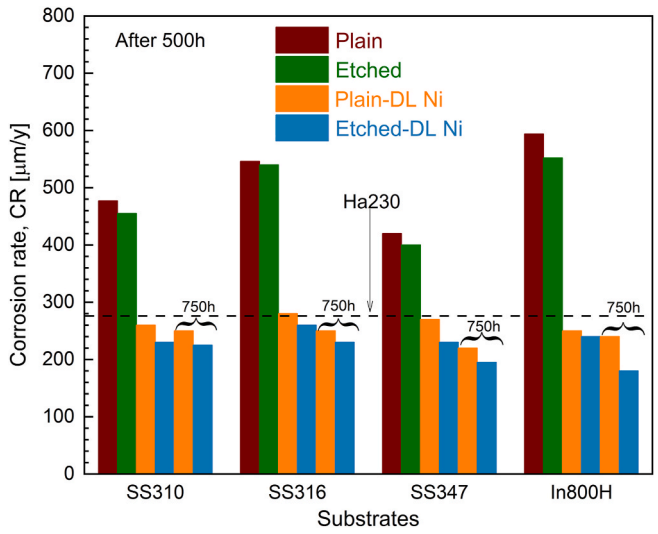

Fig. 32. Comparison of corrosion rate for the uncoated and DL Ni coated plain, etched Fe-based alloys of SS310, SS316, SS347 and In800H after 500 h and 750 h immersion. Corrosion rate of uncoated Ha230 is shown for reference as the black dotted line (reproduced with permission from Ref. [208]).

Fe-based alloys, fractal coatings via electrodeposition reduces the corrosion rate by ~58%, from ~50 μm/y to ~21 μm/y, for SS310, and by ~52%, from ~48 μm/y to ~23 μm/y, for SS316, by ~57%, from ~55 μm/y to ~24 μm/y, for SS347, and by ~64%, from about 66 μm/y to about 24 μm/y, for In800H. In the Ni-based Ha230 alloy, the coatings provide for ~68% reduction, from ~22 μm/y to ~7 μm/y.

For effective corrosion protection, it may be reasoned that the deposited metal coatings prevent the oxygen diffusion once the stable metal oxides formed during initial corrosion. Fig. 31(b) presents the total metal/oxygen ratio for the coated and uncoated samples of the five substrates. For all the alloys, it is clear that the ratio is generally greater for coated substrates compared to the uncoated substrates. This trend is in close agreement with the relative corrosion rate values in Fig. 31(a). Overall, the corrosion rate of coated Fe-based alloys reduced by up to 68% compared to uncoated alloys and was on par with or lower than the corrosion rate of Ha230.

Fractal-textured, highly stable double layer Ni (DL-Ni) coatings were also developed for effectively mitigating corrosion in carbonate salts at a high temperature of 750 °C, over a long duration of 750 h [208]. The corrosion rate for the uncoated and DL-Ni coated plain, etched Fe-based alloys of SS310, SS316, SS347 and In800H after 500 h and 750 h immersion is shown in Fig. 32 as the orange and blue bars, as marked.

The corrosion rate is seen to be durably low for the DL Ni coatings even after 750 h, demonstrating the long-term stability of the double-layer coatings. Overall, for the iron-based alloys, DL-Ni coatings via electrodeposition reduce the corrosion rate by ~52%, from 477 μm/y to 230 μm/y, for SS310, by ~53%, from ~546 μm/y to ~260 μm/y, for SS316, by ~46%, from 420 μm/y to 230 μm/y, for SS347, and by ~60%, from ~594 μm/y to nearly 240 μm/y for In800H. Further, the black dotted line in Fig. 32 indicates the corrosion rate of uncoated Ha230 (~280 μm/y) after 750 h, which is presented for comparison to the corrosion rates achieved by the coatings on the low-cost ferrous alloys. The DL-Ni coatings on plain and etched alloys showed a reduced corrosion rate of 230 μm/y that is about 18% lower than the corrosion rate of 280 μm/y for the expensive high Ni content Ha230. The corrosion rate of different alloy materials in different molten salts before and after various mitigation methods is presented in Table 11.

5. Summary and future studies

The U.S. Department of Energy's technical and economic goal for Gen3 CSP systems and similar mandates by other nations have triggered many research activities and developments to enhance CSP plant efficiency in various ways. The fundamental theme in all these efforts is harnessing solar thermal energy effectively and reducing the cost of the CSP system. As the efficiency of a CSP system directly depends on the operating temperature, thermally stable HTFs and low-cost structural materials with low corrosion attack are urgently needed.

According to the Gen3 roadmap, for molten salt based plants, an operating temperature of the CSP plant should be above 700 °C, the corrosion rate $< 15\ \mu$ m/y, and economic cost $<$ \$30/kWh$_t$. There are various heat transfer fluids for high temperature applications, of which the most encouraging are molten salts for their relatively low melting points and high thermal stability. Molten nitrate salts have been commercially used in current CSP systems. In addition, thermally stable chloride, carbonate, fluoride molten salts, and their eutectics, and liquid metals are attractive candidates for forthcoming CSP systems. The specific temperature range, thermophysical properties, and price of each molten salt along with liquid metals were reviewed. Apart from the properties, one of the most critical issues of the HTFs is their high corrosive nature to metal alloys. In this regard, the corrosion of various structural materials in each molten salt, liquid metals and supercritical

Table 11
Corrosion rate of structural materials in different molten salts at various temperatures before and after applying a mitigation method.

Structural material	Method of fabrication	Molten salt	Temperature [°C]	Duration [h]	CR[μm/y]	Reference
Bare T22 (CS)		15% $NaNO_3$-43% KNO_3-42% $Ca(NO3)_2$	390	500	100	[158]
T22 (CS)	Graphitization				66	
T22 (CS)	Graphitization	15% $NaNO_3$-43% KNO_3-42% $Ca(NO3)_2$ + 2% Graphite	390	500	18	
A516 Gr.70 (CS)		15% $NaNO_3$-43% KNO_3-42% $Ca(NO3)_2$	500	500	31.53	[156]
Coated CS	Graphitization				8.76	
SS310		$MgCl_2$+NaCl + KCl	700	500	1752	[150]
In 800H					876	
Ha C-276					526	
SS310	Addition of Mg to the molten salt	$MgCl_2$+NaCl + KCl	700	500	300	
In 800H					262	
Ha C-276					30	
Bare In800H		NaCl + KCl	700	24	2500	[161]
In 800H	(NiCoCrAlYHfSi) HOVF	NaCl + KCl	700	24	880	
Bare SS310		NaCl + KCl			4520	
SS310	(NiCrAl) HOVF	NaCl + KCl	700	24	1030	
In 800H	(NiCoCrAlYHfSi) HOVF	NaCl + KCl	700	24	690	
SS310	(NiCoCrAlYTa) HOVF	NaCl + KCl	700	24	190	
Alloy 230	Amorphous metal (Ni + Cr + Fe + Mo) HOVF	KCl + $MgCl_2$	750	300	0.02	[165]

carbon-di-oxide (sCO_2) was comprehensively reviewed, and the corrosion mechanisms were also discussed. Control of corrosion is essential in molten salt based CSP plants. With this in view, various corrosion mitigation methods and their advantages and disadvantages were reviewed. Targeted areas for further investigation and development were also identified.

Building on the wealth of developments so far in the field, looking forward, improving the efficiency of CSP plants requires high-temperature compatible materials that are resistant to corrosion by heat transfer fluids such as nitrates, carbonates, chlorides, liquid metals, and supercritical carbon-di-oxide. From the heat transfer fluid side, developments must lead to promising thermophysical properties for HTF and energy storage (e.g., low melting temperature, high heat capacity, high thermal conductivity), chemical compatibility with sCO_2, and high thermal stability ($> 750\ ^{\circ}C$). In a related need, more systematic characterization of the thermophysical properties as function of temperature, pressure, composition and other governing parameters through analytical relationships is warranted for the different HTFs.

In the literature, enhancement in the thermophysical properties such as specific heat, thermal conductivity, viscosity, and density of the molten salts at higher temperatures was achieved through adding various nanoparticles and/or using different compositions. However, the results are contradictory with regard to corrosion in molten salts with added nanoparticles. So, further research is needed to improve the salt properties while understanding the fundamental corrosion mechanisms of heat transfer fluids with the nanoadditives. In addition to experimental characterizations, which are abundant, accurate theoretical models should be developed in predicting thermophysical properties such as phase diagrams, viscosity, density, and specific heat of the mixed molten salts. Liquid metals have excellent heat transfer characteristics compared to molten salts but lower heat capacity, high density, and high cost. Development of liquid metals that address the technoeconomic and safety limitations is an area for further research. Besides, corrosion of containment materials in liquid metals is not understood well yet and is an area for further research.

Literature has shown that corrosion of Ni-based alloys is less than that of other Fe- and Cr-based metal alloys. However, the U.S. Department of Energy's cost targets cannot be reached if the entire system is designed from nickel super-alloys. Therefore, low-cost materials or approaches that meet high-temperature mechanical properties and low corrosion must be identified. Oxide and amorphous coatings have a significant influence in reducing the corrosion attack as discussed in this review. Still, there is a need to improve the mechanical durability and compatibility with the base materials at high temperatures. Besides, there is a need to develop coatings by low-cost and industrially viable methods for large area substrates.

The novel approach of using fractal textured surfaces presented in the review offers much potential for corrosion reduction, scalability to large structures and geometries, and enabling the use of low-cost Fe-based alloys in place of expensive high Ni-content alloys in high temperature applications prone to corrosion. Further work on the development of textured surfaces for corrosion mitigation in carbonates, chlorides, liquid metals and sCO_2 environment is a promising area for further research. Non-wetting surfaces developed on structural materials provide significant benefit in mitigating corrosion, but the studies are only limited to low temperatures. Creating high-temperature stable non-wetting surfaces with a high contact angle with molten salts to decrease the interaction with the salts, thereby increasing the materials' lifetime, is another challenging and highly rewarding prospect for further development.

Impurities present in the salts lead to severe corrosion. Proper purification protocols are needed that are scalable to large quantity molten salts. Salt purification methods and standardization of the protocols are required to eliminate cationic metallic impurities and corrosive moisture, oxides, and hydroxides in the hygroscopic halide molten salts. It is also necessary to identify salt impurities and quantify the degree of purity achieved. Advanced electrochemical characterizations and deep analysis are required for corrosion mitigation techniques, which allow low-cost and active metals such as Na, Zr, or Mg, to change redox potentials in halide molten salts.

It is envisioned that the holistic review presented in this article will serve as the foundation for further research addressing the relevant challenges and enabling the promise of achieving cost competitive CSP.

CRediT authorship contribution statement

P. Kondaiah: Investigation, Data curation, Methodology, Formal analysis, Writing – original draft. **R. Pitchumani:** Conceptualization, Investigation, Methodology, Formal analysis, Writing – review & editing, Resources, Supervision, Funding acquisition, Project administration.

Declaration of competing interest

The authors declare that they have no known competing financial interests or personal relationships that could have appeared to influence the work reported in this paper.

Data availability

All relevant data are included in the article.

Acknowledgments

The review was prepared as part of work supported by the U.S. Department of Energy's Office of Energy Efficiency and Renewable Energy (EERE) under the Solar Energy Technologies Office Award Number DE-EE0008525. This report was prepared as an account of work sponsored by an agency of the United States Government. Neither the United States Government nor any agency thereof, nor any of their employees, makes any warranty, express or implied, or assumes any legal liability or responsibility for the accuracy, completeness, or usefulness of any information, apparatus, product, or process disclosed, or represents that its use would not infringe privately owned rights. Reference herein to any specific commercial product, process, or service by trade name, trademark, manufacturer, or otherwise does not necessarily constitute or imply its endorsement, recommendation, or favoring by the United States Government or any agency thereof. The views and opinions of authors expressed herein do not necessarily state or reflect those of the United States Government or any agency thereof.

References

[1] BP, Statistical Review of World Energy globally consistent data on world energy markets . and authoritative publications in the field of energy, BP Energy Outlook 70 (2021) 8–20.
[2] K. Hansen, B. Vad Mathiesen, Comprehensive assessment of the role and potential for solar thermal in future energy systems, Sol. Energy 169 (2018) 144–152, https://doi.org/10.1016/j.solener.2018.04.039.
[3] O. Behar, Solar thermal power plants - a review of configurations and performance comparison, Renew. Sustain. Energy Rev. 92 (2018) 608–627, https://doi.org/10.1016/j.rser.2018.04.102.
[4] T. Franz, S. Christoph, S. Marlene, P. Thomas, K.C. Hoyer, Global potential of concentrating solar power, in: Proceedings of the SolarPACES, 2009. Berlin, Germany; 2009.
[5] Helioscsp, Concentrated solar power (CSP) vs. Photovoltaic (PV). https://doi.org/10.4324/9781315853178, 2019.
[6] S. Izquierdo, C. Montañs, C. Dopazo, N. Fueyo, Analysis of CSP plants for the definition of energy policies: the influence on electricity cost of solar multiples, capacity factors and energy storage, Energy Pol. 38 (2010) 6215–6221, https://doi.org/10.1016/j.enpol.2010.06.009.
[7] M. Mehos, C. Turchi, J. Vidal, M. Wagner, Z. Ma, C. Ho, W. Kolb, C. Andraka, Z. Ma, A. Kruizenga, NREL, concentrating solar power Gen3 demonstration roadmap. https://doi.org/10.2172/1338899, 2017.
[8] O. Achkari, A. El Fadar, Latest developments on TES and CSP technologies – energy and environmental issues , applications and research trends, Appl. Therm. Eng. 167 (2020), 114806, https://doi.org/10.1016/j.applthermaleng.2019.114806.

[9] IRENA, Renewable energy technologies: cost analysis series, Volume 1: Power Sector, https://doi.org/10.1542/peds.2006-2099, 2012.
[10] IRENA International Renewable Energy Agency, Renewable power generation costs in 2017. https://doi.org/10.1007/SpringerReference_7300, 2018.
[11] C.S. Turchi, M. Boyd, D. Kesseli, P. Kurup, M. Mehos, T. Neises, P. Sharan, M.J. Wagner, T. Wendelin, CSP Systems Analysis - Final Project Report, NREL/TP-5500-7285, 2019. https://www.nrel.gov/docs/fy19osti/72856.pdf (Accessed: January 2023).
[12] M. Liu, N.H. Steven Tay, S. Bell, M. Belusko, R. Jacob, G. Will, W. Saman, F. Bruno, Review on concentrating solar power plants and new developments in high temperature thermal energy storage technologies, Renew. Sustain. Energy Rev. 53 (2016) 1411–1432, https://doi.org/10.1016/j.rser.2015.09.026.
[13] H.-B Yin, J. Ding, X.-X. Yang, Heat accumulation technologies and systems for use in concentration type solar energy thermal power generation, Reneng Dongli Gongcheng/Journal of Engineering for Thermal Energy and Power 28 (1) (2013) 1–6.
[14] Y.X. Zuo Yz, J. Ding, Current status of thermal energy storage technologies used for concentrating solar power systems, 25, 2006, pp. 1–21.
[15] S. Ushak, A.G. Fernández, M. Grageda, Using Molten Salts and Other Liquid Sensible Storage Media in Thermal Energy Storage (TES) Systems, Woodhead Publishing Limited, 2015, https://doi.org/10.1533/9781782420965.1.49.
[16] K. Federsel, J. Wortmann, M. Ladenberger, High-temperature and corrosion behavior of nitrate nitrite molten salt mixtures regarding their application in concentrating solar power plants, Energy Proc. 69 (2015) 618–625, https://doi.org/10.1016/j.egypro.2015.03.071.
[17] U. Herrmann, D.W. Kearney, Survey of thermal energy storage for parabolic trough power plants, J. Sol. Energy Eng. Trans. ASME. 124 (2002) 145–152, https://doi.org/10.1115/1.1467601.
[18] Experience with molten salt thermal storage in a commercial parabolic trough plant, Andasol-1 commissioning and operation, in: Proceedings of the 15th International SolarPACES Symposium, International Energy Agency, Berlin, 2009, pp. 14–18.
[19] M. Chaanaoui, S. Vaudreuil, T. Bounahmidi, Benchmark of concentrating solar power plants: historical, current and future technical and economic development, Procedia Comput. Sci. 83 (2016) 782–789, https://doi.org/10.1016/j.procs.2016.04.167.
[20] T. Delise, A.C. Tizzoni, M. Ferrara, N. Corsaro, C. D'Ottavi, S. Sau, S. Licoccia, Thermophysical, environmental, and compatibility properties of nitrate and nitrite containing molten salts for medium temperature CSP applications: a critical review, J. Eur. Ceram. Soc. 39 (2019) 92–99, https://doi.org/10.1016/j.jeurceramsoc.2018.07.057.
[21] A. Bonk, S. Sau, N. Uranga, M. Hernaiz, T. Bauer, Advanced heat transfer fluids for direct molten salt line-focusing CSP plants, Prog. Energy Combust. Sci. 67 (2018) 69–87, https://doi.org/10.1016/j.pecs.2018.02.002.
[22] K. Vignarooban, X. Xu, A. Arvay, K. Hsu, A.M. Kannan, Heat transfer fluids for concentrating solar power systems - a review, Appl. Energy 146 (2015) 383–396, https://doi.org/10.1016/j.apenergy.2015.01.125.
[23] M. Henríquez, L. Guerreiro, Á.G. Fernández, E. Fuentealba, Lithium nitrate purity influence assessment in ternary molten salts as thermal energy storage material for CSP plants, Renew. Energy 149 (2020) 940–950, https://doi.org/10.1016/j.renene.2019.10.075.
[24] M. Durth, C. Prieto, A. Rodríguez-Sánchez, D. Patiño-Rodríguez, L.F. Cabeza, Effects of sodium nitrate concentration on thermophysical properties of solar salts and on the thermal energy storage cost, Sol. Energy 182 (2019) 57–63, https://doi.org/10.1016/j.solener.2019.02.038.
[25] C. Villada, F. Jaramillo, J.G. Castaño, F. Echeverría, F. Bolívar, Design and development of nitrate-nitrite based molten salts for concentrating solar power applications, Sol. Energy 188 (2019) 291–299, https://doi.org/10.1016/j.solener.2019.06.010.
[26] A.G. Fernández, S. Ushak, H. Galleguillos, F.J. Pérez, Thermal characterisation of an innovative quaternary molten nitrate mixture for energy storage in CSP plants, Sol. Energy Mater. Sol. Cells 132 (2015) 172–177, https://doi.org/10.1016/j.solmat.2014.08.020.
[27] A.G. Fernández, S. Ushak, H. Galleguillos, F.J. Pérez, Development of new molten salts with $LiNO_3$ and $Ca(NO_3)_2$ for energy storage in CSP plants, Appl. Energy 119 (2014) 131–140, https://doi.org/10.1016/j.apenergy.2013.12.061.
[28] L. lu Zou, X. Chen, Y. ting Wu, X. Wang, C. fang Ma, Experimental study of thermophysical properties and thermal stability of quaternary nitrate molten salts for thermal energy storage, Sol. Energy Mater. Sol. Cells 190 (2019) 12–19, https://doi.org/10.1016/j.solmat.2018.10.013.
[29] U. Nithiyanantham, Y. Grosu, A. Anagnostopoulos, E. Carbó-Argibay, O. Bondarchuk, L. González-Fernández, A. Zaki, J.M. Igartua, M.E. Navarro, Y. Ding, A. Faik, Nanoparticles as a high-temperature anticorrosion additive to molten nitrate salts for concentrated solar power, Sol. Energy Mater. Sol. Cells 203 (2019), 110171, https://doi.org/10.1016/j.solmat.2019.110171.
[30] J. Navas, A. Sánchez-Coronilla, E.I. Martín, M. Teruel, J.J. Gallardo, T. Aguilar, R. Gómez-Villarejo, R. Alcántara, C. Fernández-Lorenzo, J.C. Piñero, J. Martín-Calleja, On the enhancement of heat transfer fluid for concentrating solar power using Cu and Ni nanofluids: an experimental and molecular dynamics study, Nano Energy 27 (2016) 213–224, https://doi.org/10.1016/j.nanoen.2016.07.004.
[31] X. Wei, Y. Yin, B. Qin, W. Wang, J. Ding, J. Lu, Preparation and enhanced thermal conductivity of molten salt nanofluids with nearly unaltered viscosity, Renew. Energy 145 (2020) 2435–2444, https://doi.org/10.1016/j.renene.2019.04.153.
[32] G. Mohan, M. Venkataraman, J. Gomez-Vidal, J. Coventry, Thermo-economic analysis of high-temperature sensible thermal storage with different ternary eutectic alkali and alkaline earth metal chlorides, Sol. Energy 176 (2018) 350–357, https://doi.org/10.1016/j.solener.2018.10.008.
[33] D. Han, B. Guene Lougou, Y. Xu, Y. Shuai, X. Huang, Thermal properties characterization of chloride salts/nanoparticles composite phase change material for high-temperature thermal energy storage, Appl. Energy 264 (2020), 114674, https://doi.org/10.1016/j.apenergy.2020.114674.
[34] W. Ding, A. Bonk, T. Bauer, Molten chloride salts for next generation CSP plants: selection of promising chloride salts & study on corrosion of alloys in molten chloride salts, in: AIP Conf. Proc., American Institute of Physics Inc., 2019, https://doi.org/10.1063/1.5117729.
[35] K. Wang, E. Molina, G. Dehghani, B. Xu, P. Li, Q. Hao, P. Lucas, M. Kassaee, S. Jeter, A. Teja, Experimental investigation to the properties of eutectic salts by NaCl-KCl-$ZnCl_2$ for application as high temperature heat transfer fluids, Paper No: ES2014-6578, V001T02A040, in: Proceedings ASME 2014 8th International Conference on Energy Sustainability, 2014, 6 pages, https://doi.org/10.1115/ES2014-6578.
[36] X. Xu, X. Wang, P. Li, Y. Li, Q. Hao, B. Xiao, H. Elsentriecy, D. Gervasio, Experimental test of properties of KCl-$MgCl_2$ eutectic molten salt for heat transfer and thermal storage fluid in concentrated solar power systems, J. Sol. Energy Eng. Trans. ASME. 140 (2018), https://doi.org/10.1115/1.4040065.
[37] Y. Li, X. Xu, X. Wang, P. Li, Q. Hao, B. Xiao, Survey and evaluation of equations for thermophysical properties of binary/ternary eutectic salts from NaCl, KCl, $MgCl_2$, $CaCl_2$, $ZnCl_2$ for heat transfer and thermal storage fluids in CSP, Sol. Energy 152 (2017) 57–79, https://doi.org/10.1016/j.solener.2017.03.019.
[38] W. Xie, J. Ding, G. Pan, Q. Fu, X. Wei, J. Lu, W. Wang, Heat and mass transportation properties of binary chloride salt as a high-temperature heat storage and transfer media, Sol. Energy Mater. Sol. Cells 209 (2020), 110415, https://doi.org/10.1016/j.solmat.2020.110415.
[39] G.J. Janz, G.L. Gardner, U. Krebs, R.P.T. Tomkins, Molten salts: volume 4, Part 1, fluorides and mixtures electrical conductance, density, viscosity, and surface tension data, J. Phys. Chem. Ref. Data 3 (1974) 1–115, https://doi.org/10.1063/1.3253134.
[40] R.P. Clark, Heats of fusion and heat capacities of lithium chloride-potassium chloride eutectic and potassium nitrate, J. Chem. Eng. Data 18 (1973) 67–70, https://doi.org/10.1021/je60056a023.
[41] N. Lorenzin, A. Abánades, A review on the application of liquid metals as heat transfer fluid in Concentrated Solar Power technologies, Int. J. Hydrogen Energy 41 (2016) 6990–6995, https://doi.org/10.1016/j.ijhydene.2016.01.030.
[42] J. Coventry, C. Andraka, J. Pye, M. Blanco, J. Fisher, A review of sodium receiver technologies for central receiver solar power plants, Sol. Energy 122 (2015) 749–762, https://doi.org/10.1016/j.solener.2015.09.023.
[43] R. Moore, M. Vernon, C. K. Ho, N.P. Siegel, G.J. Kolb, Design Considerations for Concentrating Solar Power Tower Systems Employing Molten Salt. Technical Report SAND2010-697, 2010, https://www.osti.gov/servlets/purl/1008140 (Accessed: January 2023).
[44] S.H. Goods, R.W. Bradshaw, M.R. Prairie. Corrosion of Stainless and Carbon Steels in Molten Mixtures of Industrial Nitrates, 1994, https://doi.org/10.2172/10141843.
[45] G. García-Martín, M.I. Lasanta, V. Encinas-Sánchez, M.T. de Miguel, F.J. Pérez, Evaluation of corrosion resistance of A516 Steel in a molten nitrate salt mixture using a pilot plant facility for application in CSP plants, Sol. Energy Mater. Sol. Cells 161 (2017) 226–231, https://doi.org/10.1016/j.solmat.2016.12.002.
[46] A. Kruizenga, D. Gill, Corrosion of iron stainless steels in molten nitrate salt, Energy Proc. 49 (2014) 878–887, https://doi.org/10.1016/j.egypro.2014.03.095.
[47] S.H. Goods, R.W. Bradshaw, Corrosion of stainless steels and carbon steel by molten mixtures of commercial nitrate salts, 78–87, https://doi.org/10.1361/10599490417542, 2004.
[48] A.G. Fernández, H. Galleguillos, E. Fuentealba, F.J. Pérez, Corrosion of stainless steels and low-Cr steel in molten $Ca(NO_3)_2$-$NaNO_3$-KNO_3 eutectic salt for direct energy storage in CSP plants, Sol. Energy Mater. Sol. Cells 141 (2015) 7–13, https://doi.org/10.1016/j.solmat.2015.05.004.
[49] Standard Practice for Preparing, Cleaning, and Evaluating Corrosion Test Specimens, ASTM Spec. Tech. Publ, 1985, pp. 505–510, https://doi.org/10.1520/G0001-03.2.
[50] G. McConohy, A. Kruizenga, Molten nitrate salts at 600 and 680°C: thermophysical property changes and corrosion of high-temperature nickel alloys, Sol. Energy 103 (2014) 242–252, https://doi.org/10.1016/j.solener.2014.01.028.
[51] R.G. Kelly, J.R. Scully, D. Shoesmith, R.G. Buchheit, Electrochemical techniques in corrosion science and engineering. https://doi.org/10.1201/9780203909133, 2002.
[52] M. Stern, Electrochemical polarization, 1. A theoretical analysis of the shape of polarization curves, J. Electrochem. Soc. 104 (1957) 751, https://doi.org/10.1149/1.2428473.
[53] V. Encinas-Sánchez, M.T. de Miguel, M.I. Lasanta, G. García-Martín, F.J. Pérez, Electrochemical impedance spectroscopy (EIS): an efficient technique for monitoring corrosion processes in molten salt environments in CSP applications, Sol. Energy Mater. Sol. Cells 191 (2019) 157–163, https://doi.org/10.1016/j.solmat.2018.11.007.
[54] J.C. Gomez-Vidal, A.G. Fernandez, R. Tirawat, C. Turchi, W. Huddleston, Corrosion resistance of alumina forming alloys against molten chlorides for energy production. II: electrochemical impedance spectroscopy under thermal cycling conditions, Sol. Energy Mater. Sol. Cells 166 (2017) 234–245, https://doi.org/10.1016/j.solmat.2017.03.025.

[55] K. Sridharan, T.R. Allen, Corrosion in molten salts, in: Molten Salts Chem, Elsevier Inc., 2013, pp. 241–267, https://doi.org/10.1016/B978-0-12-398538-5.00012-3.
[56] M. Walczak, F. Pineda, Á.G. Fernández, C. Mata-torres, R.A. Escobar, Materials corrosion for thermal energy storage systems in concentrated solar power plants, Renew. Sustain. Energy Rev. 86 (2018) 22–44, https://doi.org/10.1016/j.rser.2018.01.010.
[57] D.F. Williams, L.M. Toth, Chemical Considerations for the Selection of the Coolant for the Advanced High-Temperature Reactor, ORNL/GEN4/LTR-05-011, doi:10.2172/4299382.
[58] S. Bell, T. Steinberg, G. Will, Corrosion mechanisms in molten salt thermal energy storage for concentrating solar power, Renew. Sustain. Energy Rev. 114 (2019), https://doi.org/10.1016/j.rser.2019.109328.
[59] T. Tzvetkoff, A. Girginov, M. Biginov, Review Corrosion of Nickel , Iron , Cobalt and Their Alloys in Molten Salt Electrolytes, J. Mat. Sci. 30 (1995),5561–5575, doi.org/10.1007/BF00356688.
[60] M. Orfield, D.A. Shores, Solubility of NiO in Molten Li_2CO_3, Na_2CO_3, K_2CO_3 Aand Rb_2CO_3 at 910 oC, J. Electrochem. Soc. 135 (1988) 1662–1668, https://doi.org/10.1149/1.2096093.
[61] M.L. Orfield, D.A. Shores, The Solubility of NiO in Binary Mixtures of Molten Carbonates the Solubility of NiO in Binary Mixtures of Molten Carbonates, J. Electrochem. Soc. 136 (1989) 2862, https://doi.org/10.1149/1.2096301.
[62] P. Dolado, A. Gil, M. Medrano, I. Martorell, A. La, L.F. Cabeza, State of the art on high temperature thermal energy storage for power generation, Part 1 — Concepts , materials and modellization 14 (2010) 31–55, https://doi.org/10.1016/j.rser.2009.07.035.
[63] R.W. Bradshaw, S.H. Goods, Corrosion of alloys and metals by molten nitrates, Sandia Report SAND2000-8727 (2001) 1–34. https://www.osti.gov/servlets/purl/1545803 (Accessed: January 2023).
[64] A. Soleimani Dorcheh, R.N. Durham, M.C. Galetz, Corrosion behavior of stainless and low-chromium steels and IN625 in molten nitrate salts at 600 °C, Sol. Energy Mater. Sol. Cells 144 (2016) 109–116, https://doi.org/10.1016/j.solmat.2015.08.011.
[65] A. Gomes, M. Navas, N. Uranga, T. Paiva, I. Figueira, T.C. Diamantino, High-temperature corrosion performance of austenitic stainless steels type AISI 316L and AISI 321H, in molten Solar Salt, Sol. Energy 177 (2019) 408–419, https://doi.org/10.1016/j.solener.2018.11.019.
[66] J. Wang, Y. Jiang, Y. Ni, A. Wu, J. Li, Investigation on static and dynamic corrosion behaviors of thermal energy transfer and storage system materials by molten salts in concentrating solar power plants, Mater. Corros. 70 (2019) 102–109, https://doi.org/10.1002/maco.201810362.
[67] W. Wang, B. Guan, X. Li, J. Lu, J. Ding, Solar Energy Materials and Solar Cells Corrosion behavior and mechanism of austenitic stainless steels in a new quaternary molten salt for concentrating solar power, Sol. Energy Mater. Sol. Cells 194 (2019) 36–46, https://doi.org/10.1016/j.solmat.2019.01.024.
[68] A. Bonk, C. Martin, M. Braun, T. Bauer, Material investigations on the thermal stability of solar salt and potential filler materials for molten salt storage, AIP Conf. Proc. 1850 (2017), https://doi.org/10.1063/1.4984429.
[69] C. Yang, X. Wei, W. Wang, Z. Lin, J. Ding, Y. Wang, Q. Peng, J. Yang, NOx emissions and the component changes of ternary molten nitrate salts in thermal energy storage process, Appl. Energy 184 (2016) 346–352, https://doi.org/10.1016/j.apenergy.2016.10.024.
[70] A. Bonk, D. Rückle, S. Kaesche, M. Braun, T. Bauer, Impact of Solar Salt aging on corrosion of martensitic and austenitic steel for concentrating solar power plants, Sol. Energy Mater. Sol. Cells 203 (2019), 110162, https://doi.org/10.1016/j.solmat.2019.110162.
[71] V.A. Sötz, A. Bonk, J. Steinbrecher, T. Bauer, Defined purge gas composition stabilizes molten nitrate salt - experimental prove and thermodynamic calculations, Sol. Energy 211 (2020) 453–462, https://doi.org/10.1016/j.solener.2020.09.041.
[72] K. Vignarooban, X. Xu, K. Wang, E.E. Molina, P. Li, D. Gervasio, A.M. Kannan, Vapor pressure and corrosivity of ternary metal-chloride molten-salt based heat transfer fluids for use in concentrating solar power systems, Appl. Energy 159 (2015) 206–213, https://doi.org/10.1016/j.apenergy.2015.08.131.
[73] B. Liu, X. Wei, W. Wang, J. Lu, J. Ding, Corrosion behavior of Ni-based alloys in molten NaCl-$CaCl_2$-$MgCl_2$ eutectic salt for concentrating solar power, Sol. Energy Mater. Sol. Cells 170 (2017) 77–86, https://doi.org/10.1016/j.solmat.2017.05.050.
[74] K. Vignarooban, P. Pugazhendhi, C. Tucker, D. Gervasio, A.M. Kannan, Corrosion resistance of Hastelloys in molten metal-chloride heat-transfer fluids for concentrating solar power applications, Sol. Energy 103 (2014) 62–69, https://doi.org/10.1016/j.solener.2014.02.002.
[75] W. Ding, H. Shi, Y. Xiu, A. Bonk, A. Weisenburger, A. Jianu, T. Bauer, Hot corrosion behavior of commercial alloys in thermal energy storage material of molten $MgCl_2$/KCl/NaCl under inert atmosphere, Sol. Energy Mater. Sol. Cells 184 (2018) 22–30, https://doi.org/10.1016/j.solmat.2018.04.025.
[76] A.G. Fernández, L.F. Cabeza, Corrosion monitoring and mitigation techniques on advanced thermal energy storage materials for CSP plants, Sol. Energy Mater. Sol. Cells 192 (2019) 179–187, https://doi.org/10.1016/j.solmat.2018.12.028.
[77] J.C. Gomez-Vidal, A.G. Fernandez, R. Tirawat, C. Turchi, W. Huddleston, Corrosion resistance of alumina-forming alloys against molten chlorides for energy production . I : pre-oxidation treatment and isothermal corrosion tests, Sol. Energy Mater. Sol. Cells 166 (2017) 222–233, https://doi.org/10.1016/j.solmat.2017.02.019.
[78] A.G. Fernández, L.F. Cabeza, Corrosion evaluation of eutectic chloride molten salt for new generation of CSP plants. Part 2: materials screening performance, J. Energy Storage 29 (2020), 101381, https://doi.org/10.1016/j.est.2020.101381.
[79] L. Guo, Y. Yue, T.J. Pan, Z.F. Tang, W. Liu, Corrosion behavior of Ni-Al alloys beneath chlorides melt salt at 700 °C, Sol. Energy 184 (2019) 657–663, https://doi.org/10.1016/j.solener.2019.04.045.
[80] A.R. Shankar, A. Kanagasundar, U.K. Mudali, Corrosion of nickel-containing alloys in molten LiCl-KCl medium, Corrosion 69 (2013) 48–57, https://doi.org/10.5006/0627.
[81] A. Ravi Shankar, K. Thyagarajan, U. Kamachi Mudali, Corrosion behavior of candidate materials in molten LiCl-KCl salt under argon atmosphere, Corrosion 69 (2013) 655–665, https://doi.org/10.5006/0746.
[82] M. Groll, O. Brost, D. Heine, Corrosion of steels in contact with salt eutectics as latent heat storage materials: influence of water and other impurities, Heat Recovery Syst. CHP 10 (1990) 567–572, https://doi.org/10.1016/0890-4332(90)90207-Z.
[83] C. Prieto, S. Fereres, F.J. Ruiz-caba, A. Rodriguez-sanchez, C. Montero, Carbonate molten salt solar thermal pilot facility : plant design, commissioning and operation up to 700 °C, 151, 2020, pp. 528–541, https://doi.org/10.1016/j.renene.2019.11.045.
[84] V.M.B. Nunes, M.J.V. Lourenço, F.J.V. Santos, C.A. Nieto de Castro, Molten alkali carbonates as alternative engineering fluids for high temperature applications, Appl. Energy 242 (2019) 1626–1633, https://doi.org/10.1016/j.apenergy.2019.03.190.
[85] X. Li, S. Wu, Y. Wang, L. Xie, Experimental investigation and thermodynamic modeling of an innovative molten salt for thermal energy storage (TES), Appl. Energy 212 (2018) 516–526, https://doi.org/10.1016/j.apenergy.2017.12.069.
[86] S. Frangini, A. Masi, ScienceDirect Molten carbonates for advanced and sustainable energy applications : Part I . Revisiting molten carbonate properties from a sustainable viewpoint, Int. J. Hydrogen Energy 41 (2016) 18739–18746, https://doi.org/10.1016/j.ijhydene.2015.12.073.
[87] Y. Wu, N. Ren, T. Wang, C. Ma, Experimental study on optimized composition of mixed carbonate salt for sensible heat storage in solar thermal power plant, Sol. Energy 85 (2011) 1957–1966, https://doi.org/10.1016/j.solener.2011.05.004.
[88] R.I. Olivares, S. Wright, The thermal stability of molten lithium – sodium – potassium carbonate and the influence of additives on the melting point, 2012 1–8,, https://doi.org/10.1115/1.4006895.
[89] A.G. Fernández, F. Pineda, M. Walczak, L.F. Cabeza, Corrosion evaluation of alumina-forming alloys in carbonate molten salt for CSP plants, Renew. Energy 140 (2019) 227–233, https://doi.org/10.1016/j.renene.2019.03.087.
[90] P. Biedenkopf, H.J. Grabke, The Corrosion Behavior of Fe-Cr Alloys Containing Co, Mn, And/or Ni and of a Co-base Alloy in the Presence of Molten (Li,K)-carbonate, Materials and Corrosion 48 (11) (1997) 731–743. https://doi.org/10.1002/maco.19970481103.
[91] M.T. De Miguel, V. Encinas-sánchez, M.I. Lasanta, F.J. Pérez, Solar Energy Materials & Solar Cells Corrosion resistance of HR3C to a carbonate molten salt for energy storage applications in CSP plants, Sol. Energy Mater. Sol. Cells 157 (2016) 966–972, https://doi.org/10.1016/j.solmat.2016.08.014.
[92] S.P. Sah, E. Tada, A. Nishikata, Corrosion behaviour of austenitic stainless steels in carbonate melt at 923 K under controlled CO_2-O_2 environment, Corrosion Sci. 133 (2018) 310–317, https://doi.org/10.1016/j.corsci.2018.01.031.
[93] A.J. Appleby, S.B. Nicholson, Reduction of oxygen in lithium-potassium carbonate melt, J. Electroanal. Chem. 112 (1980) 71–76, https://doi.org/10.1016/S0022-0728(80)80008-8.
[94] A.J. Appleby Nicholson S.B., Reduction of oxygen in alkali carbonate melts, J. Electroanal. Chem. 83(2) (1977) 309–328 https://doi.org/10.1016/S0022-0728(77)80176-9.
[95] M. Sarvghad, T.A. Steinberg, Solar Energy Materials and Solar Cells Corrosion of steel alloys in eutectic NaCl + Na_2CO_3 at 700 ° C and Li_2CO_3 + K_2CO_3 + Na_2CO_3 at 450 ° C for thermal energy storage, 48–59, https://doi.org/10.1016/j.solmat.2017.05.063, 2017.
[96] A.A. Attia, S.A. Salih, A.M. Baraka,Corrosion and passivation behaviors of some stainless steel alloys inmolten alkali carbonates, Electrochimica Acta 48(2) (2002) 113–118. https://doi.org/10.1016/S0013-4686(02)00506-6.
[97] T.H. Lim, E.R. Hwang, H.Y. Ha, S.W. Nam, I.H. Oh, S.A. Hong, Effects of temperature and partial pressure of CO_2/O_2 on corrosion behaviour of stainless-steel in molten Li/Na carbonate salt, J. Power Sources 89 (2000) 1–6, https://doi.org/10.1016/S0378-7753(00)00376-1.
[98] S. Frangini, Corrosion behavior of AISI 316L stainless steel and ODS FeAl aluminide in eutectic Li_2CO_3-K_2CO_3 molten carbonates under flowing CO_2-O_2 gas mixtures, Oxid. Metals 53 (2000) 139–156, https://doi.org/10.1023/a:1004538931676.
[99] P. Biedenkopf, M. Spiegel, H.J. Grabke, The corrosion behaviour of iron and chromium in molten $(Li0.62K0.38)_2CO_3$, Electrochim. Acta 44 (1998) 683–692, https://doi.org/10.1016/S0013-4686(97)10191-8.
[100] D.F. Williams, K.T. Clarno, Evaluation of salt coolants for reactor applications evaluation of salt coolants, Nuclear Technol. 163:3 (2008) 330-343,. https://doi.org/10.13182/NT08-A3992.
[101] H.G. MacPherson, Development of materials and systems for molten salt-reactor concept. https://www.osti.gov/biblio/4678401. (Accessed January 2023).
[102] T. Allen, K. Sridharan, M. Anderson, M. Corradini, Molten salt heat transport loop: materials corrosion and heat transfer phenomena, NERI Tech. Rep. (2008) 1–88. doi:10.2172/934785.
[103] J.R. Keiser, J.H. DeVan, E.J. Lawrence,Compatibility of molten salts with type 316 stainless steel and lithium, J. Nuclear Mater. 85-86 (1979) 295–298. https://doi.org/10.1016/0022-3115(79)90505-1.

[104] O. Muránsky, C. Yang, H. Zhu, I. Karatchevtseva, P. Sláma, Z. Nový, L. Edwards, Molten salt corrosion of Ni-Mo-Cr candidate structural materials for Molten Salt Reactor (MSR) systems, Corros. Sci 159 (2019), 108087, https://doi.org/10.1016/j.corsci.2019.07.011.
[105] M.W. Rosenthal, P.R. Kasten, R.B. Briggs, Molten-salt reactors—history, status, and potential, 2017, pp. 107–117. https://doi.org/10.13182/NT70-A28619.
[106] W.R. Grimes, Molten-salt Reactor Chemistry, Nucl. Appl. Technol. 8 (1970) 137–155. https://doi.org/10.13182/NT70-A28621.
[107] Y. Wang, C. Zeng, W. Li, The influence of temperature gradient on the corrosion of materials in molten fluorides, Corrosion Science 136 (2018) 180–187. https://doi.org/10.1016/j.corsci.2018.03.003.
[108] J. Pacio, T. Wetzel, Assessment of liquid metal technology status and research paths for their use as efficient heat transfer fluids in solar central receiver systems, Sol. Energy 93 (2013) 11–22, https://doi.org/10.1016/j.solener.2013.03.025.
[109] J. Pacio, A. Fritsch, C. Singer, R. Uhlig, Liquid metals as efficient coolants for high-intensity point-focus receivers : implications to the design and performance of next- generation CSP systems, Energy Proc. 49 (2014) 647–655, https://doi.org/10.1016/j.egypro.2014.03.070.
[110] Y. Zhang, Y. Cai, S. Hwang, G. Wilk, F. Deangelis, A. Henry, K.H. Sandhage, Containment materials for liquid tin at 1350 °C as a heat transfer fluid for high temperature concentrated solar power, Sol. Energy 164 (2018) 47–57, https://doi.org/10.1016/j.solener.2018.01.085.
[111] J. Pacio, T. Wetzel, Assessment of liquid metal technology status and research paths for their use as efficient heat transfer fluids in solar central receiver systems, Sol. Energy 93 (2013) 11–22, https://doi.org/10.1016/j.solener.2013.03.025.
[112] M.P. Popović, A.M. Bolind, C. Cionea, P. Hosemann, Liquid lead-bismuth eutectic as a coolant in generation iv nuclear reactors and in high temperature solar concentrator applications: characteristics, challenges, issues, Contemp. Mater. 6 (2015), https://doi.org/10.7251/comen1501020p.
[113] M. Mecheri, Y. Le, Supercritical CO_2 Brayton cycles for coal- fired power plants, Energy 103 (2016) 758–771, https://doi.org/10.1016/j.energy.2016.02.111.
[114] M.T. White, G. Bianchi, L. Chai, S.A. Tassou, A.I. Sayma, Review of supercritical CO_2 technologies and systems for power generation, Appl. Therm. Eng. 185 (2021), https://doi.org/10.1016/j.applthermaleng.2020.116447.
[115] G. Angelino, Real gas effects in carbon dioxide, (1969) 1–12, doi:10.1115/69-GT-102.
[116] V. Dostal, M.J. Driscoll, P. Hejzlar, A Supercritical Carbon Dioxide Cycle for Next Generation Nuclear Reactors, Technical Report MIT-ANP-TR-100, 2004. https://web.mit.edu/22.33/www/dostal.pdf (Accessed: January 2023).
[117] S. Polimeni, M. Binotti, L. Moretti, G. Manzolini, Comparison of Sodium and KCl-MgCl2 as Heat Transfer Fluids in CSP Solar Tower with sCO2 Power Cycles, 162, 2018, pp. 510–524, https://doi.org/10.1016/j.solener.2018.01.046.
[118] G. Cao, V. Firouzdor, K. Sridharan, M. Anderson, T.R. Allen, Corrosion of austenitic alloys in high temperature supercritical carbon dioxide, Corrosion Sci. 60 (2012) 246–255, https://doi.org/10.1016/j.corsci.2012.03.029.
[119] V. Firouzdor, K. Sridharan, G. Cao, M. Anderson, T.R. Allen, Corrosion of a stainless steel and nickel-based alloys in high temperature supercritical carbon dioxide environment, Corrosion Sci. 69 (2013) 281–291, https://doi.org/10.1016/j.corsci.2012.11.041.
[120] L.F. He, P. Roman, B. Leng, K. Sridharan, M. Anderson, T.R. Allen, Corrosion behavior of an alumina forming austenitic steel exposed to supercritical carbon dioxide, Corrosion Sci. 82 (2014) 67–76, https://doi.org/10.1016/j.corsci.2013.12.023.
[121] U. Nithiyanantham, Y. Grosu, L. González-fernández, A. Zaki, Corrosion aspects of molten nitrate salt-based nanofluids for thermal energy storage applications, Sol. Energy 189 (2019) 219–227, https://doi.org/10.1016/j.solener.2019.07.050.
[122] Y. Grosu, N. Udayashankar, O. Bondarchuk, L. González-fernández, A. Faik, Unexpected effect of nanoparticles doping on the corrosivity of molten nitrate salt for thermal energy storage, Sol. Energy Mater. Sol. Cells 178 (2018) 91–97, https://doi.org/10.1016/j.solmat.2018.01.002.
[123] M. Schuller, F. Little, D. Malik, M. Betts, S. Qian, J. Luo, W. Zhong, S. Shankar, Molten Salt-Carbon Nanotube Thermal Energy Storage for Concentrating Solar Power Systems, Final Report (2012), https://doi.org/10.2172/1036948.
[124] U. Nithiyanantham, A. Zaki, Y. Grosu, L. González-Fernández, J.M. Igartua, A. Faik, $SiO_2@Al_2O_3$ core-shell nanoparticles based molten salts nanofluids for thermal energy storage applications, J. Energy Storage 26 (2019), 101033, https://doi.org/10.1016/j.est.2019.101033.
[125] H. Li, X. Yang, X. Yin, X. Wang, J. Tang, J. Gong, Effect of chloride impurity on corrosion kinetics of stainless steels in molten solar salt for CSP application: experiments and modeling, Oxid. Metals 95 (2021) 311–332, https://doi.org/10.1007/s11085-021-10025-y.
[126] R.W. Bradshaw, S.H. Goods, Corrosion Resistance of Stainless Steels during Thermal Cycling in Alkali Nitrate Molten salts, 2001, https://doi.org/10.2172/1020472.
[127] Y. Grosu, O. Bondarchuk, A. Faik, The e ff ect of humidity , impurities and initial state on the corrosion of carbon and stainless steels in molten HitecXL salt for CSP application, Sol. Energy Mater. Sol. Cells 174 (2018) 34–41, https://doi.org/10.1016/j.solmat.2017.08.026.
[128] A. Zahs, M. Spiegel, H. Ju, È. Grabke, Chloridation and Oxidation of Iron , Chromium , Nickel and Their Alloys in Chloridizing and Oxidizing Atmospheres at 400- 700 ₀C, Corrosion Sci. 42 (2000) 1093–112, doi:10.1016/S0010-938X(99)00142-0.
[129] W. Ding, A. Bonk, T. Bauer, Corrosion behavior of metallic alloys in molten chloride salts for thermal energy storage in concentrated solar power plants, A review, Front. Chem. Sci. Eng. 12 (2018) 564–576. https://doi.org/10.1007/s11705-018-1720-0.
[130] J. De Bakker, J. Peacey, B. Davis, Thermal decomposition studies on magnesium hydroxychlorides, Can. Metall. Q. 51 (2012) 419–423, https://doi.org/10.1179/1879139512Y.0000000007.
[131] S. Kashani-Nejad, K.W. Ng, R. Harris, Preparation of MgOHCl by controlled dehydration of $MgCl_2{\cdot}6H_2O$, Metall. Mater. Trans. B 35 (2004) 405–406, https://doi.org/10.1007/s11663-004-0042-4.
[132] B.L. Garcia-diaz, L. Olson, M. Martinez-rodriguez, R. Fuentes, H. Colon, J. Gray, High Temperature Electrochemical Engineering and Clean Energy Systems, Journal of the South Carolina Academy of Science, 14 (2016), pp. 11–14. https://scholarcommons.sc.edu/jscas/vol14/iss1/4 (Accessed: January 2023).
[133] B.A.T. Mehrabadi, J.W. Weidner, B. Garcia-Diaz, M. Martinez-Rodriguez, L. Olson, S. Shimpalee, Modeling the effect of cathodic protection on superalloys inside high temperature molten salt systems, J. Electrochem. Soc. 164 (2017) C171–C179, https://doi.org/10.1149/2.1461704jes.
[134] Z. Zhang, X. Lu, T. Wang, Y. Yan, F. Pan, The dehydration of $MgCl_2{\cdot}6H_2O$ in $MgCl_2{\cdot}6H_2O$-KCl-NH4Cl system, J. Anal. Appl. Pyrolysis 110 (2014) 248–253, https://doi.org/10.1016/j.jaap.2014.09.009.
[135] G.S. Chen, Removal of oxide impurities from alkali haloaluminate melts using carbon tetrachloride, J. Electrochem. Soc. 140 (1993) 1523, https://doi.org/10.1149/1.2221596.
[136] N. Kanari, I. Gaballah, Chlorination and carbochlorination of magnesium oxide, Metall. Mater. Trans. B 30 (1999) 383–391, https://doi.org/10.1007/s11663-999-0070-1.
[137] J.M. Kurley, P.W. Halstenberg, A. McAlister, S. Raiman, S. Dai, R.T. Mayes, Enabling chloride salts for thermal energy storage: implications of salt purity, RSC Adv. 9 (2019) 25602–25608, https://doi.org/10.1039/c9ra03133b.
[138] G. Pedro Smith, C.R. Boston, Influence of rare-gas-configuration cations on the absorption spectra of nickel (II) centers in liquid chloride and bromide salts, J. Chem. Phys. 43 (1965) 4051–4056, https://doi.org/10.1063/1.1696639.
[139] Z. Zhang, X. Lu, S. Yang, F. Pan, Preparation of anhydrous magnesium chloride from magnesia, Ind. Eng. Chem. Res. 51 (2012) 9713–9718, https://doi.org/10.1021/ie300765u.
[140] N. Klammer, C. Engtrakul, Y. Zhao, Y. Wu, J. Vidal, Method to determine MgO and MgOHCl in chloride molten salts, Anal. Chem. 92 (2020) 3598–3604, https://doi.org/10.1021/acs.analchem.9b04301.
[141] Q. Gong, W. Ding, Y. Chai, A. Bonk, J. Steinbrecher, T. Bauer, Chemical analysis and electrochemical monitoring of extremely low-concentration corrosive impurity MgOHCl in molten $MgCl_2$–KCl–NaCl, Front. Energy Res. 10 (2022) 1–13, https://doi.org/10.3389/fenrg.2022.811832.
[142] A.G. Fernández, L.F. Cabeza, Corrosion evaluation of eutectic chloride molten salt for new generation of CSP plants . Part 1 : thermal treatment assessment, J. Energy Storage 27 (2020), 101125, https://doi.org/10.1016/j.est.2019.101125.
[143] B.A. Pint. Progression to Compatibility Evaluations in Flowing Molten Salts, 2020, https://doi.org/10.2172/1649281.
[144] S. Guo, J. Zhang, W. Wu, W. Zhou, Corrosion in the molten fluoride and chloride salts and materials development for nuclear applications, Prog. Mater. Sci. 97 (2018) 448–487, https://doi.org/10.1016/j.pmatsci.2018.05.003.
[145] J. Zhang, C.W. Forsberg, M.F. Simpson, S. Guo, S.T. Lam, R.O. Scarlat, F. Carotti, K.J. Chan, P.M. Singh, W. Doniger, K. Sridharan, J.R. Keiser, Redox potential control in molten salt systems for corrosion mitigation, Corrosion Sci. 144 (2018) 44–53, https://doi.org/10.1016/j.corsci.2018.08.035.
[146] C.G. Dariva, A.F. Galio, Corrosion Inhibitors – Principles, Mechanisms and Applications, (2014) 365-380, doi:10.5772/57255.
[147] J.E. Indacochea, J.L. Smith, K.R. Litko, E.J. Karell, Corrosion Performance of Ferrous and Refractory Metals in Molten Salts under Reducing Conditions, J. Mater. Research 14 (5) 1990–1995, doi:10.1557/JMR.1999.0268.
[148] J.E. Indacochea, J.L. Smith, K.R. Litko, E.J. Karell, High-Temperature Oxidation and Corrosion of Structural Materials in Molten Chlorides, Materials Science (2001) 55, https://doi.org/10.1023/A:1010333407304.
[149] W. Ding, H. Shi, A. Jianu, Y. Xiu, A. Bonk, A. Weisenburger, T. Bauer, Molten chloride salts for next generation concentrated solar power plants : mitigation strategies against corrosion of structural materials, Sol. Energy Mater. Sol. Cells 193 (2019) 298–313, https://doi.org/10.1016/j.solmat.2018.12.020.
[150] W. Ding, J. Gomez-Vidal, A. Bonk, T. Bauer, Molten chloride salts for next generation CSP plants : electrolytical salt purification for reducing corrosive impurity level, Sol. Energy Mater. Sol. Cells 199 (2019) 8–15, https://doi.org/10.1016/j.solmat.2019.04.021.
[151] K. Hanson, K.M. Sankar, P.F. Weck, J.K. Startt, R. Dingreville, C.S. Deo, J. D. Sugar, P.M. Singh, Effect of excess Mg to control corrosion in molten $MgCl_2$ and KCl eutectic salt mixture, Corrosion Sci. 194 (2022), 109914, https://doi.org/10.1016/j.corsci.2021.109914.
[152] D.K. Guptha, S.M. Meier, The Evolution of Thermal Barrier Coatings in Gas Turbine Engine Applications, J. Eng. Gas Turbines Power. (1994) 116. https://doi.org/10.1115/1.2906801.
[153] N.P. Padture, M. Gell, E.H. Jordan, Thermal Barrier Coatings for Gas-Turbine Engine Applications. *Science*, vol. 296, no. 5566, 2002, pp. 280–84. *JSTOR*, http://www.jstor.org/stable/3076507. (Accessed: January 2023).
[154] J.T. Demasi-Marcin, D.K. Gupta, Protective coatings in the gas turbine engine, Surface. Coat. Technol. 69 (1994) 1–9, https://doi.org/10.1016/0257-8972(94)90129-5.
[155] V. Encinas-Sánchez, E. Batuecas, A. Macías-García, C. Mayo, R. Díaz, F.J. Pérez, Corrosion resistance of protective coatings against molten nitrate salts for thermal energy storage and their environmental impact in CSP technology, Sol. Energy 176 (2018) 688–697, https://doi.org/10.1016/j.solener.2018.10.083.

[156] J. Piquot, U. Nithiyanantham, Y. Grosu, A. Faik, Solar Energy Materials and Solar Cells Spray-graphitization as a protection method against corrosion by molten nitrate salts and molten salts based nano fl uids for thermal energy storage applications, Sol. Energy Mater. Sol. Cells 200 (2019), 110024, https://doi.org/10.1016/j.solmat.2019.110024.
[157] Y. Grosu, U. Nithiyanantham, A. Zaki, A. Faik, A simple method for the inhibition of the corrosion of carbon steel by molten nitrate salt for thermal storage in concentrating solar power applications, Npj Mater. Degrad. 2 (2018) 1–8, https://doi.org/10.1038/s41529-018-0055-0.
[158] M. Gonzalez, U. Nithiyanantham, E. Carbó-argibay, O. Bondarchuk, Y. Grosu, A. Faik, Graphitization as e ffi cient inhibitor of the carbon steel corrosion by molten binary nitrate salt for thermal energy storage at concentrated solar power, Sol. Energy Mater. Sol. Cells 203 (2019), 110172, https://doi.org/10.1016/j.solmat.2019.110172.
[159] K.G. Parker Dw, HVOF — spray technology — poised for growth, Adv. Mater. Process. 139 (1991) 68–74.
[160] T.S. Sidhu, R.D. Agrawal, S. Prakash, Hot corrosion of some superalloys and role of high-velocity oxy-fuel spray coatings - a review, Surf. Coat. Technol. 198 (2005) 441–446, https://doi.org/10.1016/j.surfcoat.2004.10.056.
[161] J.C. Gomez-Vidal, Corrosion resistance of MCrAlX coatings in a molten chloride for thermal storage in concentrating solar power applications, Npj Mater. Degrad. 1 (2017) 1–9, https://doi.org/10.1038/s41529-017-0012-3.
[162] J.C. Gomez-Vidal, J. Noel, J. Weber, Corrosion evaluation of alloys and MCrAlX coatings in molten carbonates for thermal solar applications, Sol. Energy Mater. Sol. Cells 157 (2016) 517–525, https://doi.org/10.1016/j.solmat.2016.07.029.
[163] H.R. Ma, J.W. Li, C.T. Chang, X.M. Wang, R.W. Li, Passivation behavior of Fe-based amorphous coatings prepared by high-velocity air/oxygen fuel processes, 2040–2047, https://doi.org/10.1007/s11666-017-0647-1, 2017.
[164] A. Grayeli-korpi, H. Savaloni, M. Habibi, Corrosion inhibition of stainless steel type AISI 304 by Mn coating and subsequent annealing with flow of nitrogen at different temperatures, Appl. Surf. Sci. 276 (2013) 269–275, https://doi.org/10.1016/j.apsusc.2013.03.081.
[165] S.S. Raiman, R.T. Mayes, J.M. Kurley, R. Parrish, E. Vogli, Amorphous and partially-amorphous metal coatings for corrosion resistance in molten chloride salt, Sol. Energy Mater. Sol. Cells 201 (2019), 110028, https://doi.org/10.1016/j.solmat.2019.110028.
[166] M.R. Loghman-estarki, M. Nejati, H. Edris, R. Shoja, Evaluation of hot corrosion behavior of plasma sprayed scandia and yttria co-stabilized nanostructured thermal barrier coatings in the presence of molten sulfate and vanadate salt, J. Eur. Ceram. Soc. 35 (2015) 693–702, https://doi.org/10.1016/j.jeurceramsoc.2014.08.029.
[167] M. Hofmeister, L. Klein, H. Miran, R. Rettig, S. Virtanen, R.F. Singer, Corrosion behaviour of stainless steels and a single crystal superalloy in a ternary LiCl – KCl – CsCl molten salt, Corrosion Sci. 90 (2015) 46–53, https://doi.org/10.1016/j.corsci.2014.09.009.
[168] M.P. Brady, B. Gleeson, I.G. Wright, Alloy Design Strategies for Promoting Protective Oxide-Scale Formation, The Journal of The Minerals, Metals & Materials Society 52 (2000) 16–21, https://doi.org/10.1007/s11837-000-0109-x.
[169] Y. Yamamoto, M.P. Brady, Z.P. Lu, P.J. Maziasz, C.T. Liu, B.A. Pint, K.L. More, H. M. Meyer, E.A. Payzant, Creep-Resistant, Al_2O_3-Forming Austenitic Stainless Steels, Science 80 (2007) 316, https://doi.org/10.1126/science.1137711.
[170] Y.S. Li, Y. Niu, M. Spiegel, High temperature interaction of Al/Si-modified Fe – Cr alloys with KCl, Corrosion Sci 49 (2007) 1799–1815, https://doi.org/10.1016/j.corsci.2006.10.019.
[171] M.F.B. Sousa, H.C. Loureiro, C.A. Bertran, Anti-scaling performance of slippery liquid-infused porous surface (SLIPS) produced onto electrochemically-textured 1020 carbon steel, Surf. Coat. Technol. 382 (2020), 125160, https://doi.org/10.1016/j.surfcoat.2019.125160.
[172] R. Jain, R. Pitchumani, Fractal model for wettability of rough surfaces, Langmuir 33 (2017) 7181–7190. https://doi.org/10.1021/acs.langmuir.7b01524.
[173] P. Kondaiah, R. Pitchumani, Fractal textured surfaces for high temperature corrosion mitigation in molten salts, Sol. Energy Mater. Sol. Cells 230 (2021), 111281, https://doi.org/10.1016/j.solmat.2021.111281.
[174] P. Kondaiah, R. Pitchumani, Fractal coatings of Ni and NiYSZ for high-temperature corrosion mitigation in solar salt, Corrosion Sci. 201 (2022), 110283, https://doi.org/10.1016/j.corsci.2022.110283.
[175] S. Wu, H. Peng, L. Xie, Design and investigation of the novel $ZnCl_2$ based ternary chloride salts with low-temperature for sensible energy storage, Appl. Therm. Eng. 171 (2020), https://doi.org/10.1016/j.applthermaleng.2020.114917.
[176] G. Mohan, M.B. Venkataraman, J. Coventry, Sensible energy storage options for concentrating solar power plants operating above 600 °C, Renew. Sustain. Energy Rev. 107 (2019) 319–337, https://doi.org/10.1016/j.rser.2019.01.062.
[177] X. Wei, Y. Yin, B. Qin, W. Wang, J. Ding, J. Lu, Preparation and enhanced thermal conductivity of molten salt nano fluids with nearly unaltered viscosity, Renew. Energy 145 (2020) 2435–2444, https://doi.org/10.1016/j.renene.2019.04.153.
[178] X. Xu, G. Dehghani, J. Ning, P. Li, Basic properties of eutectic chloride salts NaCl-KCl-$ZnCl_2$ and NaCl-KCl-$MgCl_2$ as HTFs and thermal storage media measured using simultaneous DSC-TGA, Sol. Energy 162 (2018) 431–441, https://doi.org/10.1016/j.solener.2018.01.067.
[179] T. Liu, X. Xu, W. Liu, X. Zhuang, Corrosion of alloys in high temperature molten-salt heat transfer fluids with air as the cover gas, Sol. Energy 191 (2019) 435–448, https://doi.org/10.1016/j.solener.2019.09.015.
[180] T. Wang, D. Mantha, R.G. Reddy, Novel high thermal stability LiF–Na_2CO_3–K_2CO_3 eutectic ternary system for thermal energy storage applications, Sol. Energy Mater. Sol. Cells 140 (2015) 366–375, https://doi.org/10.1016/j.solmat.2015.04.033.
[181] R. Serrano-López, J. Fradera, S. Cuesta-Lopez, Molten salts database for energy applications, Chem. Eng. Process. Process Intensif. 73 (2013) 87–102, https://doi.org/10.1016/j.cep.2013.07.008.
[182] W. Xie, J. Ding, X. Wei, W. Wang, G. Xia, J. Xing, Corrosion resistance of stainless steel and pure metal in ternary molten nitrate for thermal energy storage, Energy Proc. 158 (2019) 4897–4902, https://doi.org/10.1016/j.egypro.2019.01.703.
[183] K.L. Summers, D. Chidambaram, Corrosion behavior of structural materials for potential use in nitrate salts based solar thermal power plants, J. Electrochem. Soc. 164 (2017), https://doi.org/10.1149/2.0501708jes. H5357–H5363.
[184] A. Palacios, M.E. Navarro, Z. Jiang, A. Avila, G. Qiao, E. Mura, Y. Ding, High-temperature corrosion behaviour of metal alloys in commercial molten salts, Sol. Energy 201 (2020) 437–452, https://doi.org/10.1016/j.solener.2020.03.010.
[185] P. Audigié, V. Encinas-Sánchez, M. Juez-Lorenzo, S. Rodríguez, M. Gutiérrez, F. J. Pérez, A. Agüero, High temperature molten salt corrosion behavior of aluminide and nickel-aluminide coatings for heat storage in concentrated solar power plants, Surf. Coat. Technol. 349 (2018) 1148–1157, https://doi.org/10.1016/j.surfcoat.2018.05.081.
[186] N. Tranvan, S.P. Sah, E. Tada, A. Nishikata, Cathodic protection of type 310S stainless steel in a chloride – bromide mixed molten salt at 923 K, Corrosion Sci. 157 (2019) 62–69, https://doi.org/10.1016/j.corsci.2019.05.002.
[187] X. Zhuang, W. Liu, X. Xu, Hot corrosion of different alloys in chloride and carbonate molten-salt mixtures under argon atmosphere, Sol. Energy 189 (2019) 254–267, https://doi.org/10.1016/j.solener.2019.07.065.
[188] H. Sun, J. Wang, Z. Li, P. Zhang, X. Su, Corrosion behavior of 316SS and Ni-based alloys in a ternary NaCl-KCl-$MgCl_2$ molten salt, Sol. Energy 171 (2018) 320–329, https://doi.org/10.1016/j.solener.2018.06.094.
[189] L. Guo, Q. Liu, H. Yin, T.J. Pan, Z. Tang, Excellent corrosion resistance of 316 stainless steel in purified NaCl-$MgCl_2$ eutectic salt at high temperature, Corrosion Sci. 166 (2020), 108473, https://doi.org/10.1016/j.corsci.2020.108473.
[190] S.P. Sah, E. Tada, A. Nishikata, Corrosion behaviour of austenitic stainless steels in carbonate melt at 923 K under controlled CO_2 -O_2 environment, Corrosion Sci. 133 (2018) 310–317, https://doi.org/10.1016/j.corsci.2018.01.031.
[191] H. Ai, M. Shen, H. Sun, K.P. Dolan, C. Wang, M. Ge, H. Yin, X. Li, H. Peng, N. Li, L. Xie, Effects of O^{2-} additive on corrosion behavior of Fe–Cr–Ni alloy in molten fluoride salts, Corrosion Sci. 150 (2019) 175–182, https://doi.org/10.1016/j.corsci.2019.01.040.
[192] F.Y. Ouyang, C.H. Chang, J.J. Kai, Long-term corrosion behaviors of Hastelloy-N and Hastelloy-B3 in moisture-containing molten FLiNaK salt environments, J. Nucl. Mater. 446 (2014) 81–89, https://doi.org/10.1016/j.jnucmat.2013.11.045.
[193] H. Ai, X.X. Ye, L. Jiang, B. Leng, M. Shen, Z. Li, Y. Jia, J.Q. Wang, X. Zhou, Y. Xie, L. Xie, On the possibility of severe corrosion of a Ni-W-Cr alloy in fluoride molten salts at high temperature, Corrosion Sci. 149 (2019) 218–225, https://doi.org/10.1016/j.corsci.2019.01.012.
[194] L.C. Olson, J.W. Ambrosek, K. Sridharan, M.H. Anderson, T.R. Allen, Materials corrosion in molten LiF-NaF-KF salt, J. Fluor. Chem. 130 (2009) 67–73, https://doi.org/10.1016/j.jfluchem.2008.05.008.
[195] Q. Dai, X.X. Ye, H. Ai, S. Chen, L. Jiang, J. Liang, K. Yu, B. Leng, Z. Li, X. Zhou, Corrosion of Incoloy 800H alloys with nickel cladding in FLiNaK salts at 850 °C, Corrosion Sci. 133 (2018) 349–357, https://doi.org/10.1016/j.corsci.2018.01.026.
[196] M.C. Trent, S.H. Goods, R.W. Bradshaw, Comparison of corrosion performance of grade 316 and grade 347H stainless steels in molten nitrate salt, AIP Conf. Proc. 1734 (2016), https://doi.org/10.1063/1.4949258.
[197] J.C. Gomez-Vidal, R. Tirawat, Corrosion of alloys in a chloride molten salt (NaCl-LiCl) for solar thermal technologies, Sol. Energy Mater. Sol. Cells 157 (2016) 234–244, https://doi.org/10.1016/j.solmat.2016.05.052.
[198] M. Sarvghad, O. Muránsky, T.A. Steinberg, J. Hester, M.R. Hill, G. Will, On the effect of cold-rolling on the corrosion of SS316L alloy in a molten carbonate salt, Sol. Energy Mater. Sol. Cells 202 (2019), https://doi.org/10.1016/j.solmat.2019.110136.
[199] J. Gallardo-González, M. Martínez, C. Barreneche, A.I. Fernández, M. Liu, N.H. S. Tay, F. Bruno, M. Segarra, Corrosion of AISI316 as containment material for latent heat thermal energy storage systems based on carbonates, Sol. Energy Mater. Sol. Cells 186 (2018) 1–8, https://doi.org/10.1016/j.solmat.2018.06.003.
[200] P. Audigié, V. Encinas-Sánchez, S. Rodríguez, F.J. Pérez, A. Agüero, High temperature corrosion beneath carbonate melts of aluminide coatings for CSP application, Sol. Energy Mater. Sol. Cells 210 (2020), https://doi.org/10.1016/j.solmat.2020.110514.
[201] R. Repukaiti, L. Teeter, M. Ziomek-Moroz, Ö. Doğan, J. Tucker, Corrosion behavior of steels in supercritical CO_2 for power cycle applications, ECS Trans. 77 (2017) 799–808, https://doi.org/10.1149/07711.0799ecst.
[202] H.J. Lee, H. Kim, S.H. Kim, C. Jang, Corrosion and carburization behavior of chromia-forming heat resistant alloys in a high-temperature supercritical-carbon dioxide environment, Corrosion Sci. 99 (2015) 227–239, https://doi.org/10.1016/j.corsci.2015.07.007.
[203] M. Walker, E. Withey, Influence of CO_2 purity on the corrosion of structural alloys for supercritical CO_2 power cycles, in: 6th Int. Supercrit. CO_2 Power Cycles Symp, 2018, pp. 1–20. March 27 - 29, 2018, Pittsburgh, Pennsylvania, https://www.osti.gov/servlets/purl/1513649.
[204] J. Mahaffey, A. Kaira, M. Anderson, K. Sridharan, Materials corrosion in high temperature supercritical carbon dioxide, in: 4th Int. Symp. - Supercrit. CO_2 Power Cycles Sept. 9-10, 2014, Pennsylvania Mater, Pittsburgh, 2014. https://citeseerx.ist.psu.edu/document?repid=rep1&type=pdf&doi=5d5cba3c3ef72ea2e2c8374be1c2fc7a29ef99a3. (Accessed January 2023).

[205] Z. Liang, Y. Gui, Y. Wang, Q. Zhao, Corrosion performance of heat-resisting steels and alloys in supercritical carbon dioxide at 650 °C and 15 MPa, Energy 175 (2019) 345–352, https://doi.org/10.1016/j.energy.2019.03.014.

[206] J. Mahaffey, David Adam, M. Anderson, K. Sridharan, Effect of Oxygen Impurity on Corrosion in Supercritical CO_2 Environments, The 5th International Supercritical CO_2 Power Cycles Symposium, March 29–31, San Antonio, Texas, 2016. https://sco2symposium.com/papers2016/Materials/114paper.pdf. (Accessed January 2023).

[207] A. Brittan, J. Mahaffey, M. Anderson, K. Sridharan, Mechanical and corrosion performance of the weld of 740H and 282, in: 6th Int. Symp. - Supercrit. CO_2 Power Cycles, 2018, 11 pp, https://www.osti.gov/servlets/purl/1524974. (Accessed January 2023).

[208] P. Kondaiah, R. Pitchumani, Novel textured surfaces for superior corrosion mitigation in molten carbonate salts for concentrating solar power, Renew Sustain Energy Rev 170 (2022) 112961, https://doi.org/10.1016/j.rser.2022.112961.